NOTE TO USERS

This reproduction is the best copy available.

UMI®

VERTEX DIFFRACTED EDGE WAVES ON A PERFECTLY CONDUCTING PLANE ANGULAR SECTOR

ALPER KURSAT OZTURK

A THESIS

IN

THE DEPARTMENT

OF

ELECTRICAL AND COMPUTER ENGINEERING

PRESENTED IN PARTIAL FULFILLMENT OF THE REQUIREMENTS
FOR THE DEGREE OF DOCTOR OF PHILOSOPHY
CONCORDIA UNIVERSITY
MONTRÉAL, QUÉBEC, CANADA

SEPTEMBER 2009
© ALPER KURSAT OZTURK, 2009

Library and Archives
Canada

Published Heritage
Branch

395 Wellington Street
Ottawa ON K1A 0N4
Canada

Bibliothèque et
Archives Canada

Direction du
Patrimoine de l'édition

395, rue Wellington
Ottawa ON K1A 0N4
Canada

Canada

Abstract

Vertex Diffracted Edge Waves on a Perfectly Conducting Plane
Angular Sector

Alper Kursat Ozturk, Ph.D.

Concordia University, 2009

The problem of electromagnetic scattering from a perfectly-conducting plane angular sector has been of interest for many years. An exact solution for this problem has been developed based on the separation of variables in sphero-conal coordinate system. In this solution, fields and currents are expressed in terms of scalar wave functions that are the solutions of a two parameter eigenvalue problem of two coupled spherical Lamé differential equations and spherical Bessel functions. The resulting expressions are in the form of eigenfunction expansions. These expansions are slowly convergent and not suitable for high frequency scattering calculations. Despite their computational advantages, high-frequency modeling techniques fail to provide accurate results for many classes of problems. Lack of a vertex diffraction coefficient is a major factor that limits the accuracy of the high frequency diffraction techniques. Furthermore, the vertex-excited surface currents are strongly guided by the edges of the angular sector creating strong singularities on the current and charge densities.

The singular behavior of the current density near the sharp edges of a scattering target is also known as the edge condition and should be modeled properly in numerical solutions to improve the accuracy.

In this thesis, numerical diffraction coefficients are derived for vertex-diffracted edge waves induced on an infinitely-thin, perfectly conducting semi-infinite plane angular sector. The diffraction coefficients are formulated to be used in a purely high-frequency modeling of a scattering problem. The current density on the surface of the plane angular sector is modeled using the physical theory of diffraction (PTD). The vertex-diffracted currents are defined as the difference between the exact and PTD currents. The difference current is then modeled as a wave traveling away from the corner with unknown amplitude and phase factors. The unknown coefficients for the vertex-diffracted currents are calculated by using a least squares fit approximation. The vertex-diffracted currents are successfully modeled even for very narrow angular sectors for arbitrary directions of incidence. Illustrative examples are presented to demonstrate the substantial improvement provided by the vertex-diffracted currents to the accuracy of RCS patterns.

Another aspect of the research in this thesis is the development of higher-order basis functions for the Method of Moments (MoM) solution. A set of divergence-conforming basis functions was developed to model the singular behavior of the surface currents near the edges and corners of an infinitely-thin, perfectly-conducting polygonal flat plate. The basis functions are derived by imposing the edge and corner conditions on the first order basis functions. It is demonstrated that, even though

the new basis functions are not highest order complete, they provide accurate results without incurring complexity in the analysis or additional computational requirements.

Acknowledgments

I would like to express my sincere gratitude to my supervisors Dr. Robert Paknys and Dr. Christopher Trueman for their guidance and encouragement. This work would not have been completed without their support, confidence, and patience. I feel fortunate to have worked with them.

I would also like to thank Dr. Abdel R. Sebak, Dr. Ibahim G. Hassan, Dr. Luiz A. C. Lopes and Dr. Prabhakar Pathak for serving in my examining committee and for their valuable suggestions and comments.

I would like to thank my friends Armin Parsa, Sadegh Farzaneh, Malcolm Ng Mou Kehn, Donald Davis and Celal Alp Tunc for their friendship and moral support. A special thanks to my friend Volkan Efe for the many interesting conversations we have had over the years.

Thanks are finally due to my parents for their endless support and understanding.

Table of Contents

List of Figures

xv

List of Tables

List of Abbreviations

APE   Asymptotic Phasefront Extraction

FW   Fringe Wave

GO   Geometrical Optics

GTD   Geometrical Theory of Diffraction

ITD   Incremental Theory of Diffraction

LSF   Least squares fit

MEMP   Matrix Enhancement Matrix Pencil

MoM   Method of Moments

MPM   Matrix Pencil Method

PO   Physical Optics

PTD   Physical Theory of Diffraction

PWS   Plane Wave Spectral

RCS   Radar Cross Section

UTD   Uniform Theory of Diffraction

Chapter 1

Introduction

The problem of electromagnetic scattering from a perfectly-conducting plane angular sector has been of interest for many years. An exact solution based on the separation of variables in the sphero-conal coordinate system was first developed by Satterwhite [1]. The solution was later verified by Hansen [2]. In this solution, fields and currents are expressed in terms of scalar wave functions that are the solutions of a two parameter eigenvalue problem of two coupled spherical Lamé differential equations and spherical Bessel functions. The resulting expressions are in the form of eigenfunction expansions. These expansions are slowly convergent and not suitable for high frequency scattering calculations. Based on Satterwhite's solution, several attempts have been made to obtain a tractable approximation that can be used in the high frequency modeling of the angular sector problem [3], [4]. The eigenfunction expansions for the currents and fields are particularly difficult to evaluate when both the source and observation points are far from the corner. An efficient numerical evaluation procedure for calculating the radar cross section (RCS) of an elliptic cone was presented by Blume and Uschkerat [5]. This procedure is based on using Euler's sequence transformation to accelerate the convergence of the infinite series of eigenfunction expansions. Blume and Krebs [6] used a similar approach to derive dyadic

diffraction coefficients at the tip of an elliptic cone for nose-on incidence. The same problem was solved by Babich *et al.* [7] through numerical evaluation of the Fredholm integral equation that is obtained by combining the soft and hard boundary conditions on the surface of the cone [8]. Even though these developments provide certain advantages in terms of describing the behavior of the currents and fields near the tip of the cone, the resulting expressions are difficult to use in numerical calculations. As a result, it was not possible to derive a corner diffraction coefficient from the exact eigenfunction solution.

Lack of a corner diffraction coefficient is a major factor that limits the accuracy of the high frequency diffraction techniques. Consider an infinitely-thin, perfectly conducting plane angular sector. The current density on the surface of the angular sector can be approximated using the physical theory of diffraction (PTD) [9]. The current density is expressed as the sum of the physical optics (PO) and the fringe wave (FW) components. The FW component accounts for the edge-diffracted currents and acts as a correction to the PO component just like the geometrical theory of diffraction (GTD) currents being a correction to the geometrical optics (GO) currents. In the application of high-frequency techniques to 3-D scattering problems, the surface currents are often expressed in the form of equivalent edge currents. The far field is then given by the line integral of the equivalent currents along the edges. When the equivalent edge currents are integrated along a finite or semi-infinite edge, the asymptotic evaluation of the line integral results in end-point contributions. These end-point contributions are interpreted as corner diffracted fields. It should be noted that, these end-point contributions serve as a correction to the vertex-diffracted fields arising from the PO and PTD based integral contribution from the vertex and do not include the effect of the edge waves excited at the vertex. An approximate corner diffraction coefficient based on the geometrical theory of diffraction was first proposed by Burnside and Pathak [10]. The corner diffraction coefficient was derived by

asymptotically evaluating the radiation integral containing the GTD equivalent edge currents along the edge of a plane angular sector. It was demonstrated by Sikta *et al.* [11] that the corner diffraction contributions improve the accuracy of radar cross section (RCS) calculations. However, it was later shown by Michaeli [12] that this corner diffraction coefficient yields nonunique results for various scattering configurations. Furthermore, the resulting far field is discontinuous at the false shadow boundaries. In order to overcome this discrepancy, a corner diffraction coefficient was formulated by Brinkley and Marhefka [13] by employing the equivalent edge currents based on the PTD [14]. Since higher order interactions among the edges of the scatterer are not included in this formulation, the resulting corner diffraction coefficients provide an improvement only when the higher order contributions are negligible. A uniform geometrical theory of diffraction (UTD) solution for describing corner-diffracted fields was presented by Hill and Pathak [15], [16]. The corner diffraction coefficients were derived in the UTD format by asymptotically evaluating the plane wave spectral (PWS) representation of the total field scattered from a perfectly-conducting plane angular sector. Asymptotic evaluation of the PWS integral provides the Geometrical Optics (GO), edge- and corner-diffracted fields. The corner-diffracted fields compensate for the discontinuities in the edge-diffracted fields. More recently, end-point contributions were evaluated based on the incremental theory of diffraction (ITD) by Maci *et al.* [17]. It was shown that the inclusion of the vertex-diffracted currents leads to an accurate representation of the total current far from the vertex. However, the total current density predicted by incorporating the end-point effects fails when nose-on incidence is approached. In this case, the vertex-diffracted edge waves make a significant contribution to the scattered field. Thus, a more complete representation of the corner diffraction phenomenon should include the effect of vertex-diffracted edge waves. Towards this goal, Hansen [18] used the difference between the Method of

3

Moments (MoM) current density and the known high-frequency currents near the corner of a rectangular plate to characterize the behavior of vertex-diffracted currents. A similar approach was used in [19], [20] and [21] to derive diffraction coefficients for various scattering structures using the MoM analysis of finite bodies. Hansen's approach resulted in approximate analytical expressions for vertex diffraction coefficients for a quarter plane. However, these diffraction coefficients are valid over a very limited angular range of forward scattering directions for which only the first-order diffractions contribute to the scattered field. As a consequence, Hansen's formulation is not applicable to finite geometries. Thus, a corner diffraction coefficient that can be used in a purely high-frequency modeling of a 3-D scattering problem is yet to be determined.

In this thesis, we present the derivation of numerical diffraction coefficients for the vertex-diffracted edge waves at the tip of a plane angular sector. Based on the PTD, we express the total current on the surface as the sum of the physical optics current, the fringe wave currents (edge diffracted currents) from the two edges, and the vertex-diffracted current. The vertex-diffracted current for a given direction of incidence is obtained by subtracting the known PO and edge diffracted currents from the total current. The total current is calculated using the exact eigenfunction solution. This approach was previously used by Brinkley [22] for the same purpose. However, only the first-order fringe-wave contributions were used in calculating the vertex-diffracted currents. As a consequence, Brinkley's solution becomes inaccurate when higher order edge to edge interactions are present. In this thesis, up to second order edge-diffracted currents are used in the derivations. In order to obtain the double-diffracted FW currents, it is assumed that the second-order diffraction point is illuminated by the field launched at the first-order diffraction point. Assuming plane wave incidence at the second-order diffraction point, the double-diffracted current can easily be obtained by using the PTD formulation. This method was first introduced in the form of

equivalent edge currents in [23]. It should be noted that, in the present formulation we use the FW expressions that are derived from Sommerfeld's half plane solution [24] to account for edge diffractions. Since diffraction is a local phenomenon, each edge of the angular sector can be modeled as a half plane. However, as the diffraction point approaches the vertex, the effect of the truncation on edge-diffracted currents becomes substantial. This truncation effect is equivalent to the aforementioned end-point contributions. The vertex-diffracted currents not only account for the vertex-diffracted edge waves but also include the effect of these end-point contributions and serve as a correction to the FW currents. Once the known contributions are subtracted out from the total current, the remaining portion is interpreted as the vertex-diffracted current. The corner current is then expressed in the form of a wave traveling away from the vertex with unknown amplitude and decay factors. Using a least squares fit approximation, these unknown factors are obtained as a function of the angular position of the observation point with respect to the edge of the plane angular sector. It is demonstrated by numerical examples that the vertex-diffracted currents can be obtained with reasonable accuracy for an arbitrary direction of incidence even for very narrow angular sector openings. The accuracy of the vertex-diffracted currents are verified by comparisons with the exact current density. On the surface of a perfectly conducting polyhedral scatterer, the total high-frequency current is then calculated by superposing the PO current, the first and second order edge diffracted currents and the vertex-diffracted currents from the corners of the structure. In order to demonstrate the improvement provided by the inclusion of vertex-diffracted currents in the RCS calculations, the RCS pattern obtained by numerically integrating the total high-frequency current over the scattering structure is compared with the MoM results for various scattering configurations.

Due to the edge and corner conditions [25], the current and the charge densities exhibit strong singularities near the sharp edges and corners of a plane angular sector.

In a numerical solution, these singularities should be modeled properly for accurate results. A second aspect of this dissertation is the development of higher-order basis functions for the MoM solution. In the solution of integral equations by the MoM, higher-order basis functions provide a better representation of the actual current distribution, leading to a fast convergence and high accuracy. One of the most fundamental problems of interest is the modeling of singular currents near the sharp edges and corners of a scatterer. Wilton and Govind [26] studied the effect of edge singularities in the MoM solution for TM scattering from a strip. Richmond [27] showed that including the edge modes in the basis functions leads to considerable improvement in the convergence of the MoM solution. More recently, Brown and Wilton [28] developed triangular sub-domain basis functions that incorporate the edge singularities for three-dimensional cases involving perfectly-conducting infinitely-thin scatterers. Their basis functions can successfully model the singularity of the current component that is parallel to the edge. According to the edge condition, the component of the current density perpendicular to the edge remains finite as the edge is approached [25]. Specifically, for a half plane this component becomes zero at the edge. Hence, the perpendicular component of the current density cannot be modeled using the same set of basis functions as the parallel component. In [29], Andersson developed two kinds of rectangular sub-domain basis functions to account for the behavior of each component separately near the edges and at the tip of a 90° corner. Due to the extra degrees of freedom, these basis functions provide a better representation of the current density. However, the use of half-rooftop basis functions for the edge and corner elements introduces a discontinuity in the current density. A set of higher-order-complete basis functions for two-dimensional domains has been presented by Graglia *et al.* [30], [31]. A recent review of higher-order basis functions is available in [32].

In order to model the current density in the vicinity of the singular points (i.e.

sharp edges and corners), we develop a set of first-order divergence-conforming triangular patch basis functions with the correct edge and corner behaviors. The correct behavior of the current density near the edge of a wedge is described by $d^{\nu-1}$, where d is the perpendicular distance to the edge. The value of ν for different wedge angles can be obtained by requiring that the energy density be integrable near the edge [33]. Similarly, the behavior of the current density near the corner of a perfectly-conducting plane angular sector is defined by ρ^τ, where ρ is the distance to the corner. The value of τ for various angular sectors was obtained by Van Bladel [25] in a similar manner by enforcing the same integrability requirement near the corner of an angular sector. First-order basis functions have been studied previously in [34]. In order to obtain a better representation of the current density, each element edge is associated with two basis functions in the first-order basis function formulation. Therefore, for a given number of triangular patches, employing first-order basis functions leads to twice as many unknowns as compared to the standard Rao-Wilton-Glisson (RWG) [35] basis functions. However, it has been shown in [34] that first-order basis functions provide more accurate results compared to RWG basis functions for the same number of unknowns. First-order basis functions are actually simple decompositions of the standard RWG basis functions, and do not require additional computational load. The expressions for the edge and corner basis functions are constructed by imposing the known behavior of the true current density on the first order basis functions. Owing to six degrees of freedom provided by the first-order basis functions, it is possible to model both the parallel and the perpendicular components of the current density near the edges.

In order to validate the results, we consider the current density induced on a perfectly-conducting plane angular sector for plane wave incidence. The new basis functions are employed in a MoM solution to obtain the current density over a certain finite region around the corner of the plane angular sector. The current distribution

obtained using the MoM is not expected to agree with the exact solution. For instance, to find the current density over a 90° plane angular sector, we apply the MoM over a rectangular region near the corner of the angular sector. The truncation introduces three extraneous corners and two edges which act as new diffraction centers. In order to obtain an accurate representation of the current density due to one corner, the contributions from these diffraction centers should be eliminated from the MoM current. To accomplish this, the MoM current is expressed as the sum of complex exponential functions and the Matrix Pencil Method (MPM) [36], [37] is used to eliminate the extraneous contributions. We find that the resultant current distribution is indeed associated with a single corner by investigating its phase variation along different radial cuts around the corner. This method allows us to compare the current density obtained using the MoM with the exact solution at points very close to the edges and corners for a broad range of forward directions, providing a better insight on the performance of the basis functions.

This thesis is organized as follows: Chapter 2 presents the exact solution of the problem of electromagnetic scattering from a plane angular sector. The exact solution of the problem is of primary importance since the vertex diffraction coefficients are obtained by using the exact current density. Furthermore, the performance of the first-order-singular basis functions are also determined by comparisons with the exact current density near the vertex or edges of a plane angular sector. Chapter 3 investigates the behavior of the vertex-diffracted currents and presents the derivation of numerical vertex-diffraction coefficients. In Chapter 4, a new set of basis functions are derived to model the singular behavior of the current density near the vertex and the edges of a plane angular sector. Final discussions and conclusions are provided in Chapter 5.

Chapter 2

Current on a Plane Angular Sector

2.1 Introduction

This chapter presents the formulation of the exact solution for the problem of electromagnetic scattering from a perfectly conducting plane angular sector. The final solution of this 3-D vector problem is given in the form of a dyadic Green's function. The surface current density is then obtained by using the expressions for the magnetic field and the boundary conditions on the plane angular sector. The solution of the vector wave equation is based on the separation of variables in the uniformized sphero-conal coordinate system that was introduced by Kraus [38]. The sphero-conal coordinate system is described in Appendix A. In this chapter, the solution of the scalar wave equation and the computation of the eigenfunctions are presented in detail. The derivation of the dyadic Green's function is summarized in Appendix B. In Section 2.2, the solution of the scalar wave equation is summarized first. Then, the numerical procedure used to obtain the scalar wave functions is described in detail. Finally, the exact current density induced on the surface of the angular sector is compared with the current density obtained using the PTD to investigate the behavior

of the vertex-diffracted currents.

2.2   Scalar Helmholtz Equation in the Sphero-conal Coordinate System

Within a linear, homogeneous, isotropic and source-free region the E-field vector satisfies the homogeneous vector Helmholtz equation given by

$$\nabla \times \nabla \times \bar{E} - \kappa^2 \bar{E} = 0 \qquad (2.1)$$

where κ denotes the wave number. Eq. (2.1) must be solved subject to the boundary conditions $\hat{n} \times \bar{E} = 0$ on the surface of the plane angular sector and the radiation condition. The vector solutions of (2.1) can be constructed as

$$\bar{M} = \nabla \times \psi \bar{p} \qquad (2.2)$$

$$\bar{N} = \frac{1}{\kappa} \nabla \times \nabla \times \psi \bar{p} \qquad (2.3)$$

where $\bar{p}$ denotes a constant vector and the scalar function ψ is a solution of the scalar Helmholtz equation

$$\nabla^2 \psi + \kappa^2 \psi = 0. \qquad (2.4)$$

$\bar{p}$ and ψ are termed as the piloting vector and the generating function respectively [39]. Eq. (2.4) follows directly from (2.1) by substituting (2.2) and (2.3).

In the sphero-conal coordinates the pivoting vector $\bar{p}$ is chosen to be equal to $\bar{r}$ and the two independent vector solutions are defined as

$$\bar{M}_2 = \nabla \times \psi_2 \bar{r} \qquad (2.5)$$

$$\bar{N}_1 = \frac{1}{\kappa} \nabla \times \nabla \times \psi_1 \bar{r}. \qquad (2.6)$$

Enforcing the boundary condition $\hat{n} \times \bar{M}_2 = 0$ and $\hat{n} \times \bar{N}_1 = 0$ on the surface of the plane angular sector, it is found that ψ_1 and ψ_2 must satisfy the Dirichlet and
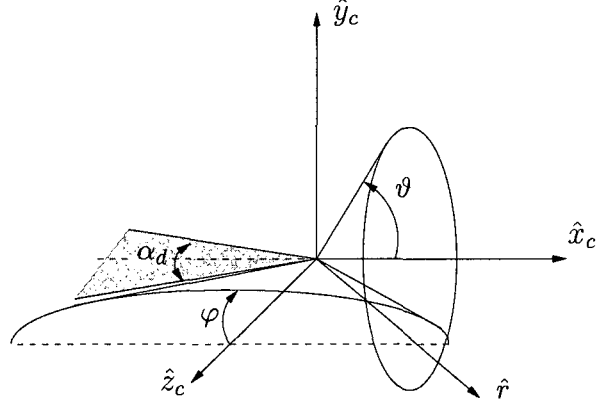
Figure 2.1: Sphero-conal coordinate system and the plane angular sector.

Neumann boundary conditions respectively. The solution of the scalar Helmholtz equation is expressed as

$$\psi(r, \vartheta, \varphi) = R(r)T(\vartheta)P(\varphi) \tag{2.7}$$

where (r, ϑ, φ) denote the sphero-conal coordinates as depicted in Fig. 2.1. Substituting this solution in (2.4) and dividing by $R(r)T(\vartheta)P(\varphi)$, the wave equation becomes

$$
\frac{1}{k^2 \sin^2 \vartheta + k'^2 \sin^2 \varphi} \left[\frac{\sqrt{1 - k^2 \cos^2 \vartheta}}{T(\vartheta)} \frac{\partial}{\partial \vartheta} (\sqrt{1 - k^2 \cos^2 \vartheta} \frac{dT(\vartheta)}{d\vartheta}) \right.
$$
$$
\left. + \frac{\sqrt{1 - k'^2 \cos^2 \varphi}}{P(\varphi)} \frac{\partial}{\partial \varphi} (\sqrt{1 - k'^2 \cos^2 \varphi} \frac{dP(\varphi)}{d\varphi}) \right] \tag{2.8}
$$
$$
+ \frac{1}{R(r)} \left[\frac{\partial}{\partial r} (r^2 \frac{dR(r)}{dr}) \right] + \kappa^2 r^2 = 0.
$$

Using a separation constant $\nu(\nu + 1)$, (2.8) is separated into two differential equations given by

$$[\frac{d}{dr}(r^2 \frac{dR(r)}{dr})] + R(r)[r^2 \kappa^2 - \nu(\nu + 1)] = 0 \tag{2.9}$$

$$\frac{\sqrt{1 - k^2 \cos^2 \vartheta}}{T(\vartheta)} \frac{\partial}{\partial \vartheta} (\sqrt{1 - k^2 \cos^2 \vartheta} \frac{dT(\vartheta)}{d\vartheta}) + k^2 \sin^2 \vartheta \nu(\nu + 1)$$

$$+ \frac{\sqrt{1 - k'^2 \cos^2 \varphi}}{P(\varphi)} \frac{\partial}{\partial \varphi} (\sqrt{1 - k'^2 \cos^2 \varphi} \frac{dP(\varphi)}{d\varphi}) + k'^2 \sin^2 \varphi \nu(\nu + 1) = 0. \tag{2.10}$$

Eq. (2.9) is the spherical Bessel equation with two solutions, $j_\nu(\kappa r)$ and $h_\nu^{(2)}(\kappa r)$. Here, $j_\nu(\kappa r)$ satisfies the continuity at the vertex of the plane angular sector and

11

$h_\nu^{(2)}(\kappa r)$ satisfies the radiation condition as $r \to \infty$. Using the separation of variables method once again with a separation constant μ, (2.10) separates as

$$\sqrt{1 - k^2 \cos^2 \vartheta}\, \frac{\partial}{\partial \vartheta}(\sqrt{1 - k^2 \cos^2 \vartheta}\, \frac{dT(\vartheta)}{d\vartheta}) + (k^2 \sin^2 \vartheta \nu(\nu + 1) + \mu)T(\vartheta) = 0 \quad (2.11)$$

$$\sqrt{1 - k'^2 \cos^2 \varphi}\, \frac{\partial}{\partial \varphi}(\sqrt{1 - k'^2 \cos^2 \varphi}\, \frac{dP(\varphi)}{d\varphi}) + (k'^2 \sin^2 \varphi \nu(\nu + 1) - \mu)P(\varphi) = 0. \quad (2.12)$$

The resulting are the trigonometric forms of spherical Lamé differential equations. These differential equations must be solved subject to the Dirichlet and Neumann boundary conditions and the "matching conditions." Referring to the problem geometry in Fig. 2.1, the matching conditions imposed by the sphero-conal coordinate system can be summarized as follows:

- Any single-valued function must be periodic in φ

$$\psi(r, \vartheta, \varphi) = \psi(r, \vartheta, \varphi + 2\pi). \tag{2.13}$$

- A given point on the plane $\vartheta = 0°$ must be uniquely defined. Thus

$$\psi(r, \vartheta = 0, \varphi) = \psi(r, \vartheta = 0, -\varphi). \tag{2.14}$$

- When crossing the plane $\vartheta = 0°$, $\hat{\vartheta}$ changes direction. To satisfy the continuity of $\nabla\psi(r, \vartheta = 0, \varphi)$,

$$\frac{\partial}{\partial \vartheta}\psi(r, 0, \varphi) = -\frac{\partial}{\partial \vartheta}\psi(r, 0, -\varphi). \tag{2.15}$$

In order to determine the matching conditions on the eigenfunctions, $T(\vartheta)$ and $P(\varphi)$ are expressed in terms of even and odd parts

$$T(\vartheta) = T_e(\vartheta) + T_o(\vartheta) \tag{2.16}$$

$$P(\varphi) = P_e(\varphi) + P_o(\varphi) \tag{2.17}$$

where even and odd parts are defined such that $T'_e(0) = P'_e(0) = 0$ for the even parts and $T_o(0) = P_o(0) = 0$ for the odd parts. Using (2.16) in (2.14), it can be shown that

$$T_e(0)P_o(\varphi) = -T_e(0)P_o(\varphi) \tag{2.18}$$

12

which implies that either $P_o(\varphi) = 0$ or $T_e(0) = 0$. The first condition means that $P(\varphi)$ is even. The second condition along with the definition $T'_e(0) = 0$ implies that $T_e(\vartheta) = 0$. Thus, (2.18) requires that either $P(\varphi)$ is even or $T(\vartheta)$ is odd. Similarly it follows from (2.17) and (2.15) that

$$T'_o(0)P_e(\varphi) = -T'_o(0)P_e(\varphi). \tag{2.19}$$

This implies that either $T'_o(0) = 0$ or $P_e(\varphi) = 0$. The second condition simply means that $P(\varphi)$ is odd. It follows from the first condition and the definition $T_o(0) = 0$ that $T_o(\vartheta) = 0$. Thus, (2.19) implies that either $T(\vartheta)$ is even or $P(\varphi)$ is odd. Combining the results from (2.18) and (2.19), it can be deduced that $T(\vartheta)$ and $P(\varphi)$ are both even or both odd. Thus, the solution of (2.4) can be expressed as

$$\psi(r, \vartheta, \varphi) = R(r) \begin{cases} T_e(\vartheta)P_e(\varphi) \\ T_o(\vartheta)P_o(\varphi) \end{cases} \tag{2.20}$$

where, the radial function $R(r)$ is the solution of (2.9) as described above. To be able to verify the resulting eigenfunctions and the eigenvalue pairs with the previously published results, the eigenfunctions are normalized as in [1] such that

$$P_e(0) = T_e(0) = 1 \tag{2.21}$$

$$P'_o(0) = T'_o(0) = 1. \tag{2.22}$$

Even and odd solutions of (2.11) and (2.12) must be obtained subject to the Dirichlet and Neumann boundary conditions given by

$$T_{e,o}(\pi) = 0 \tag{2.23}$$

$$T'_{e,o}(\pi) = 0 \tag{2.24}$$

respectively. The solutions of (2.11) and (2.12) are in general periodic Lamé functions. The form of the eigenfunctions can be determined starting from the boundary and the matching conditions. These eigenfunctions are expressed in terms of Fourier series

13

expansions. The solutions of the φ Lamé equation (2.12) are well known [40], [41]. Based on the periodicity and the normalization conditions on $P_{e,o}(\varphi)$, four types of eigenfunctions can be defined. For a plane angular sector, the solutions of the ϑ Lamé equation (2.11) can be obtained in a similar manner using the boundary conditions (2.23) and (2.24) and the matching conditions. The four independent solutions of the φ and ϑ Lamé equations are listed in Table 2.1. The subscripts 1 and 2 of the functions T and P are used in Table 2.1 to specify that the associated expansion is the solution of the Dirichlet and Neumann problems respectively. The superscripts are used to identify the type of the eigenfunctions.

Table 2.1: Eigenfunction expansions

	Dirichlet	Neumann
even	$T_{e1}^{(1)}(\vartheta) = \sum\limits_{m=-\infty}^{\infty} A_m^{(e1)} \cos[(2m - 0.5)\vartheta]$	$T_{e2}^{(1)}(\vartheta) = \sum\limits_{m=0}^{\infty} A_{2m+1}^{(e2)} \cos[(2m + 1)\vartheta]$ $T_{e2}^{(2)}(\vartheta) = \sum\limits_{m=0}^{\infty} A_{2m}^{(e2)} \cos[2m\vartheta]$
even	$P_{e1}^{(1)}(\varphi) = \sum\limits_{m=0}^{\infty} B_{2m}^{(e1)} \cos[2m\varphi]$ $P_{e1}^{(2)}(\varphi) = \sum\limits_{m=0}^{\infty} B_{2m+1}^{(e1)} \cos[(2m + 1)\varphi]$	$P_{e2}^{(1)}(\varphi) = \sum\limits_{m=0}^{\infty} B_{2m+1}^{(e2)} \cos[(2m + 1)\varphi]$ $P_{e2}^{(2)}(\varphi) = \sum\limits_{m=0}^{\infty} B_{2m}^{(e2)} \cos[2m\varphi]$
odd	$T_{o1}^{(1)}(\vartheta) = \sum\limits_{m=0}^{\infty} A_{2m+1}^{(o1)} \sin[(2m + 1)\vartheta]$ $T_{o1}^{(2)}(\vartheta) = \sum\limits_{m=1}^{\infty} A_{2m}^{(o1)} \sin[2m\vartheta]$	$T_{o2}^{(1)}(\vartheta) = \sum\limits_{m=-\infty}^{\infty} A_m^{(o2)} \sin[(2m - 0.5)\vartheta]$
odd	$P_{o1}^{(1)}(\varphi) = \sum\limits_{m=0}^{\infty} B_{2m+1}^{(o1)} \sin[(2m + 1)\varphi]$ $P_{o1}^{(2)}(\varphi) = \sum\limits_{m=1}^{\infty} B_{2m}^{(o1)} \sin[2m\varphi]$	$P_{o2}^{(1)}(\varphi) = \sum\limits_{m=1}^{\infty} B_{2m}^{(o2)} \sin[2m\varphi]$ $P_{o2}^{(2)}(\varphi) = \sum\limits_{m=0}^{\infty} B_{2m+1}^{(o2)} \sin[(2m + 1)\varphi]$

The eigenvalue pairs (ν, μ) and the unknown coefficients in the eigenfunction expansions can be obtained by simultaneously solving (2.11) and (2.12). To accomplish this, the eigenfunction expansions are first substituted in the associated differential equations, resulting in matrix eigenvalue equations for each expansion. These eigenvalue equations are then solved simultaneously to calculate the eigenvalue pairs and the expansion coefficients. In what follows, we describe this procedure and provide the resulting matrix eigenvalue equation for each eigenfunction expansion.

Using the series expansion of $T_{e1}^{(1)}(\vartheta)$, it follows from (2.11) that

$$
\sum_{m=-\infty}^{\infty} \left\{ \frac{k^2}{4} A_m^{(e1)} \left[\frac{(4m-1)(4m+1)}{4} - \nu(\nu+1) \right] sin[(2m+\frac{3}{2})\vartheta] \right.
$$
$$
+ \frac{k^2}{4} A_m^{(e1)} \left[\frac{(4m-1)(4m-3)}{4} - \nu(\nu+1) \right] sin[(2m-\frac{5}{2})\vartheta] \tag{2.25}
$$
$$
\left. + A_m^{(e1)} \left[\mu + (\frac{k^2}{2}-1)\frac{(4m-1)^2}{4} + \frac{k^2\nu(\nu+1)}{2} \right] sin[(2m-\frac{1}{2})\vartheta] \right\} = 0.
$$

This equation can be rearranged to give

$$
\sum_{m=-\infty}^{\infty} \left\{ A_{m-1}^{(e1)} a_m + A_m(b_m + \mu) + A_{m+1}^{(e1)} c_m \right\} sin[(2m-\frac{1}{2})\vartheta] = 0 \tag{2.26}
$$

where

$$
a_m = \frac{k^2}{4} \left[\frac{(4m-5)(4m-3)}{4} - \nu(\nu+1) \right] \tag{2.27}
$$

$$
b_m = \left[(\frac{k^2}{2}-1)\frac{(4m-1)^2}{4} + \frac{k^2\nu(\nu+1)}{2} \right] \tag{2.28}
$$

$$
c_m = \frac{k^2}{4} \left[\frac{(4m+3)(4m+1)}{4} - \nu(\nu+1) \right]. \tag{2.29}
$$

In order to solve for the unknown coefficients $A_m^{(e1)}$, (2.26) is written in matrix form

as

$$
\begin{pmatrix}
\ddots & & & & & \\
\hline
a_{-2} & b_{-2} & c_{-2} & 0 & 0 & 0 \\
0 & a_{-1} & b_{-1} & c_{-1} & 0 & 0 \\
0 & 0 & a_0 & b_0 & c_0 & 0 \\
0 & 0 & 0 & a_1 & b_1 & c_1 \\
\hline
& & & & & \ddots
\end{pmatrix}
\begin{pmatrix}
\vdots \\
A_{-3}^{(e1)} \\
A_{-2}^{(e1)} \\
A_{-1}^{(e1)} \\
A_0^{(e1)} \\
A_1^{(e1)} \\
A_2^{(e1)} \\
\vdots
\end{pmatrix}
= -\mu
\begin{pmatrix}
\vdots \\
A_{-3}^{(e1)} \\
A_{-2}^{(e1)} \\
A_{-1}^{(e1)} \\
A_0^{(e1)} \\
A_1^{(e1)} \\
A_2^{(e1)} \\
\vdots
\end{pmatrix} .
\tag{2.30}
$$

The resulting is a matrix eigenvalue problem of the form $\bar{A} \cdot \bar{x} = -\mu\bar{x}$ with the eigenvector $\bar{x} = [...A_{-1}^{(e1)} A_0^{(e1)} A_1^{(e1)}...]^T$ and the eigenvalue $-\mu$. It is noted that $\bar{x}$, μ and ν are the unknowns to be determined. Since the matrix elements in (2.30) are functions of ν, the eigensystem can be solved for a given ν. Eq. (2.10), which is a two-dimensional Sturm-Lioville equation, is known to be self adjoint and positive definite. Thus, ν is positive for every eigenfunction expansion. Then, the eigenvalue (i. e. $-\mu$) in (2.30) is calculated for a discrete set of ν values starting from $\nu = 0$. As a result, a set of eigenvalue pairs (ν_q, μ_q) is obtained. In order to be able calculate μ_q for a given ν_q, the matrix has to be truncated. The size of this truncation can be determined depending on the values of the elements of the eigenvector $\tilde{x}$. The truncated matrix is in the form of a real Hessenberg matrix and the resulting system can easily be solved using a QR algorithm [42].

Substituting the series expansion for $P_{e1}^{(1)}(\varphi)$, (2.12) can be written as

$$
B_0^{(e1)}(b_0 - \mu) + B_2^{(e1)} c_0 + \sum_{m=1}^{\infty} \left\{ B_{2m-2}^{(e1)} a_{2m} + B_{2m}^{(e1)}(b_{2m} - \mu) + B_{2m+2}^{(e1)} c_{2m} \right\} \cos(2m\varphi) = 0
\tag{2.31}
$$

where

$$a_{2m} = \begin{cases} -\dfrac{k'^2 \nu(\nu+1)}{2}, & m = 1 \\ \dfrac{k'^2}{4}\left[(2m-2)(2m-1) - \nu(\nu+1)\right], & m \neq 1 \end{cases} \tag{2.32}$$

$$b_{2m} = \left[4m^2\left(\dfrac{k'^2}{2} - 1\right) + \dfrac{k'^2\nu(\nu+1)}{2}\right] \tag{2.33}$$

$$c_{2m} = \dfrac{k'^2}{4}\left[(2m+2)(2m+1) - \nu(\nu+1)\right]. \tag{2.34}$$

Therefore, the eigenvalue pairs for $P_{e1}^{(1)}(\varphi)$ are the solutions of

$$\left(\begin{array}{ccccc|c} b_0 & c_0 & 0 & 0 & 0 & 0 \\ a_2 & b_2 & c_2 & 0 & 0 & 0 \\ 0 & a_4 & b_4 & c_4 & 0 & 0 \\ 0 & 0 & a_6 & b_6 & c_6 & 0 \\ 0 & 0 & 0 & a_8 & b_8 & c_8 \\ \hline & & & & & \ddots \end{array} \right) \left(\begin{array}{c} B_0^{(e1)} \\ B_2^{(e1)} \\ B_4^{(e1)} \\ B_6^{(e1)} \\ B_8^{(e1)} \\ \vdots \end{array} \right) = \mu \left(\begin{array}{c} B_0^{(e1)} \\ B_2^{(e1)} \\ B_4^{(e1)} \\ B_6^{(e1)} \\ B_8^{(e1)} \\ \vdots \end{array} \right). \tag{2.35}$$

Similarly for $P_{e1}^{(2)}(\varphi)$, the eigenvalue problem can be written as

$$\left(\begin{array}{ccccc|c} b_1 & c_1 & 0 & 0 & 0 & 0 \\ a_3 & b_3 & c_3 & 0 & 0 & 0 \\ 0 & a_5 & b_5 & c_5 & 0 & 0 \\ 0 & 0 & a_7 & b_7 & c_7 & 0 \\ 0 & 0 & 0 & a_9 & b_9 & c_9 \\ \hline & & & & & \ddots \end{array} \right) \left(\begin{array}{c} B_1^{(e1)} \\ B_3^{(e1)} \\ B_5^{(e1)} \\ B_7^{(e1)} \\ B_9^{(e1)} \\ \vdots \end{array} \right) = \mu \left(\begin{array}{c} B_1^{(e1)} \\ B_3^{(e1)} \\ B_5^{(e1)} \\ B_7^{(e1)} \\ B_9^{(e1)} \\ \vdots \end{array} \right) \tag{2.36}$$

where the matrix elements are given by

$$a_{2m+1} = \dfrac{k'^2}{4}\left[(2m-1)2m - \nu(\nu+1)\right] \tag{2.37}$$

$$b_{2m+1} = \begin{cases} \left[\left(\dfrac{k'^2}{2} - 1\right) + \dfrac{k'^2\nu(\nu+1)}{4}\right], & m = 0 \\ \left[(2m+1)^2\left(\dfrac{k'^2}{2} - 1\right) + \dfrac{k'^2\nu(\nu+1)}{2}\right], & m \neq 0 \end{cases} \tag{2.38}$$

$$c_{2m+1} = \dfrac{k'^2}{4}\left[(2m+2)(2m+3) - \nu(\nu+1)\right]. \tag{2.39}$$

17

Using (2.20), the two solutions of the even Dirichlet problem can be expressed as

$$\psi_{e1}^{(1)}(r, \vartheta, \varphi) = R_{e1}(r) T_{e1}^{(1)}(\vartheta) P_{e1}^{(1)}(\varphi) \tag{2.40}$$

$$\psi_{e1}^{(2)}(r, \vartheta, \varphi) = R_{e1}(r) T_{e1}^{(1)}(\vartheta) P_{e1}^{(2)}(\varphi) \tag{2.41}$$

where the subscript "e1" is used to specify that the functions are the solutions of the even Dirichlet problem. The corresponding eigenvalue pairs are denoted by (ν_{e1}, μ_{e1}). For (2.40), the eigenvalue pairs are calculated by simultaneously solving (2.30) and (2.35). Similarly, the eigenvalue pairs for (2.41) are given by the simultaneous solutions of (2.30) and (2.36).

Using the same procedure for the odd Neumann problem, it can be shown that the eigenvalue pairs for $T_{o2}^{(1)}(\vartheta)$ can be calculated using (2.30) and (2.27)-(2.29). Substituting the expression for $P_{o2}^{(1)}(\varphi)$ in (2.12), it is found that the corresponding eigenvalue problem can be expressed as

$$
\left(\begin{array}{ccccc|c}
b_2 & c_2 & 0 & 0 & 0 & 0 \\
a_4 & b_4 & c_4 & 0 & 0 & 0 \\
0 & a_6 & b_6 & c_6 & 0 & 0 \\
0 & 0 & a_8 & b_8 & c_8 & 0 \\
0 & 0 & 0 & a_{10} & b_{10} & c_{10} \\
\hline
 & & & & & \ddots
\end{array}\right)
\left(\begin{array}{c}
B_2^{(e1)} \\
B_4^{(e1)} \\
B_6^{(e1)} \\
B_8^{(e1)} \\
B_{10}^{(e1)} \\
\vdots
\end{array}\right)
= \mu
\left(\begin{array}{c}
B_2^{(e1)} \\
B_4^{(e1)} \\
B_6^{(e1)} \\
B_8^{(e1)} \\
B_{10}^{(e1)} \\
\vdots
\end{array}\right)
\tag{2.42}
$$

where the matrix elements are given by (2.32)-(2.34).

Similary, for $P_{o2}^{(2)}(\varphi)$ the eigenvalue problem is given by (2.36). The matrix elements in this case can be calculated using (2.37), (2.39) and

$$b_{2m+1} = \begin{cases} \left[\left(\frac{k'^2}{2} - 1 \right) + \frac{3k'^2 \nu(\nu+1)}{4} \right], & m = 0 \\ \left[(2m+1)^2 \left(\frac{k'^2}{2} - 1 \right) + \frac{k'^2 \nu(\nu+1)}{2} \right], & m \neq 0. \end{cases} \tag{2.43}$$

18

Therefore, using (2.20), the two solutions of the odd Neumann problem can be expressed as

$$\psi_{o2}^{(1)}(r, \vartheta, \varphi) = R_{o2}(r) T_{o2}^{(1)}(\vartheta) P_{o2}^{(1)}(\varphi) \tag{2.44}$$

$$\psi_{o2}^{(2)}(r, \vartheta, \varphi) = R_{o2}(r) T_{o2}^{(1)}(\vartheta) P_{o2}^{(2)}(\varphi) \tag{2.45}$$

where the subscript "o2" is used to specify that the functions are the solutions of the odd Neumann problem. The corresponding eigenvalue pairs are denoted by (ν_{o2}, μ_{o2}). For (2.44), the eigenvalue pairs are calculated by simultaneously solving (2.30) and (2.42). Similarly, the eigenvalue pairs for (2.45) are given by the simultaneous solutions of (2.30) and (2.36) with the matrix elements defined by (2.37), (2.39) and (2.43).

2.3 Numerical Computation of the Eigenvalue Pairs

In order to illustrate the application of the procedure described above, the eigenvalue pairs (ν_{o2}, μ_{o2}) for the odd Neumann problem for a plane angular sector of 30° are calculated in this section. First, starting from $\nu = 0$ the corresponding values of μ are calculated for several values of ν at constant intervals using (2.30). For a given value of ν, there are infinite number of μ's which satisfy (2.11) and (2.12). In the numerical calculations, we set the size of the matrix in (2.30) to N_f. Thus for a given ν, the solution of the eigenvalue problem (2.30) leads to N_f eigenvalues. This also means that N_f is the number of terms to be used in the eigenfunction expansions in Table 2.1. The corresponding ν vs μ curves are shown in Fig. 2.2. In this case, the infinite series expansion of $T_{o2}^{(1)}$ is terminated after 11 terms $(-5 \leq m \leq 5)$. Thus, the resulting matrix equation is an 11 × 11 eigensystem. Starting from $\nu = 0$, 11 eigenvalues are calculated at a constant interval $\Delta \nu = 0.01$ until $\nu = 15$. As a result 11 curves (continuous line), along which the eigenvalue pairs (ν_{o2}, μ_{o2}) satisfy (2.11)
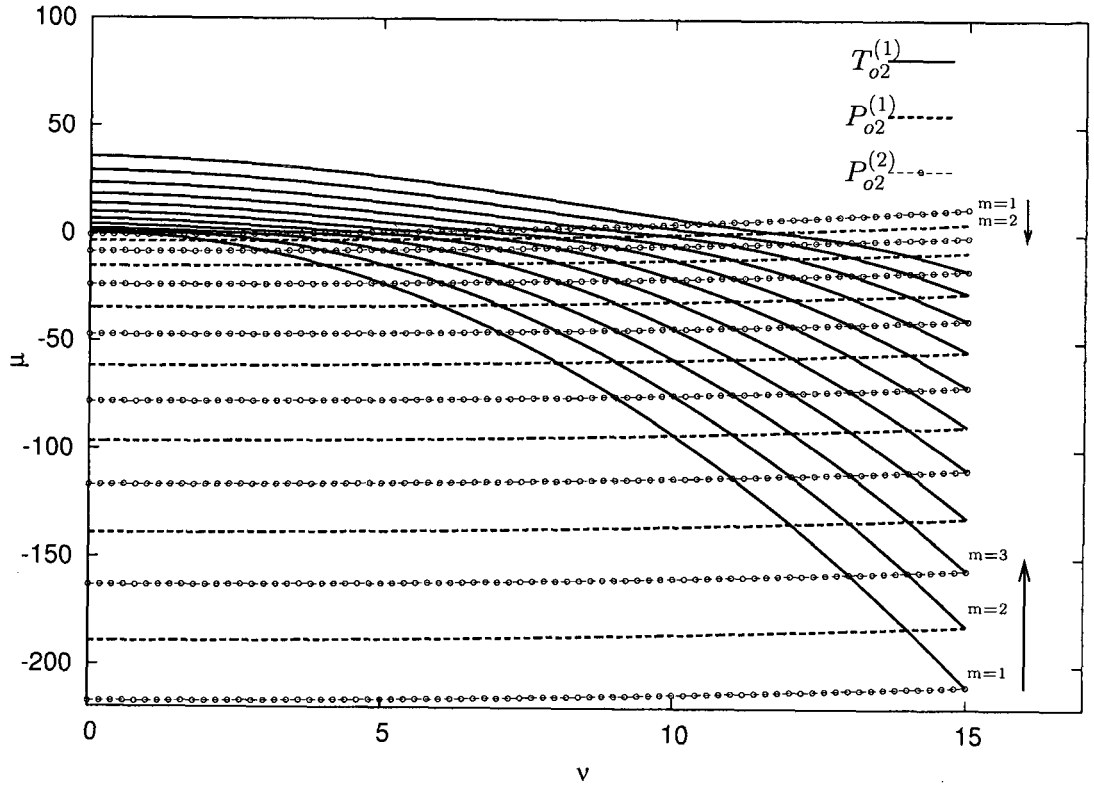
Figure 2.2: Eigenvalue curves for the odd Neumann problem for a plane angular sector of $\alpha_d = 30°$.

are obtained. In order to obtain the eigenvalue pairs that also satisfy (2.12), the same procedure is repeated using the matrix equations (2.42) and (2.36) that correspond to eigenfunction expansions $P_{o2}^{(1)}$ and $P_{o2}^{(2)}$ respectively. The ν vs μ curves associated with $P_{o2}^{(1)}$ (dashed) and $P_{o2}^{(2)}$ (other) are also shown in Fig. 2.2. Intersections of these curves are the eigenvalue pairs that satisfy both (2.11) and (2.12). The intersections of the ν vs μ curves can be calculated numerically.

The first 80 eigenvalue pairs for the even Neumann and the odd Dirichlet problems associated with various vertex angles are listed in Appendix C. Once the eigenvalue pairs are calculated, the corresponding eigenvectors can be obtained by substituting these eigenvalue pairs back into the corresponding matrix eigenvalue equations.

20

2.4 Current Density for Plane Wave Illumination

The current density on a plane angular sector due to a unit dipole source is given by (B-25). Substituting (2.7) in (2.5) and performing the curl operations, it can be shown that

$$\bar{M}_q(\bar{r}) = R_q(r)\bar{m}_q(\vartheta, \varphi) \tag{2.46}$$

$$\bar{N}_q(\bar{r}) = \frac{R_q(r)}{\kappa r}\bar{\ell}_q + \frac{[rR_q(r)]'}{\kappa r}[\hat{r} \times \bar{m}_q(\vartheta, \varphi)] \tag{2.47}$$

where the subscript q stands for 1 or 2, which correspond to even and odd Dirichlet or Neumann problems respectively. The primes imply differentiation with respect to the independent variables r, ϑ and φ. The vectors $\bar{m}_q$ and $\bar{\ell}_q$ are given by

$$\bar{m}_q(\vartheta, \varphi) = \hat{\varphi}\frac{r}{s_\vartheta}T_q'(\vartheta)P_q(\varphi) - \hat{\vartheta}\frac{r}{s_\varphi}T_q(\vartheta)P_q'(\varphi) \tag{2.48}$$

$$\bar{\ell}_q(\vartheta, \varphi) = \nu_q(\nu_q + 1)T_q(\vartheta)P_q(\varphi)\hat{r}. \tag{2.49}$$

where the metric coefficients s_ϑ and s_φ are given by (A-5) and (A-6). In (2.46) and (2.47), the superscripts for $\bar{M}_q$ and $\bar{N}_q$ are omitted for clarity. In Appendix B, the superscripts (1) and (2) are used to specify the type of the radial function $R_q(r)$ as defined by (B-7)-(B-10). In order to obtain the current expression for plane wave incidence, large argument forms of the source terms involving spherical Hankel functions are used. In (B-25), the source terms are

$$\bar{M}_{on2}^{(2)}(r') = h_{\nu n2}^{(2)}(\kappa r')\bar{m}_{on2} \tag{2.50}$$

$$\bar{N}_{en1}^{(2)}(\bar{r}') = \frac{h_{\nu n1}^{(2)}(\kappa r')}{\kappa r'}\bar{\ell}_{en1} + \frac{\frac{d}{dr'}(r'h_{\nu n1}^{(2)}(\kappa r'))}{\kappa r'}(\hat{r}' \times \bar{m}_{en1}) \tag{2.51}$$

where the subscripts "on2" and "en1" are used instead of q. It should be noted that this is necessary to be able to uniquely specify each function. For instance, "on2" denotes that the eigenfunctions to be used in evaluating $\bar{m}_q$ are the solutions of the odd Neumann problem (i. e. $T_{o2}^{(1)}$ and $P_{o2}^{(1)}$, $P_{o2}^{(2)}$) that are associated with the nth eigenvalue pair (ν_{on2}, μ_{on2}).

The spherical Bessel function can asymptotically be expressed as

$$h_\nu^{(2)}(\kappa r') \sim j^{\nu+1}\frac{e^{-j\kappa r'}}{\kappa r'}.$$ (2.52)

Using (2.52) in (2.50) and (2.51), and substituting in (B-25), the expression for the current density as $r' \to \infty$ can be written as

$$\bar{J}(\bar{r}) = -\frac{E_a^i}{15}\sum_{n=1}^{\infty} \ j^{\nu_{on2}+1}\bar{m}_{on2}(\vartheta_0,\varphi_0)\cdot\hat{a}\frac{T_{on2}(\pi)}{\Lambda_{on2}}$$

$$\left\{ -\nu_{on2}(\nu_{on2}+1)\frac{j_{\nu_{on2}}(\kappa r)}{\kappa r}P_{on2}(\varphi)\hat{\varphi} \right.$$

$$+\frac{\frac{d}{dr}(rj_{\nu_{on2}}(\kappa r))}{\kappa r sin\varphi}\sqrt{1+sin^2\varphi}P'_{on2}(\varphi)\hat{r}\right\}$$

$$+j^{\nu_{en1}}[\hat{r}_0\times\bar{m}_{en1}(\vartheta_0,\varphi_0)]\cdot\hat{a}\frac{j_{\nu_{en1}}(\kappa r)}{\Lambda_{en1}sin\varphi}T'_{en1}(\pi)P_{en1}(\varphi)\hat{r} \quad (2.53)$$

where the incident field vector at the vertex was identified as

$$\bar{E}^i = \hat{a}E_a^i = \hat{a}\frac{e^{-j\kappa r'}}{4\pi r'}.$$

(a)   (b)
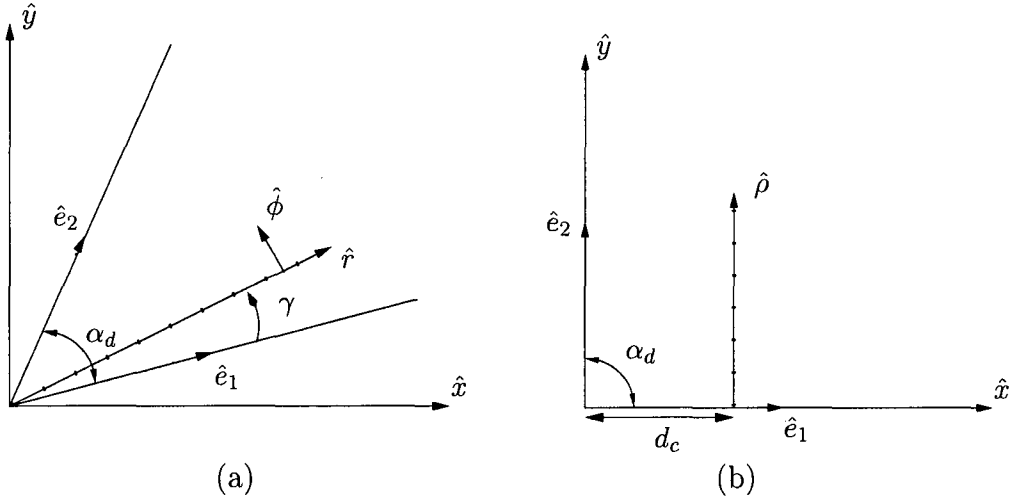
Figure 2.3: (a) Plane angular sector of $\alpha_d \leq 90°$. The angular sector is centered in the first quadrant of the x-y plane so that $\hat{e}_1\cdot\hat{x} = \hat{e}_2\cdot\hat{y}$. (b) Plane angular sector of $\alpha_d = 90°$ on the x-y plane and the current density path perpendicular to the edge.

In the numerical calculations, the infinite sum in the current expression is terminated after N_c terms. In order to determine N_c, a convergence test should be carried

22
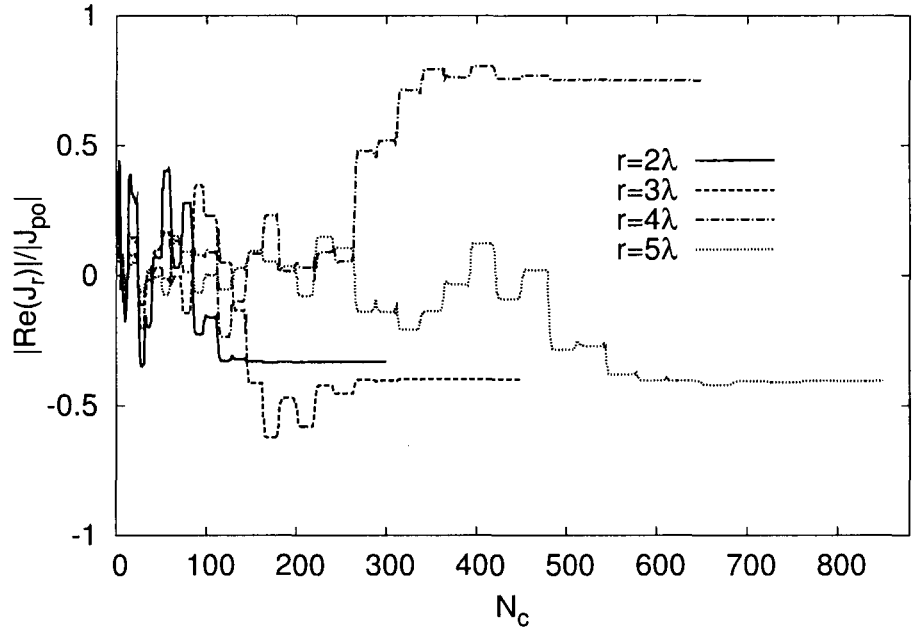
(a)
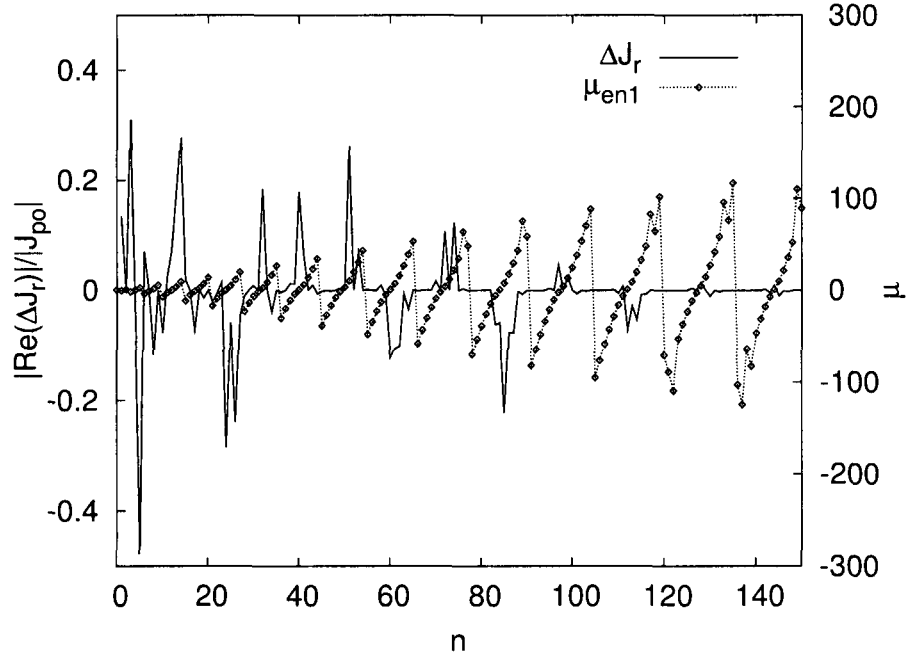
(b)

Figure 2.4: (a) $Re\{J_r\}$ as a function of the number of terms used in the current expression. (b) $Re\{\Delta J_r\}$ and μ_{en1} as a function of the summation index n. ΔJ_r represents the contribution from each term in the current expression given by (2.53). The current density on a plane angular sector of $\alpha_d = 90°$ is evaluated at $(\gamma, r) = (0.5°, 2\lambda)$ for a $\hat{\theta}_i$ polarized plane wave incidence from the direction $(\theta_i, \phi_i) = (30°, 225°)$.

23

Table 2.2: Number of terms sufficient for convergence in the evaluation of the current density. r is the radial distance measured from the vertex. N_f is the number of terms used in the eigenfunction expansions. N_c is the number of terms used in the current expression.

r (λ)	N_f	N_c
1.0	13	130
1.5	15	152
2.0	23	228
2.5	25	321
3.0	29	370
4.0	35	618
5.0	43	850
6.0	53	1159
8.0	67	2119
10.0	81	2969

out. Convergence is assumed when the consecutive terms in the series in (2.53) differed in less than 0.1%. The number of terms sufficient to obtain convergence for various radial distances are shown in Table 2.2. Each eigenvalue pair (ν_n, μ_n) that is obtained by finding the intersection of the ν vs μ curves as in Fig. 2.2 is associated with a term in the summation in (2.53). It should be noted that (2.53) is formulated such that the summation is over all the eigenfunctions in no particular order. Thus, this series expression can be evaluated in various ways. Consider the ν vs μ curves for $T_{o2}^{(1)}$ in Fig. 2.2 (continuous line). For the given range of ν, there are 15 eigenvalue pairs on the $m = 1$ curve. Once these 15 eigenvalue pairs are obtained, the corresponding 15 terms in the current expression can be calculated. Then the same procedure can be repeated for the remaining ν vs μ curves (m=2, 3, 4 etc.) until the series converges. Another approach is to sort the terms in the series in (2.53) with respect to the value of the associated eigenvalue pair. In our calculations, we use

the latter approach. The eigenvalue pairs are sorted with respect to ν_n starting with the smallest value and the summation in (2.53) is terminated after N_c terms. The
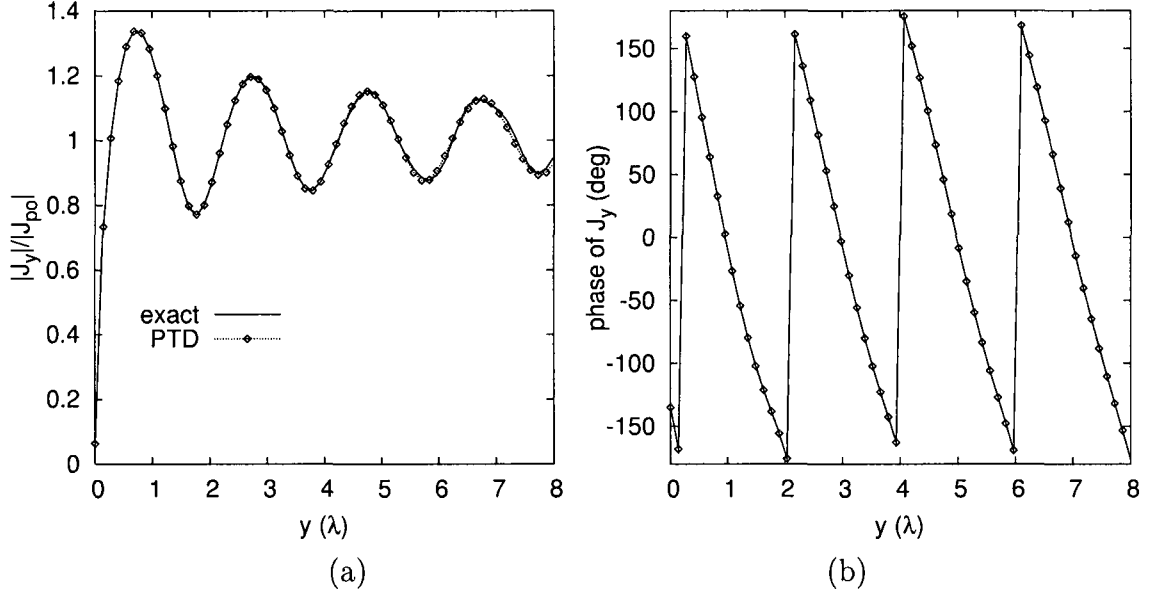
Figure 2.5: (a) Magnitude and (b) Phase of the total current density perpendicular to edge $\hat{e}_1$. The current density is calculated along the path shown in Fig. 2.3(a) with $d_c = 2\lambda$ for a $\hat{\theta}_i$ polarized plane wave incident from the direction $(\theta_i, \phi_i) = (30°, 270°)$.

current density on a plane angular sector of $\alpha_d = 90°$ evaluated at $\gamma = 0.5°$ is shown in Fig. 2.4. The problem geometry and the path along which the current is calculated is depicted in Fig. 2.3(a). The real part of J_r as a function of the number of terms used in (2.53) is shown in Fig. 2.4(a). It is observed that number of terms necessary for convergence increases with the radial distance. In Fig. 2.4(b), ΔJ_r denotes the contribution from each term in (2.53) separately. The corresponding value of μ_n for each term is also shown in Fig. 2.4(b). It is observed that the contribution due to the terms with a large value of μ_n is very small. Most of the contribution is due to the terms for which μ is close to 0. Thus, only the first few terms per each ν-μ curve make a significant contribution to the current density at this distance. This

shows that the series must be evaluated starting from the smallest value of ν to obtain better convergence. In order to further improve the convergence, acceleration techniques such as Euler transformation or Shanks transformation can be used. In [5] and [6] these transformation methods are used to calculate the scattered field from an elliptic cone in the far zone for nose-on incidence. In order to investigate the behavior of vertex-diffracted currents, it is sufficient to calculate the exact current only in the close vicinity of the vertex. Towards this goal, we use directly (2.53) to calculate the exact current density.

In [1] and [22], the solution of the problem is formulated using the same form of eigenfunctions (see Table 2.1). However, the eigenvalue pairs and the coefficients for the eigenfunctions are obtained in a different manner. In order to obtain the eigenvalue pairs; the determinant of the matrix eigenvalue problem, which must be zero, is identified in the form of an infinite continued fraction. Such an expression can be written for each matrix eigenvalue problem (2.30), (2.35), (2.36) and (2.42). The eigenvalue pairs are calculated by solving the corresponding determinant equations simultaneously. Finally, the coefficients for the eigenfunctions are obtained by using the recurrence relations similar to (2.26) and (2.31). Even though this approach is computationally less intensive, it results in incorrect values for large values of ν. Thus, this method can be used to calculate the current density only around the immediate vicinity of the vertex. It was observed that, the accuracy of the current degrades after $r \simeq 1.2\lambda$ when this approach was used to calculate the eigenvalue pairs and the coefficients of the eigenfunctions.

Fig. 2.5 shows the current $\hat{y}$ component of the current density on a $\alpha_d = 90^o$ plane angular sector illuminated by a $\hat{\theta}_i$ polarized plane wave incident from the direction $(\theta_i, \phi_i) = (30°, 270°)$. The problem geometry and the path along which the current density is plotted are shown in Fig. 2.3(b). The two edges of the angular sector are denoted by $\hat{e}_1$ and $\hat{e}_2$. The current density is calculated along the path that is

perpendicular to $\hat{e}_1$. The distance to the vertex, d_c, was chosen to be 2λ. In Fig. 2.5 "PTD" denotes the current density obtained using the Physical Theory of Diffraction. For the given direction of incidence in this example, when the observation point is far from the vertex, the current density should be very similar to the current density induced on a half plane that conforms to the angular sector at edge $\hat{e}_1$. The PTD current is obtained from Sommerfeld's exact solution [24] as the sum of PO and fringe wave (FW) currents. For the given direction of incidence and polarization, the vertex diffracted current is negligible along the perpendicular cut considered in this example. Thus, the current density obtained using the PTD is expected to be accurate and can be used to test the accuracy of the eigenfunction solution described in this chapter. It is observed that both the phase and the amplitude of the exact current density calculated using (2.53) agree very well with the PTD current. The $\hat{x}$ component of the current density for $\hat{\theta}_i$ polarized incident field was found to be zero as expected. Along the perpendicular cut $d_c = 2\lambda$, the maximum radial distance to the vertex is $r \simeq 8.2\lambda$. The parameters used in evaluating (2.53) and the eigenfunction expansions in this example are $N_c = 2500$ and $N_f = 71$. This guarantees convergence at the maximum radial distance.

In order to investigate the behavior of the current density near the vertex, we consider the current density induced on a plane angular sector of $\alpha_d = 90°$. Fig. 2.6 illustrates the $\hat{r}$ and $\hat{\phi}$ components of the current density as a function of γ at $r = 0.5\lambda$. The problem geometry is depicted in Fig. 2.3(a). The angular sector is illuminated by a $\hat{\theta}_i$ polarized plane wave from various directions. The PTD current is discontinuous at the shadow boundaries of the first order diffracted currents from the two edges. For $(\theta_i, \phi_i) = (45°, 225°)$, these shadow boundaries occur at $\gamma = 60°$ and $\gamma = 30°$ for edge $\hat{e}_1$ and $\hat{e}_2$ respectively. For $(\theta_i, \phi_i) = (80°, 225°)$, the PTD current exhibits similar discontinuities at $\gamma = 45.86°$ and $\gamma = 44.13°$. Fig. 2.7 shows the current density at $r = 5\lambda$ for the same scattering configuration. It is observed that the amount of
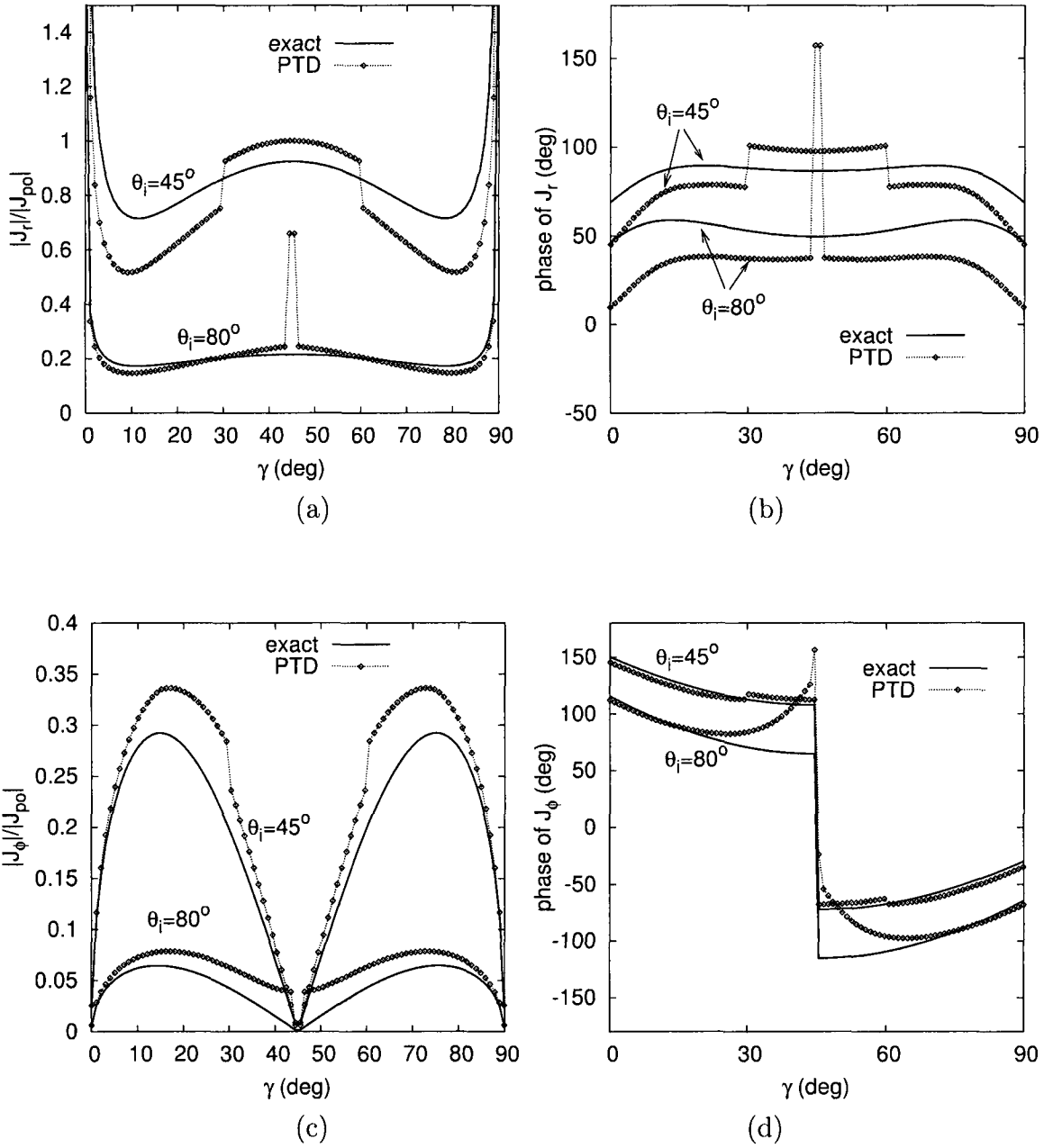
Figure 2.6: (a), (b) $\hat{r}$ and (c), (d) $\hat{\phi}$ components of the total current density on a 90° angular sector at $r = 0.5\lambda$ for a $\hat{\theta}_i$ polarized plane wave incident from the direction $(\theta_i, \phi_i) = (45°, 225°)$ and $(\theta_i, \phi_i) = (80°, 225°)$.
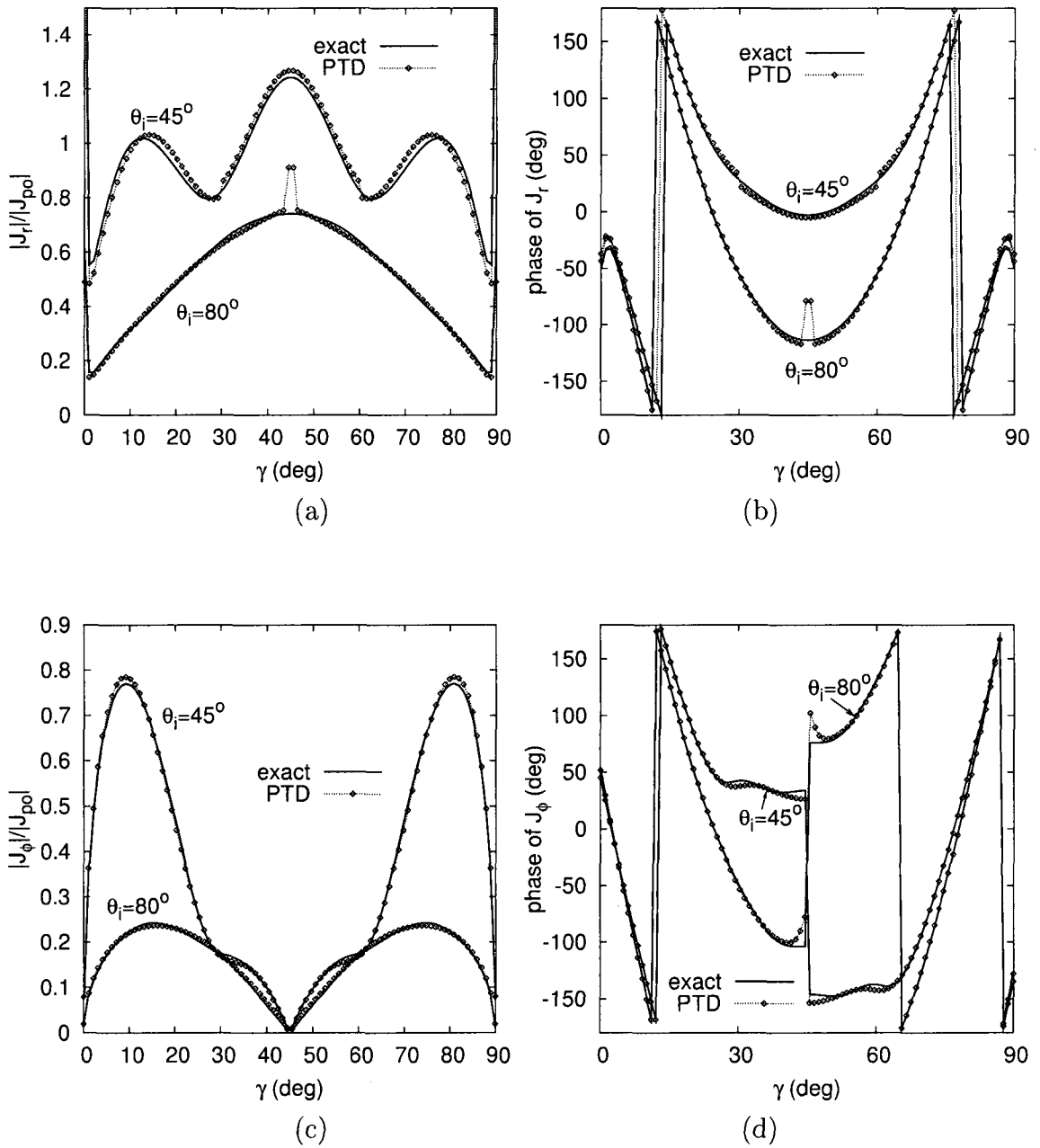
Figure 2.7: (a), (b) $\hat{r}$ and (c), (d) $\hat{\phi}$ components of the total current density on a 90° angular sector at $r = 5\lambda$ for a $\hat{\theta}_i$ polarized plane wave incident from the direction $(\theta_i, \phi_i) = (45°, 225°)$ and $(\theta_i, \phi_i) = (80°, 225°)$.

discontinuity at the shadow boundaries decreases when the observation point moves away from the vertex. Furthermore, the PTD current agrees better with the exact current as the observation point moves away from the vertex. This is particularly evident in the ϕ component of the current density. Far from the vertex, the vertex-diffracted waves are not significant. Consequently, the current density predicted by the PTD is accurate when no higher-order edge to edge interactions are present.

In the next example, we consider the case where double-diffracted currents are significant. Fig. 2.8 shows the current density induced on a plane angular sector of $\alpha_d = 60°$ for a $\hat{\theta}_i$ polarized plane wave incident from the direction $(\theta_i, \phi_i) = (30°, 240°)$. The current density is plotted at $r = 0.8\lambda$. The discontinuities in the PTD current in this case are associated with the double-diffracted currents. The shadow boundaries for these currents occur at $\gamma = 1.2°$ and $\gamma = 50.7°$. Similar to the previous example, the amount of discontinuity at the shadow boundaries decreases as the radial distance to the vertex is increased. Fig. 2.9 shows the current density at $r = 8\lambda$ for the same scattering configuration.

2.5 Conclusion

In this chapter, the eigenfunction expression for the current density induced on a perfectly-conducting, infinitely-thin semi-infinite plane angular sector illuminated by a plane wave was derived. Since the vertex-diffracted currents will be formulated using this expression in the following chapter, the accuracy of the eigenfunction solution is of primary importance.

First, the scalar wave equation was separated into two coupled Lamé equations and the spherical Bessel equation. Then, the solution of the Lamé equations were expressed in terms of eigenfunction expansions based on the boundary conditions. By substituting the eigenfunction expansions in the differential equations, matrix
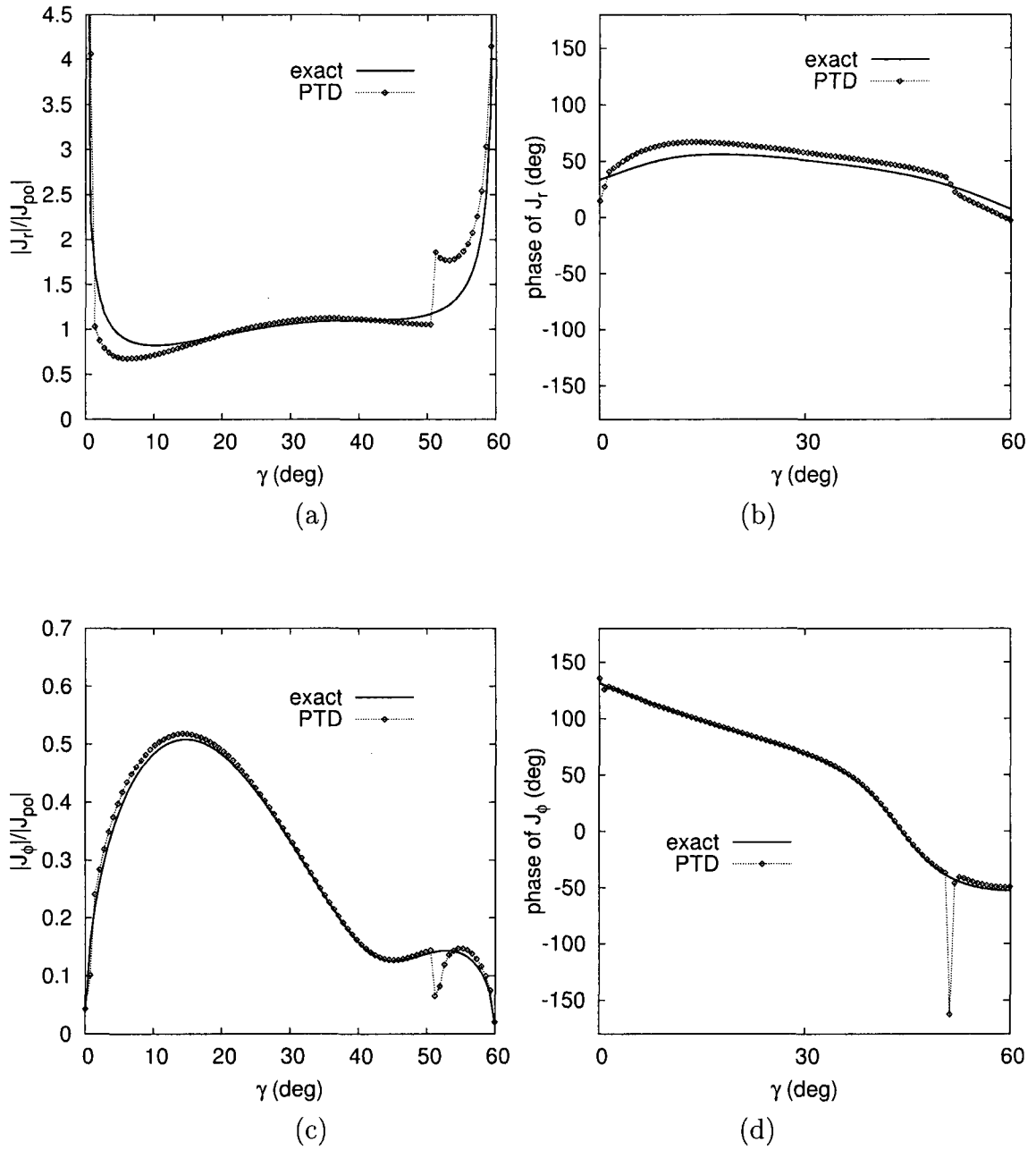
Figure 2.8: (a), (b) $\hat{r}$ and (c), (d) $\hat{\phi}$ components of the total current density on a 60° angular sector at $r = 0.8\lambda$ for a $\hat{\theta}_i$ polarized plane wave incident from the direction $(\theta_i, \phi_i) = (30°, 240°)$.
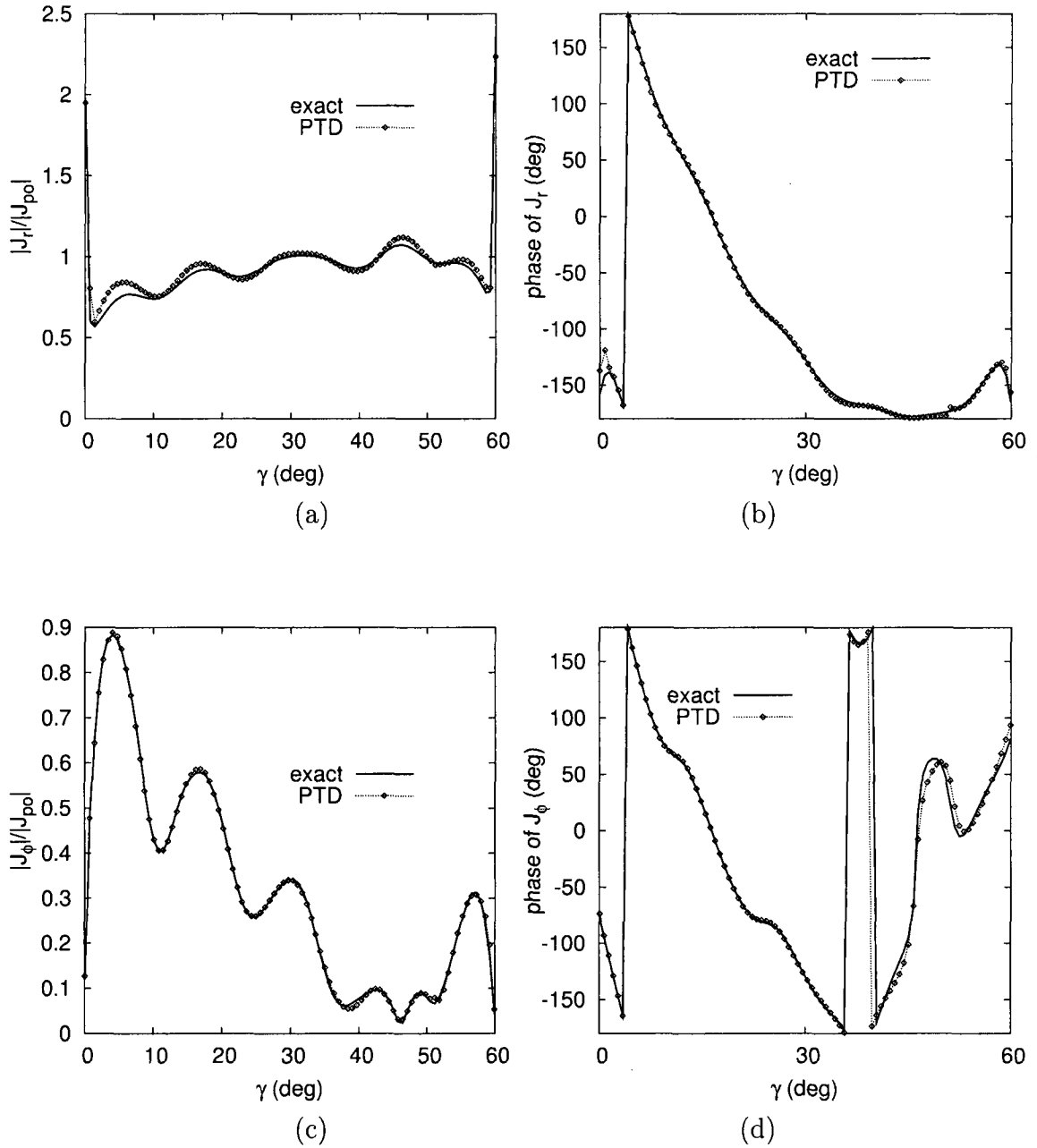
Figure 2.9: (a), (b) $\hat{r}$ and (c), (d) $\hat{\phi}$ components of the total current density on a 60° angular sector at $r = 8\lambda$ for a $\hat{\theta}_i$ polarized plane wave incident from the direction $(\theta_i, \phi_i) = (30°, 240°)$.

eigenvalue problems were obtained for each expansion. The eigenvalue pairs and the expansion coefficients were then calculated by simultaneously solving the matrix eigenvalue problems. In evaluating the expansion coefficient and the eigenvalue pairs, the matrix eigenvalue equations were solved directly using a QR algorithm. It was shown that this approach provides accurate results even at distances far from the vertex.

The exact current density was compared with the PTD current density for various scattering configurations. The PTD current is in fact exact when it is used to calculate the current density on a half plane. The plane angular sector can simply be interpreted as the intersection of two half planes. However, in this case the half plane conforming to one edge of the angular sector is truncated at the other edge. Thus, the current due to these two truncated half planes are not the same as the current induced on the half plane that is not truncated. Furthermore, the tip of the angular sector acts as a new diffraction center and affects the current density even more. It was shown that all these effects become negligible as the observation point moves away from the vertex. Far from the vertex, the eigenfunction solution and the PTD currents agree well. On the other hand, the two results do not agree around the shadow boundary lines when the observation point is close the vertex. This difference between the exact and the PTD currents is interpreted as the vertex-diffracted current and will be investigated in detail in the following chapter.

Chapter 3

Vertex-Diffracted Edge Waves

3.1   Introduction

In this chapter, the behavior of the vertex-diffracted currents is investigated in detail. The vertex-diffracted currents are defined as the difference between the exact and PTD currents. Up to second order edge diffracted currents are included in the PTD solution. The formulation of the second-order edge to edge interactions is summarized in Section 3.2. Numerical diffraction coefficients for the vertex-diffracted currents are derived in Section 3.3. Finally, the effect of the corner diffracted currents on the RCS pattern is illustrated for various scattering configurations. The scattering configurations used in the numerical examples are chosen to be the same as the ones used in the previous developments ([11], [17], [22]) to be able to assess the performance of the new derivation. This chapter has been reported in [43].

3.2 Current density on a plane angular sector

Consider an infinitely-thin, perfectly-conducting plane angular sector illuminated by a plane wave as shown in Fig. 3.1. The current density on the plane angular sector can be expressed as the sum of the physical optics (PO) current, the fringe wave (FW) current and the vertex-diffracted current. The vertex diffracted current is then defined as

$$\bar{J}^c = \bar{J}^e - (\bar{J}^{PO} + \bar{J}_1^{fw} + \bar{J}_2^{fw} + \bar{J}_{12}^{dd} + \bar{J}_{21}^{dd}) \tag{3.1}$$

where $\bar{J}^e$ is the exact current and $\bar{J}^{PO}$ is the well-known PO current. $\bar{J}_1^{fw}$ and $\bar{J}_2^{fw}$ are the fringe-wave contributions due to the two edges of the angular sector. $\bar{J}_{12}^{dd}$ and $\bar{J}_{21}^{dd}$ denote the edge-to-edge double-diffracted current contributions. An edge-fixed coordinate system is defined at each diffraction point O as depicted in Fig. 3.1. $\hat{n}$ is the normal and $\hat{x}$ is the tangent to the surface of the half plane. The edge tangent $\hat{t}$ must be defined such that $\hat{x} \times \hat{n} = \hat{t}$. With respect to the edge-fixed coordinate system, the incident plane wave is given by

$$\bar{H}(s) = [\hat{\phi}' H_{\phi'} + \hat{\beta}' H_{\beta'}] e^{-jk\hat{s}' \cdot \hat{s}s}$$

where $H_{\phi'}$ and $H_{\beta'}$ denote the $\hat{\phi}'$ and the $\hat{\beta}'$ components with the phase referenced to the tip of the angular sector. The edge diffracted fringe wave current on a half plane is obtained by subtracting the PO current from the total current [24]. The parallel and the perpendicular components of the fringe wave current can be expressed as

$$J_x^{fw}(s) = -\frac{2e^{-j\pi/4}}{\sqrt{\pi\sigma}} e^{-jks} H_{\beta'} \sin\beta' F(\sigma) \tag{3.2}$$

$$J_t^{fw}(s) = \frac{2e^{-j\pi/4}}{\sqrt{\pi\sigma}} e^{-jks} \left\{ -H_{\beta'} \cos\beta' F(\sigma) \right.$$

$$\left. + \left[H_{\phi'} \frac{\sin\phi'}{2} - H_{\beta'} \cos\beta' \cos^2\frac{\phi'}{2} \right] [2 - 2F(\sigma)] \right\} \tag{3.3}$$
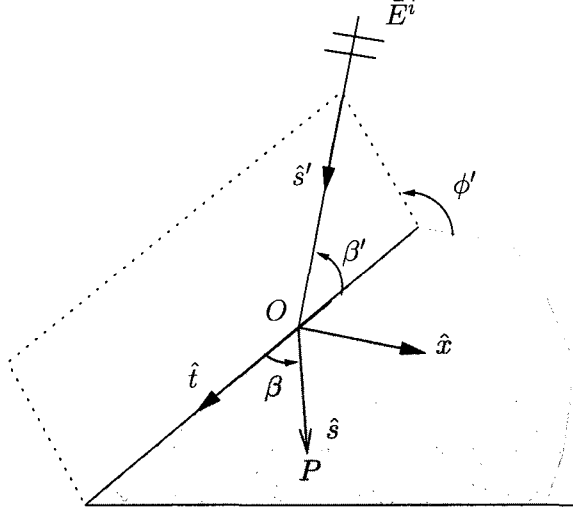
Figure 3.1: Plane angular sector and the edge fixed coordinate system.

where

$$\sigma = ks(1 - \hat{s} \cdot \hat{s}'),$$

$$F(x) = 2j\sqrt{x}e^{jx} \int_{\sqrt{x}}^{\infty} e^{-j\tau^2} d\tau.$$

The direction of propagation for the FW surface current is defined by the intersection of the Keller cone and the plate surface $(\beta = \beta')$. In order to obtain an expression for the double-diffracted currents, (3.2) and (3.3) are used at the second-order diffraction point. Consider the diffraction path depicted in Fig. 3.2. The diffracted field at O_1 is re-diffracted by the other edge at O_2. Assuming plane wave incidence, the fringe-wave current due to the diffraction at the second order diffraction point, O_2, can be expressed as

$$\bar{J}^{fw}(s_2) = \frac{-2e^{-j\pi/4}}{\sqrt{\pi\sigma}}e^{-jks_2}\Big\{ \hat{x}_2(\bar{H}_{12}^i \cdot \hat{t}_2)F(\sigma)$$

$$+\hat{t}_2(\bar{H}_{12}^i \cdot \hat{x}_2)[2 - F(\sigma)]\Big\} \tag{3.4}$$

in which $\bar{H}_{12}^i$ is the magnetic field diffracted from the first-order diffraction point, O_1. Eq. (3.4) follows directly from (3.2) and (3.3) by substituting $\phi' = 0$, $H_{\beta'}\sin\beta' =$

$\bar{H}^i \cdot \hat{t}_2$ and $H_{\beta'} \cos \beta' = \bar{H}^i \cdot \hat{x}_2$. Using the PO approximation, the magnetic field incident on the second-order diffraction point $(\bar{H}^i_{12})$ can be expressed as

$$2\bar{H}^i_{12}(O_2) = -\hat{x}_2(J_1^{fw}(O_2) \cdot \hat{t}_2) + \hat{t}_2(J_1^{fw}(O_2) \cdot \hat{x}_2) \tag{3.5}$$

where J_1^{fw} is the FW current diffracted by the first edge at O_1. Using (3.5) in (3.4), the double-diffracted FW current at point P can be expressed in terms of the first-order FW currents as

$$\bar{J}^{dd}_{12}(s_2) = \frac{-e^{-j\pi/4}}{\sqrt{\pi\sigma}} e^{-jks_2} \left\{ \hat{x}_2(\bar{J}_1^{fw}(O_2) \cdot \hat{x}_2)F(\sigma) \right.$$
$$\left. -\hat{t}_2(\bar{J}_1^{fw}(O_2) \cdot \hat{t}_2)[2 - F(\sigma)] \right\}. \tag{3.6}$$

It is noted that the first-order diffracted current (J_1^{fw}) introduces a normal component to the edge along edge 2. Using (3.6), it can be shown that this component is canceled by the introduction of the second-order diffracted current. The normal component of the first-order diffracted current at O_1 is canceled by the normal component of the PO current. Therefore, the edge condition [33] on the current density that is normal to the edges of the angular sector is satisfied by the introduction of double-diffracted currents.

3.3 Vertex-diffracted Currents

In this section, we investigate the behavior of the vertex-diffracted currents near the corner of the plane angular sector. We consider the plane angular sector shown in Fig. 3.3. The vertex-diffracted current is obtained by subtracting the known edge-diffracted current contributions from the total current as suggested by (3.1). Regardless of the tip angle, the plane angular sector is centered in the first quadrant of the x-y plane so that $\hat{e}_1 \cdot \hat{x} = \hat{e}_2 \cdot \hat{y}$. The total current, $\bar{J}^e$, is the exact solution obtained using the eigenfunction solution described in Chapter 2. The FW contributions are calculated using (3.2) and (3.3). In order to demonstrate the derivation of

37
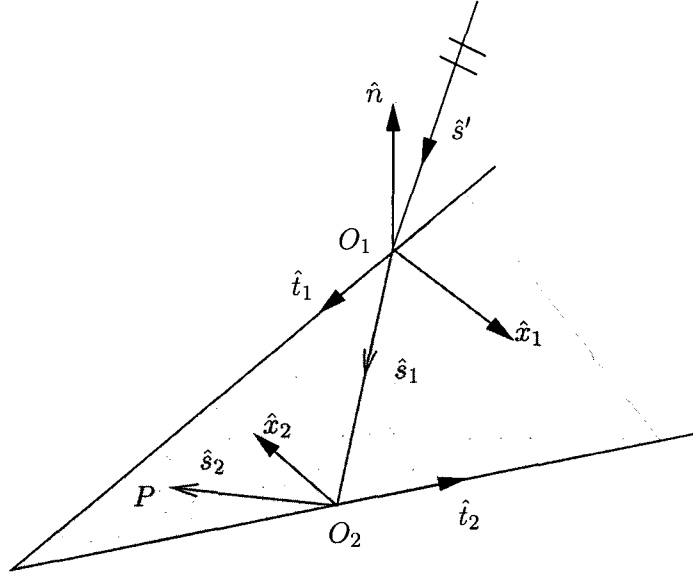
Figure 3.2: Ray path for double diffracted current.

the vertex-diffracted currents, we consider a plane angular sector of $\alpha_d = 60°$ illuminated by a $\hat{\theta}_i$ polarized plane wave incident from the direction $(\theta_i, \phi_i) = (80°, 225°)$.

The vertex-diffracted current is calculated along various radial cuts defined by γ, the angular position with respect to edge $\hat{e}_1$. The amplitude and the phase of the $\hat{r}$ component of the corner current is shown in Fig. 3.4. It is observed that, the phase behavior is the same as the phase behavior of a wave traveling away from the corner. Furthermore, the amplitude behavior along various radial cuts shows that the functional dependence on the distance from the corner is also a function of the angle γ. The behavior of the J_ϕ is very similar to that of J_r. Based on this observation, the vertex-diffracted current is formulated as

$$J^v = K(\gamma)(kr)^{-\alpha(\gamma)}e^{-jkP(\gamma)r} \tag{3.7}$$

where J^v denotes the $\hat{r}$ or the $\hat{\phi}$ component of the vertex-diffracted current density. $K(\gamma)$, $\alpha(\gamma)$ and $P(\gamma)$ are the unknown functions to be obtained numerically. The form of the corner diffracted currents given by (3.7) can also be deduced by using

38
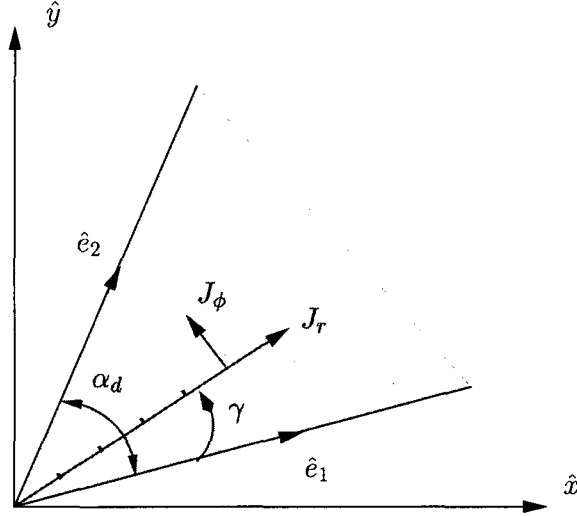
Figure 3.3: Plane angular sector on the x-y plane and the radial cuts. The angular sector is centered in the first quadrant of the x-y plane so that $\hat{e}_1 \cdot \hat{x} = \hat{e}_2 \cdot \hat{y}$.

the corner condition [25]. It is noted that for the results illustrated in Fig. 3.4, the sampling locations along the given radial cuts correspond to forward scattering directions with respect to the incidence direction. Thus, there are no multiple edge diffractions involved in calculating the corner currents ($\bar{J}_{12}^{dd} = 0$, $\bar{J}_{21}^{dd} = 0$). Consequently, the difference current $\bar{J}^c$ is dominated by the vertex-diffracted currents. When higher-order edge-to-edge diffractions are present, it is important to be able to extract the vertex-diffracted current from the total current in an accurate manner. In many cases, the corner current as defined in (3.1) may be dominated by the higher-order edge-diffracted currents. To demonstrate this, we consider a 90° angular sector illuminated from the direction $(\theta_i, \phi_i) = (80°, 160°)$. The vertex-diffracted current calculated along the radial cut $\gamma = 10°$ is shown in Fig. 3.5. The current distribution labeled "FW-1" represents the vertex current obtained without subtracting the double-diffracted edge currents(i. e. $\bar{J}_{21}^{dd} = 0$). "FW-2" denotes the actual vertex current calculated using (3.1). The double-diffracted current, $\bar{J}_{21}^{dd}$ is also shown for comparisons with the two types of difference currents. It is observed that when the

39
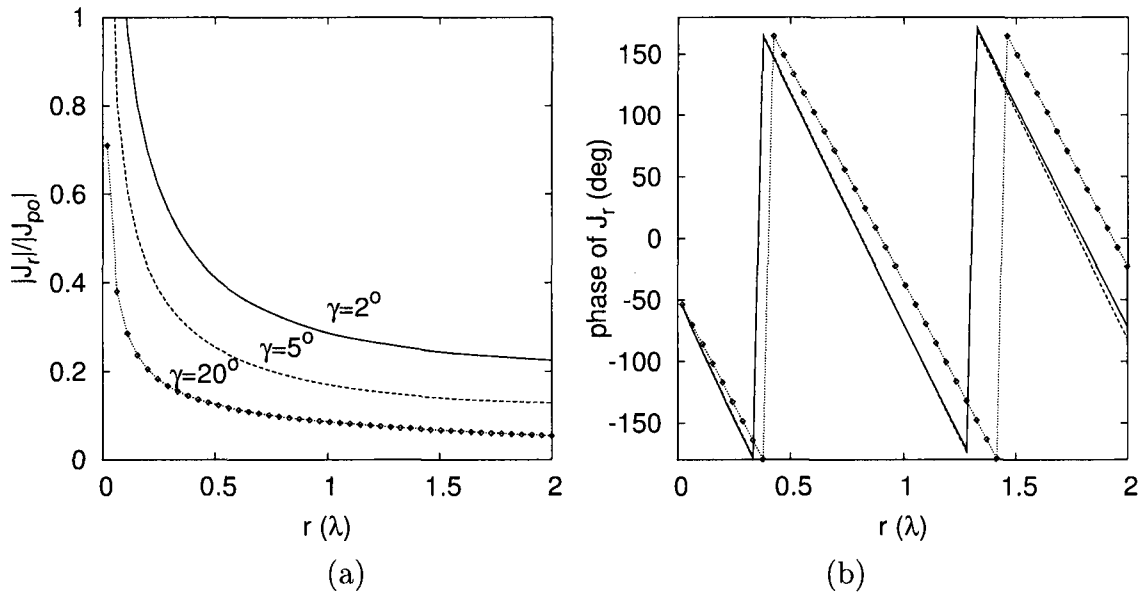
Figure 3.4: (a) Magnitude and (b) Phase of J_r^c on a 60° angular sector along various radial cuts for a $\hat{\theta}_i$ polarized plane wave incident from the direction $(\theta_i, \phi_i) = (80°, 225°)$.

double-diffracted currents are ignored, the behavior of the difference current agrees with the form assumed by (3.7). However, by comparing the phase behavior of this difference current with that of double-diffracted current alone, we deduce that the difference current is dominated by the double-diffracted current. It is noted that the phase behaviors are very similar in the two cases. However, as depicted in Fig. 3.5, the magnitude of the vertex-diffracted current is in fact much smaller than the one that is obtained without incorporating the double-diffracted currents. This would definitely result in erroneous far fields. Therefore, incorporation of the double-diffracted currents is quite critical in calculating the vertex-diffracted currents.

In order to obtain the unknowns $K(\gamma)$, $\alpha(\gamma)$ and $P(\gamma)$ for a given direction of incidence and polarization, the vertex-diffracted current obtained using (3.1) is uniformly
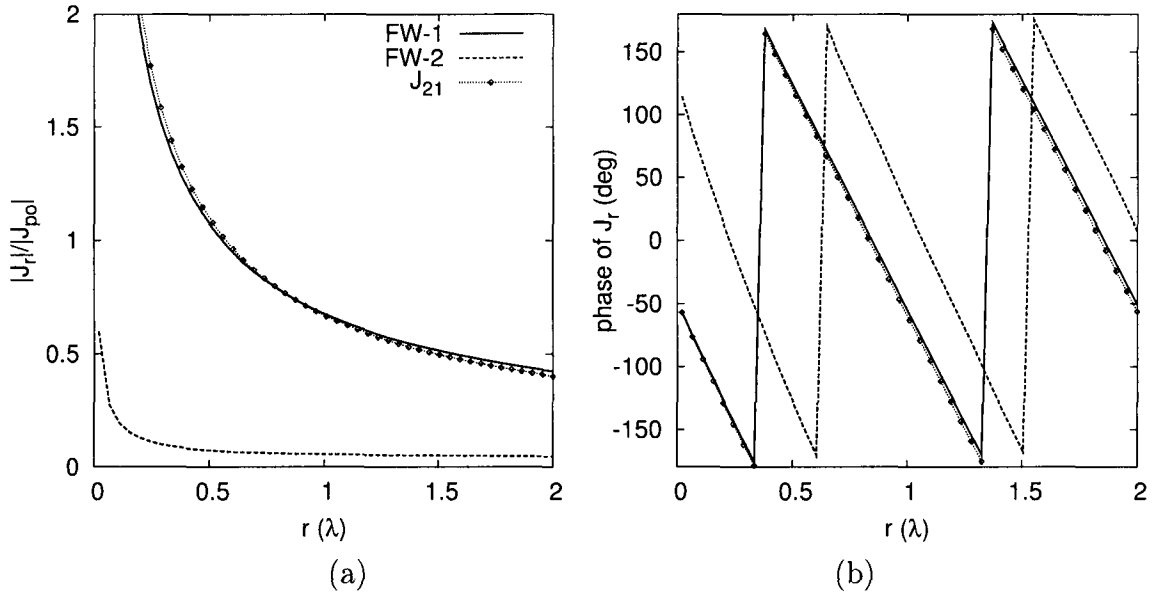
Figure 3.5: (a) Magnitude and (b) Phase of J_r^c on a 90° angular sector along the radial cut $\gamma = 10°$ for a $\hat{\theta}_i$ polarized plane wave incident from the direction $(\theta_i, \phi_i) = (80°, 160°)$.

sampled along the desired radial cut γ_0. It follows from (3.7) that

$$\ln(|J^c(\gamma_0, r_n)|) = -\alpha(\gamma_0) \ln(kr_n) + \ln(|K(\gamma_0)|) \tag{3.8}$$

$$\angle J^c(\gamma_0, r_n) = -P(\gamma_0)kr_n + \angle K(\gamma_0). \tag{3.9}$$

The radial distance to the vertex, r_n, denotes the nth sampling point along the radial cut defined by $\gamma = \gamma_0$ and $r_{min} \leq r_n \leq r_{max}$. The unknowns can be obtained by solving (3.8) and (3.9) separately using linear least-squares fitting [44]. The upper limit of the radial cut r_{max} should be chosen sufficiently large that the unknown coefficients can be obtained accurately using the least squares fit. However, it must be pointed out that the infinite series of eigenfunction expansions used to calculate the exact current, $\bar{J}^e$, converges more slowly as the observation point moves away from the tip of the angular sector. In this dissertation, we use $r_{max} = 1\lambda$ with 15 uniformly spaced sampling points (N=15). In our formulation of the eigenfunction expansions,

41

this requires the evaluation of the first 115 terms in the infinite series of the current expression and 15 terms for each eigenfunction expansion ($N_c = 115$, $N_f = 15$). The unknown coefficients over the entire surface for a given incidence direction can accurately be calculated using these variables. The singularity exponent, $\alpha(\gamma_0)$, and the magnitude of the diffraction coefficient $K(\gamma_0)$ can be expressed as

$$\alpha(\gamma_0) = -\frac{\sum_{n=1}^{N} y_n \sum_{n=1}^{N} x_n - N \sum_{n=1}^{N} x_n y_n}{\left(\sum_{n=1}^{N} x_n\right)^2 - N \sum_{n=1}^{N} x_n^2} \tag{3.10}$$

$$\ln |K(\gamma_0)| = \frac{1}{N} \left[\sum_{n=1}^{N} y_n + \alpha(\gamma_0) \sum_{n=1}^{N} x_n\right] \tag{3.11}$$

where

$$y_n = \ln(|J^c(\gamma_0, r_n)|),$$

$$x_n = \ln(kr_n) \qquad n = 1, ..., N.$$

The phase factor $P(\gamma_0)$ and the phase of $K(\gamma_0)$ can similarly be obtained by using (3.10) and (3.11) respectively with $y_n = \angle J^c(\gamma_0, r_n)$ and $x_n = kr_n$. The difference current J_r^c and the least-square fit (LSF) approximation that is obtained using (3.7) for two different cases are shown in Fig. 3.6. In Fig. 3.6(a) the direction of incidence is $(\theta_i, \phi_i) = (60°, 225°)$. This corresponds to forward scattering since there are no double-diffracted currents. On the other hand in Fig. 3.6(b), the direction of incidence is chosen to be $(\theta_i, \phi_i) = (30°, 45°)$, for which double-diffracted currents are rather significant. The LSF current density given by (3.7) agrees well with the difference current except around the immediate vicinity of the vertex in both cases.

3.4 Numerical Examples

We first consider the current density induced on a plane angular sector of 30° for $\hat{\theta}_i$ polarized incidence from the direction $(\theta_i, \phi_i) = (60°, 45°)$. The current density
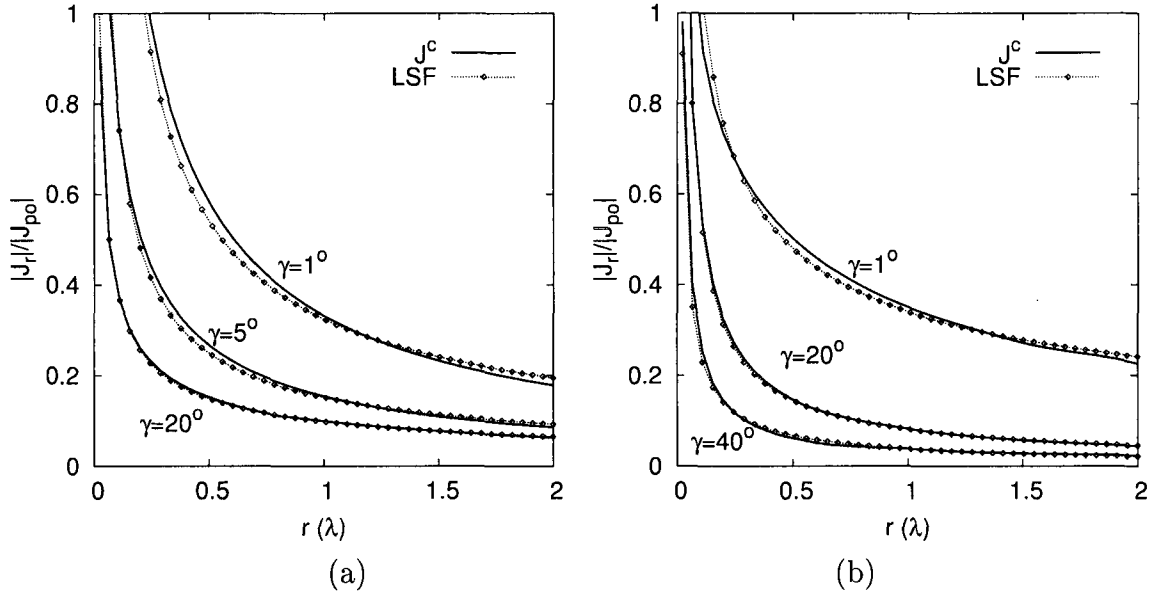
Figure 3.6: Magnitude of J_r^c and the least-squares approximation on a 90° angular sector along various radial cuts for $\hat{\theta}_i$ polarized plane wave incidence. (a) $(\theta_i, \phi_i) = (60°, 225°)$ and (b) $(\theta_i, \phi_i) = (30°, 45°)$.

obtained using the vertex-diffracted currents is compared with the exact solution in Fig. 3.7. The current density is calculated at $r = 0.5\lambda$ for $0° < \gamma < 30°$, where r is the radial distance from the tip and γ is defined as shown in Fig. 3.3. "FW-1" denotes the current density obtained using only the first-order edge-diffracted currents. The solution labeled "FW-2" represents the current density obtained by superimposing the double diffraction contributions to the first order FW currents. "FW+corner" is the current density obtained using both the first- and second-order edge-diffracted currents and the vertex-diffracted currents. It is noted that there are no discontinuities in the FW solutions since there are no diffraction shadow boundaries on the surface of the angular sector for the given direction of incidence. For the $\hat{\phi}$ component of the surface current density, inclusion of the second-order edge-diffracted currents considerably improves the accuracy of the solution. Note from Fig. 3.7(b)

that the first-order only solution tends to be singular at the edges. This is a non-physical behavior. On the other hand, when double-diffracted currents are included, J_ϕ tends to be zero near the edges. In general, the double-diffracted currents provide a significant contribution to the $\hat{\phi}$ component of the total current near the edges. However, the resulting current density is still not accurate. Inclusion of the double-diffracted currents does not seem to have a substantial improvement on J_r as shown in Fig. 3.7(a). The high-frequency current obtained using the vertex-diffracted currents agrees very well with the exact solution for both the $\hat{r}$ and $\hat{\phi}$ components. It is also observed that J_r and J_ϕ satisfy the edge condition.
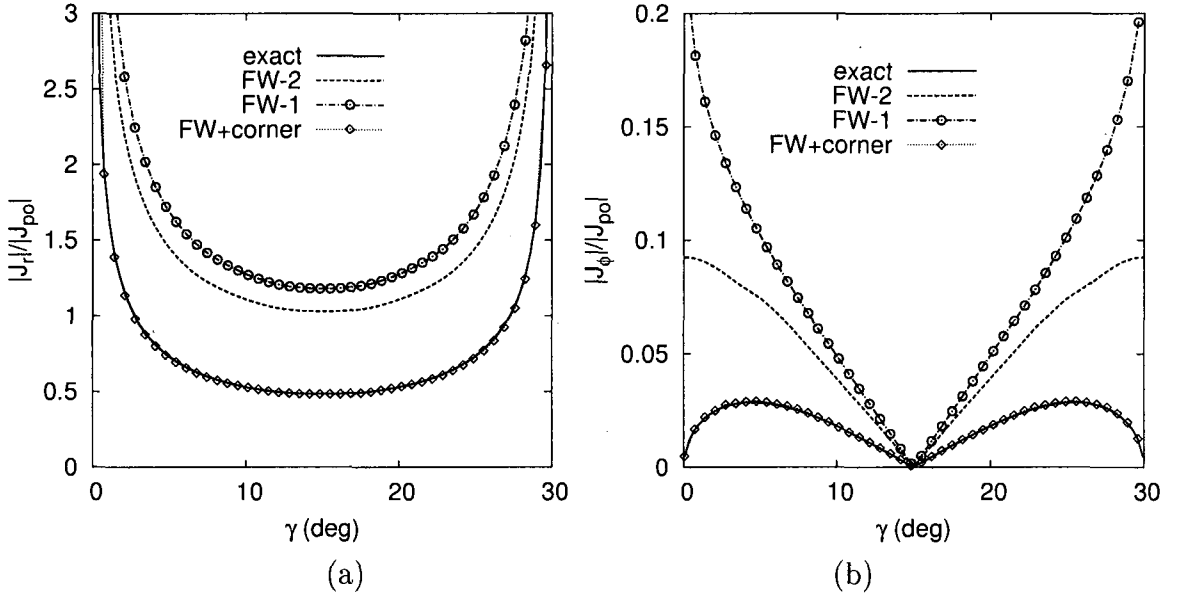
Figure 3.7: (a) $\hat{r}$ and (b) $\hat{\phi}$ components of the total current density on a 30° angular sector at $r = 0.5\lambda$ for a $\hat{\theta}_i$ polarized plane wave incident from the direction $(\theta_i, \phi_i) = (60°, 45°)$.

Next we consider the current density on a 90° plane angular sector for forward scattering directions. For $(\theta_i, \phi_i) = (45°, 225°)$, there are two shadow boundaries for the first-order edge-diffracted currents. These shadow boundaries appear at $\gamma = 60°$ for edge 1 and at $\gamma = 30°$ for edge 2. When the direction of incidence is $(\theta_i, \phi_i) =$

$(80°, 225°)$ the shadow boundary lines for edges 1 and 2 move to $\gamma = 45.86°$ and $\gamma = 44.14°$ respectively as shown in Fig. 3.8. The distance at which the current density is plotted in this example is $r = 0.5\lambda$. This is rather close to the tip of the angular sector. Thus the amount of discontinuity at the shadow boundaries is quite large. As the distance to the vertex increases, the amount of discontinuity decreases. In any case, the discontinuity is removed by the inclusion of the vertex diffracted currents. The resulting high-frequency current agrees very well with the exact solution.
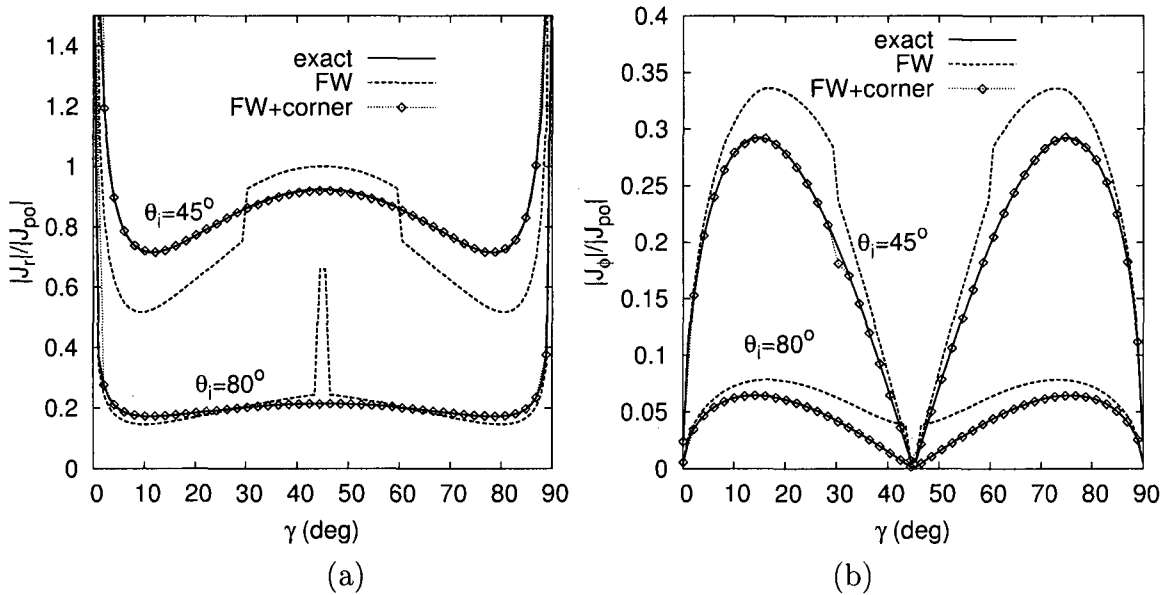
Figure 3.8: (a) $\hat{r}$ and (b) $\hat{\phi}$ components of the total current density on a 90° angular sector at $r = 0.5\lambda$ for a $\hat{\theta}_i$ polarized plane wave incident from the direction $(\theta_i, \phi_i) = (45°, 225°)$ and $(\theta_i, \phi_i) = (80°, 225°)$.

Fig. 3.9 shows the $\hat{r}$ and ϕ components of the current density on the plane angular sector of $\alpha_d = 90°$ as a function of the radial distance from the tip along the radial cut $\gamma = 1°$. Since the vertex-diffracted currents are strongly guided around the edges (Fig. 3.7), it is particularly important to predict the vertex-diffracted currents accurately near the edges. The angular sector is illuminated by a $\hat{\theta}_i$ polarized plane
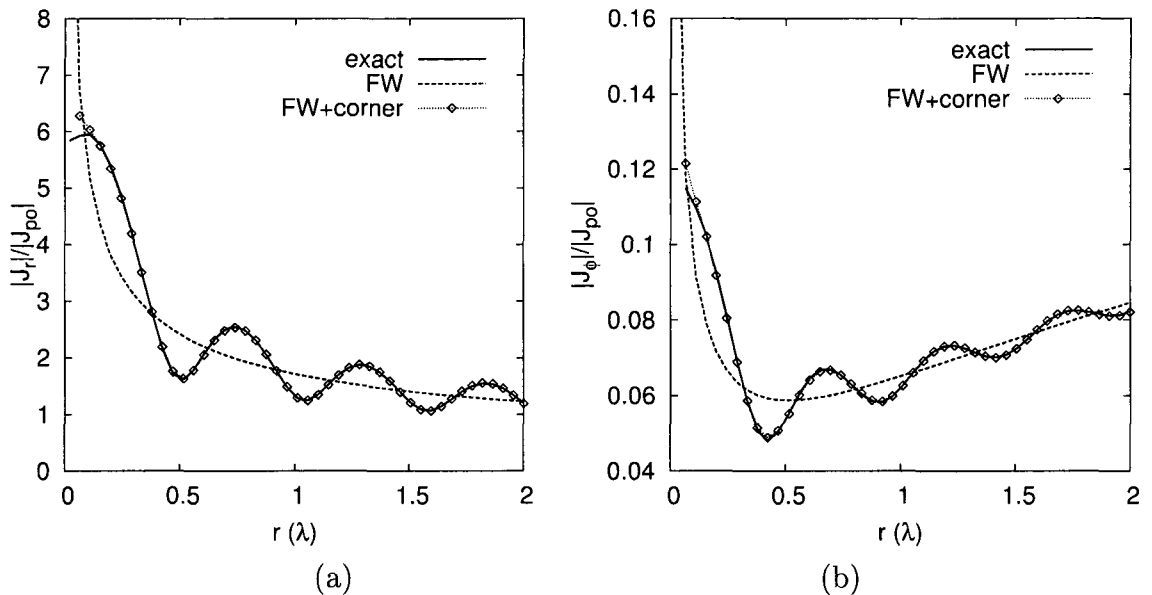
Figure 3.9: (a) $\hat{r}$ and (b) $\hat{\phi}$ components of the total current density on a 90° angular sector along the radial cut $\gamma = 1°$ for a $\hat{\theta}_i$ polarized plane wave incident from the direction $(\theta_i, \phi_i) = (60°, 345°)$.

wave incident from the direction $(\theta_i, \phi_i) = (60°, 345°)$. It is observed that the total high frequency current agrees well with the exact solution except at distances very close to the tip. Similar behavior was observed in general for any given direction of incidence. This behavior is expected since the vertex-diffracted currents are not expected to be ray-optical in the immediate vicinity of the vertex. We observed that this does not cause any substantial error in the RCS pattern.

In Fig. 3.10(a), we present the numerical diffraction coefficient K as a function of γ for various directions of incidence for a 90° angular sector. It is observed that the diffraction coefficient becomes singular at the two edges of the plane angular sector. The vertex-diffracted waves are strongly guided by the edges of the angular sector as suggested by the edge condition [33]. As demonstrated in the earlier numerical example, the vertex-diffracted currents correct the discontinuity of the edge-diffracted currents at the shadow boundary lines. This is the part of the vertex-diffracted

currents that accounts for the truncation of the FW currents. As a consequence, the diffraction coefficients are discontinuous at the shadow boundaries. It is noted that for $(\theta_i, \phi_i) = (45°, 45°)$ (continuous line) the discontinuities at $\gamma = 30°$ and $\gamma = 60°$ correspond to shadow boundaries for the double diffracted rays. Similarly, the diffraction coefficient is discontinuous at $\gamma = 56.77°$ and $\gamma = 77.05°$ for $(\theta_i, \phi_i) = (60°, 255°)$. Fig. 3.10(b) shows the phase factor P as a function of γ. It is observed that the phase factor is close to 1 for the entire angular range except around the transition regions. This verifies that the vertex-diffracted fields behave like a spherical wave traveling away from the vertex.
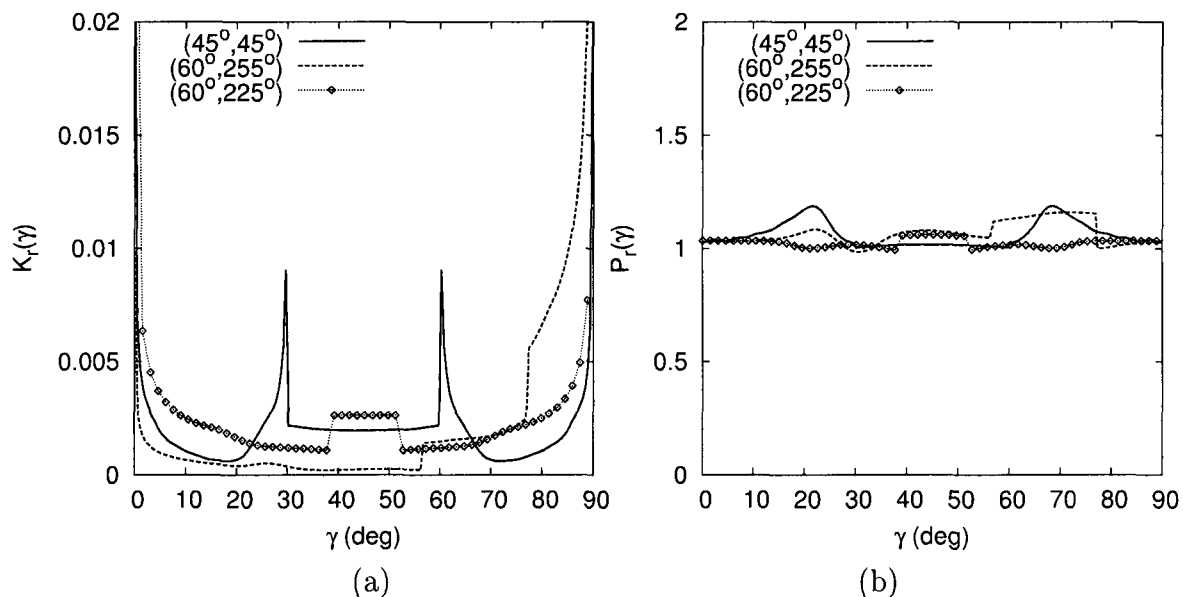
Figure 3.10: (a) Diffraction coefficient $K_r(\gamma)$ and (b) Phase factor $P_r(\gamma)$ for a 90° angular sector for a $\hat{\theta}_i$ polarized plane wave incident from the direction $(\theta_i, \phi_i) = (45°, 45°)$, $(\theta_i, \phi_i) = (60°, 255°)$ and $(\theta_i, \phi_i) = (60°, 225°)$.

The total current density obtained using the vertex-diffracted currents are integrated numerically to find the RCS of finite scattering structures of various shapes. First we consider the monostatic RCS of a 30° isosceles triangular plate depicted in
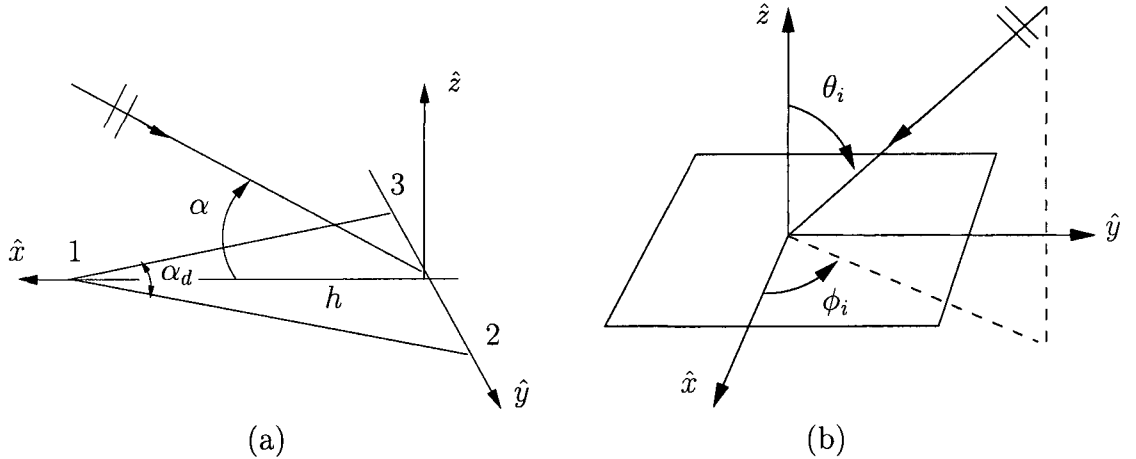
Figure 3.11: Scattering configurations for RCS calculations.

Fig. 3.11(a). The RCS pattern is calculated on the $x - z$ plane. This is the common scattering configuration that has been studied in the previous developments [22], [45], [17] to test the performance of the high-frequency solutions. In this configuration, because of the narrow tip angle ($\alpha_d = 30°$), the vertex-diffracted currents and the higher order interactions among the edges and corners makes a significant contribution to the RCS pattern when grazing directions are approached. Fig. 3.12(a) shows the copolar RCS of a triangular plate of height $h = 3\lambda$ for $\hat{\theta}_i$ polarized incident field. "PTD-1" denotes the RCS pattern that is obtained by using only the first order edge diffracted currents. In "PTD-2", the double diffracted FW currents are incorporated in the solution. "PTD+corners" is the pattern obtained using the total high frequency current. It is observed that the double-diffracted currents are of minor importance when the incident field is vertically ($\hat{\theta}_i$) polarized. On the other hand, the vertex-diffracted currents improve the accuracy of the RCS pattern by as much as 20 dB over the angular range $150° < \alpha < 180°$. This improvement is mainly due to the contributions from the vertex-excited currents at corner 1. Consider the vertex contributions when nose-on incidence is approached ($\alpha \simeq 0$). In this case, the incident E-field is perpendicular to the scattering surface. As a result, there is no
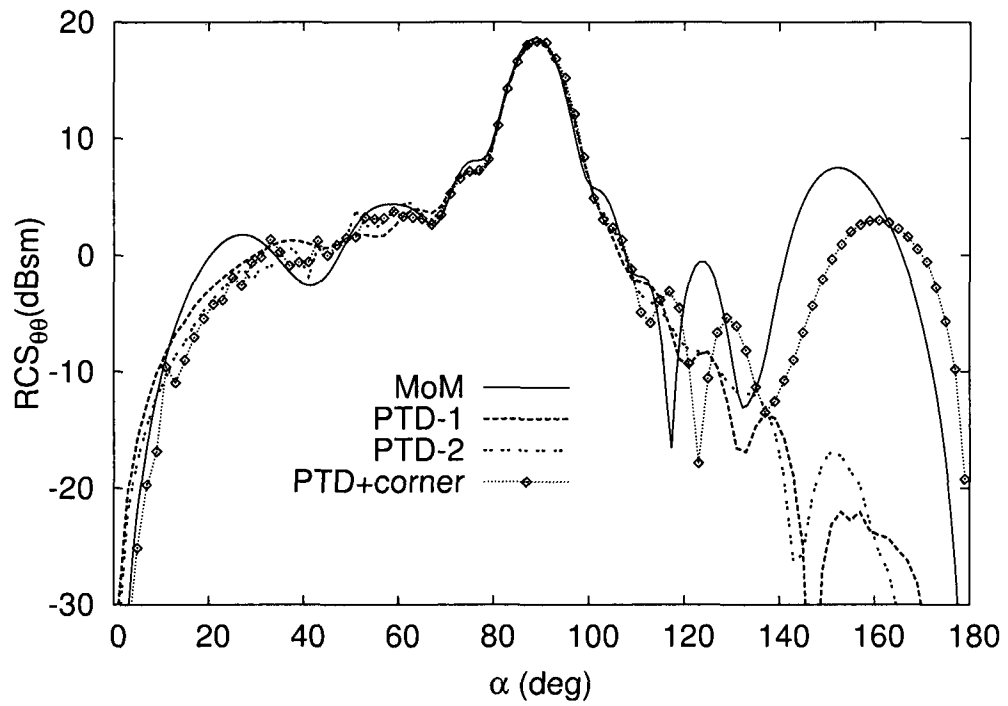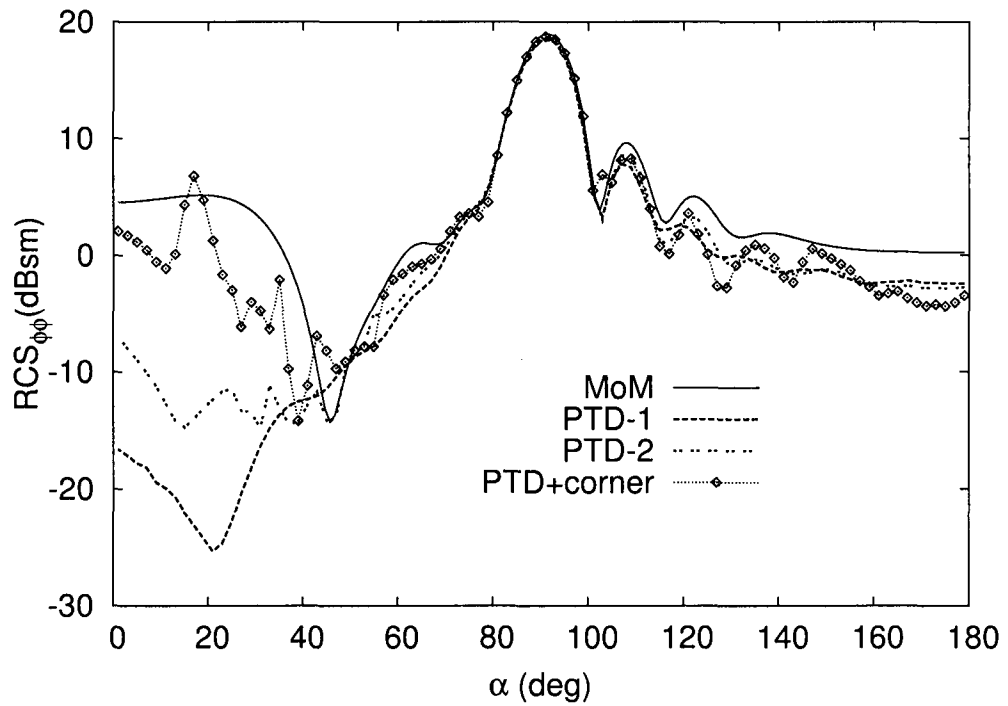
Figure 3.12: Monostatic RCS of a triangular plate. $h = 3\lambda$, $\alpha_d = 30°$. The RCS pattern is calculated on the x-z plane. α is measured from the positive x-axis. (a) $RCS_{\theta\theta}$ and (b) $RCS_{\phi\phi}$.

49
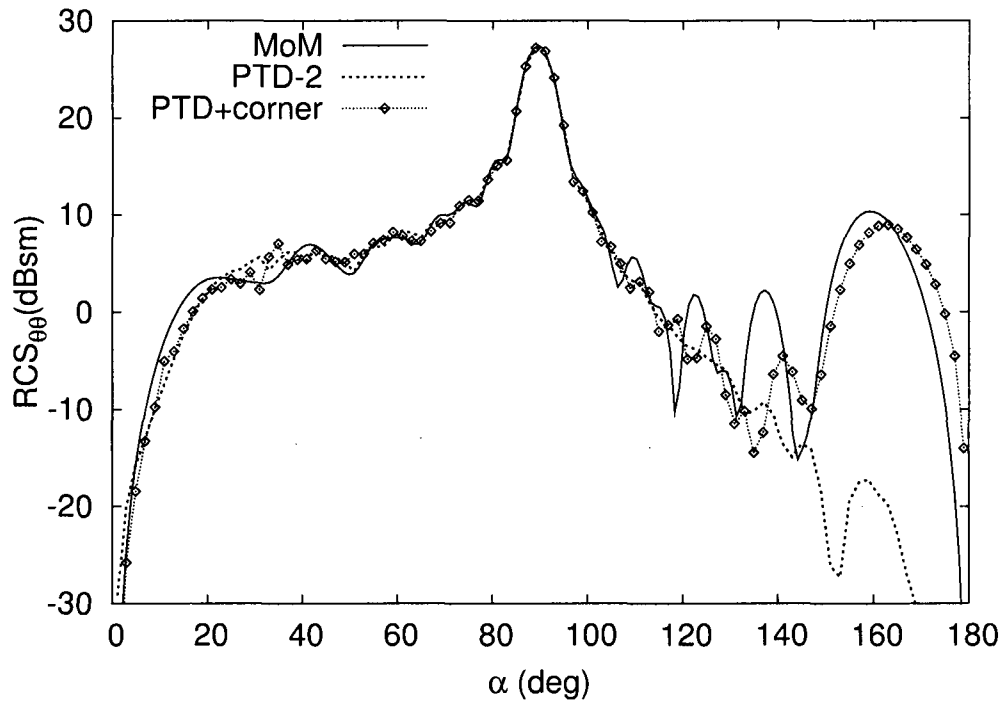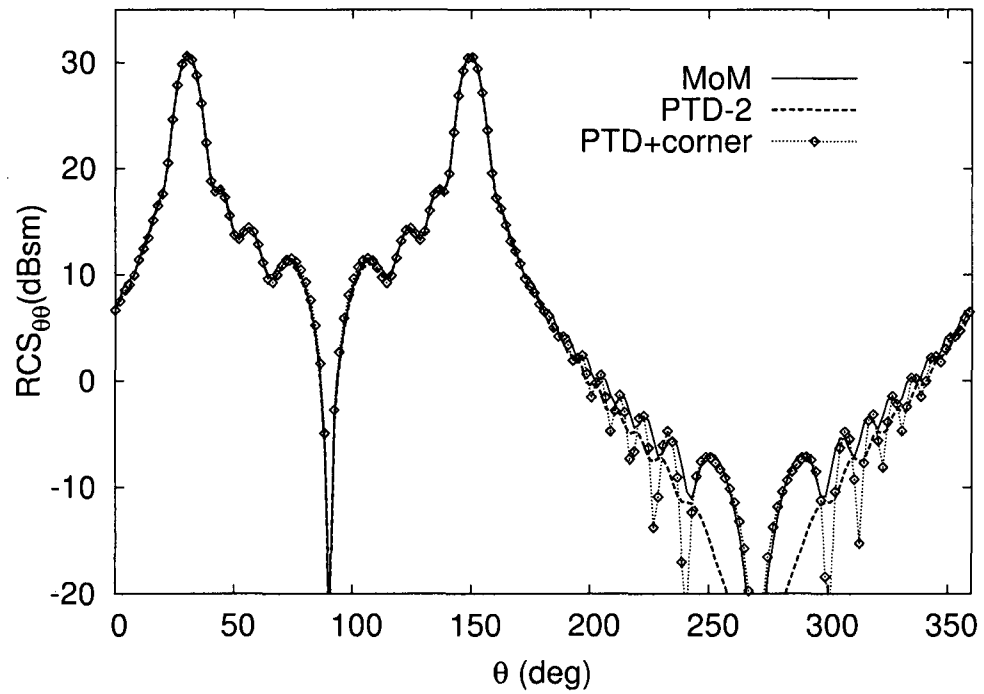
Figure 3.13: (a) Monostatic RCS of a triangular plate. $h = 5\lambda$, $\alpha_d = 30°$. (b) Bistatic RCS of a triangular plate for $(\theta_i, \phi_i) = (30°, 180°)$, $\phi_s = 0°$. $h = 8\lambda$, $\alpha_d = 20°$. The RCS patterns are calculated on the x-z plane. α is measured from the positive x-axis.

50

contribution from corner 1 and its two edges. The main contribution near nose-on incidence is due to the back edge and corners 2 and 3. The corner diffraction contribution due to these corners is very weak on the x-z plane. Thus, near nose-on incidence the RCS is dominated by the contributions from the edge along the y-axis. The small discrepancy around $\alpha \simeq 20°$ is attributed to the higher order interactions among the edges. As α approaches 180°, the far field is dominated by the contributions from corner 1. Fig. 3.12(b) shows the co-polar RCS pattern of the same triangular plate for $\hat{\phi}_i$ polarized incident field. Since the incident field in this case is parallel to the surface of the plate, the contribution from corner 1 is significant when nose-on incidence is approached. The effect of the double diffracted currents is evident in the RCS pattern. In calculating the double-diffracted currents, we employ ray tracing to find the first- and second-order diffraction points along the edges. Then we assume that the second-order diffraction point is illuminated by a plane wave. This assumption is valid when the two diffraction points are well separated. However, as the corner is approached, the first-order diffraction point becomes close to the second-order diffraction point and this assumption is no longer valid. For horizontal polarization ($\hat{\phi}_i$), the disagreement between the MoM and the PTD patterns over the angular range $0° < \alpha < 50°$ could be due to the incomplete modeling of the higher-order edge-diffracted currents. In this case, the vertex-diffracted currents act as a correction factor for the edge-diffracted currents. The resulting RCS pattern agrees reasonably well with the MoM pattern. It should be noted that, edge-wave mechanisms such as the corner-to-corner or corner-to-edge interactions are also strong for this polarization. Thus, the disagreement could partially be attributed to such higher-order effects that have not been incorporated in our calculations.

In order to demonstrate the effect of the higher order diffraction mechanisms that have not been incorporated in the solution, we consider the scattering configuration in the previous example with a triangular plate of $h = 5\lambda$. Fig. 3.13(a)

shows the co-polar RCS pattern for $\hat{\theta}_i$ polarized incident field. The resulting pattern ("PTD+corners") agrees better with the MoM pattern as compared to the previous example. It is noted in Fig. 3.13(a) that, the RCS pattern obtained using the MoM is almost completely reconstructed when the corner diffraction terms are included over the angular range $150° < \alpha < 180°$. This indicates that the discrepancy between the MoM and the "PTD+corners" pattern in Fig. 3.12(a) is indeed associated with the higher order mechanisms such as corner-to-corner and corner-to-edge interactions. As the plate size gets larger, the effect of these interactions become weaker. Even though not included in the present formulation, corner-to-corner and corner-to-edge interactions can be calculated with reasonable accuracy as demonstrated in [46]. Fig. 3.13(b) shows the RCS pattern for the same scattering configuration with $h = 8\lambda$ and $\alpha_d = 20°$. It is observed that even for such a narrow angled corner, the RCS pattern obtained using the MoM is recovered when the vertex-diffracted currents are included.

Fig. 3.14 shows the bistatic RCS of a square plate of width 5λ illustrated in Fig. 3.11(b). We consider the co-polar ($RCS_{\theta\theta}$) and cross-polar ($RCS_{\phi\theta}$) patterns for a $\hat{\theta}_i$ polarized field incident from the direction $(\theta_i, \phi_i) = (45°, 0°)$. The RCS pattern is calculated at $\phi_s = 60°$. Up to second-order edge-diffracted fields are included in the solution "PTD." For $RCS_{\theta\theta}$, the vertex-diffracted currents have a significant effect on the RCS pattern around $\theta = 90°$ and $\theta = 270°$. For the cross-polar case, the PTD approximation seems to perform much better. This indicates that corner diffraction is not as significant. Nevertheless, the resulting high-frequency pattern agrees well with the MoM result. Finally, in order to demonstrate the effect of vertex-diffracted currents for $\hat{\phi}_i$ polarized incident field, we consider the RCS of the 5λ plate for $(\theta_i, \phi_i) = (80°, 45°)$. The high-frequency pattern agrees very well with the MoM pattern for both polarizations as shown in Fig. 3.15 and Fig. 3.16. It should be noted that the RCS pattern is slightly overestimated near $\theta \simeq 240°$ and $\theta \simeq 300°$.
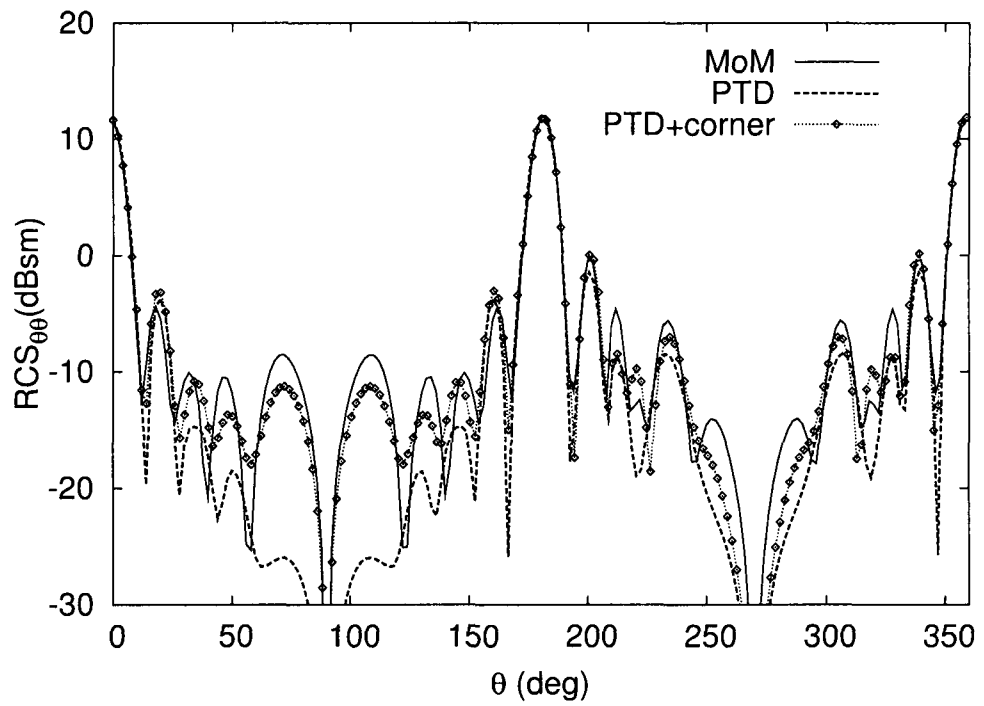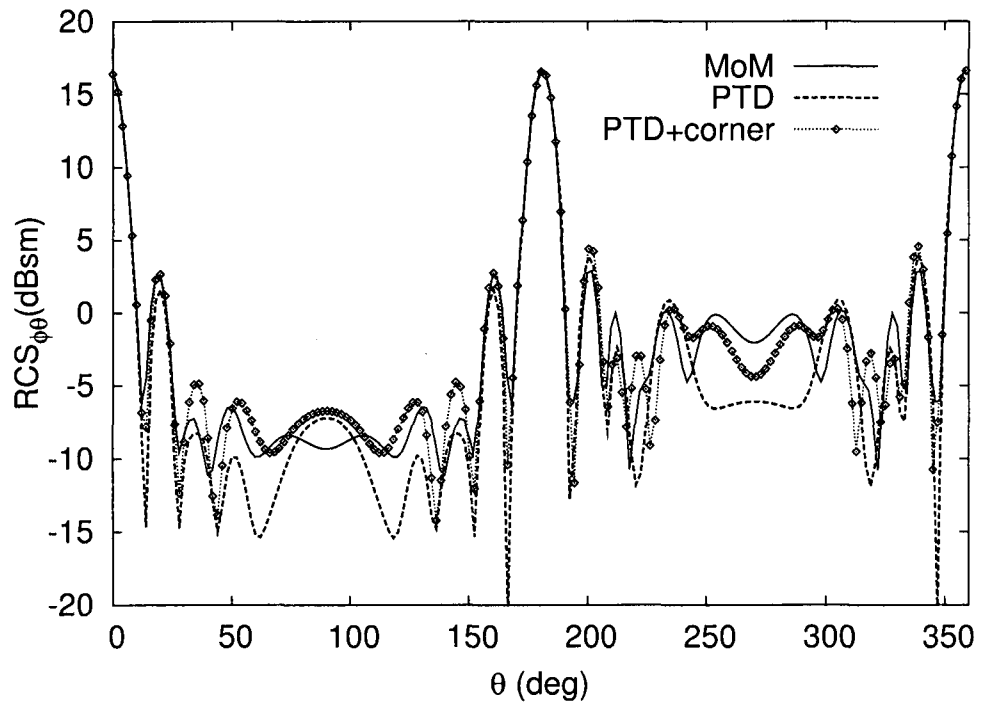
Figure 3.14: Bistatic RCS of a 5λ square plate. $(\theta_i, \phi_i) = (45°, 0°)$, $\phi_s = 60°$. (a) $RCS_{\theta\theta}$ and (b) $RCS_{\phi\theta}$.

This discrepancy is due to incomplete formulation of the double-diffracted currents and the higher-order diffraction mechanisms. Since the direction of incidence is close to grazing, higher-order interactions among different scattering centers, such as third order edge diffraction and corner-to-edge diffractions, could be significant in this case.

3.5 Conclusion

In this chapter, an approximate expression for the currents diffracted at the tip of an infinitely-thin, perfectly-conducting plane angular sector was derived. It was demonstrated that, based on the phase behavior, the vertex-diffracted current density can be modeled by

$$J^v = K(\gamma)(kr)^{-\alpha(\gamma)}e^{-jkP(\gamma)r}. \tag{3.12}$$

The unknown amplitude, phase and decay factors were calculated as a function of γ, the angular position of the observation point on the plane angular sector. It should be noted that, the unknown factors were derived using the current density induced on a plane angular sector, which is a semi-infinite structure. In order to calculate the vertex-diffracted current density from a given corner of a finite polyhedral structure, the canonical modeling that is used in traditional ray-optical methods such as the GTD or the UTD is used. The canonical modeling is based on the assumption that near the corner of the finite scatterer, the vertex-diffracted current density is well approximated by that of a semi-infinite plane angular sector that conforms to the finite scatterer at the corner that is being considered. Thus, the interaction of the vertex-diffracted currents with the rest of the scatterer was assumed to negligible. The accuracy of the vertex-diffracted currents was verified by direct comparisons with the exact current density. The effect of the vertex-diffracted currents on the RCS was also illustrated using various scattering configurations.
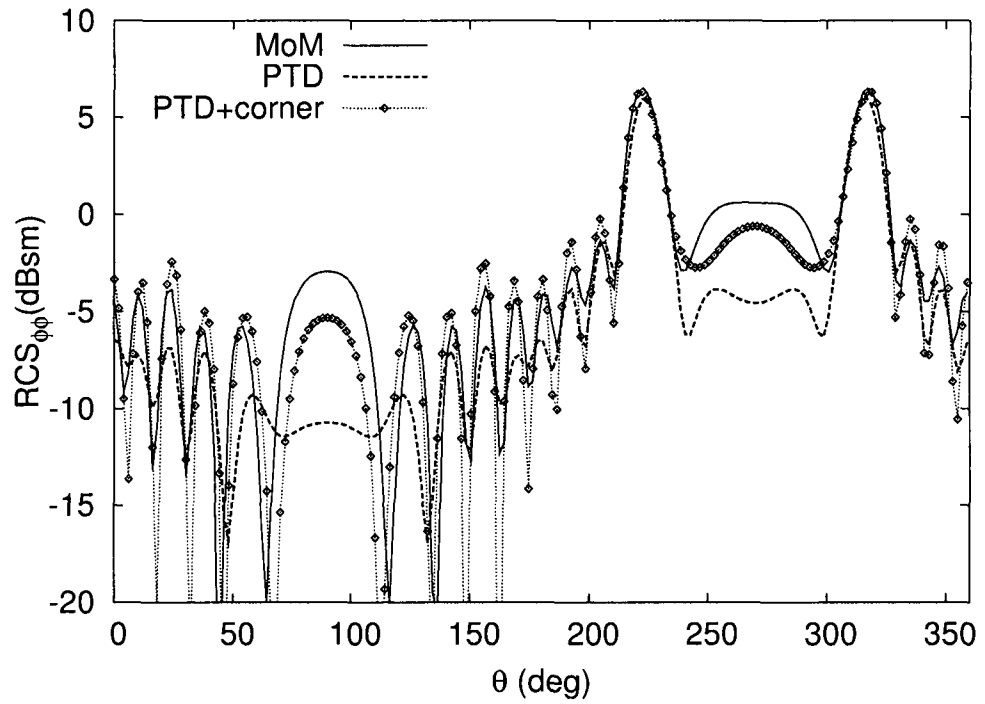
(a)
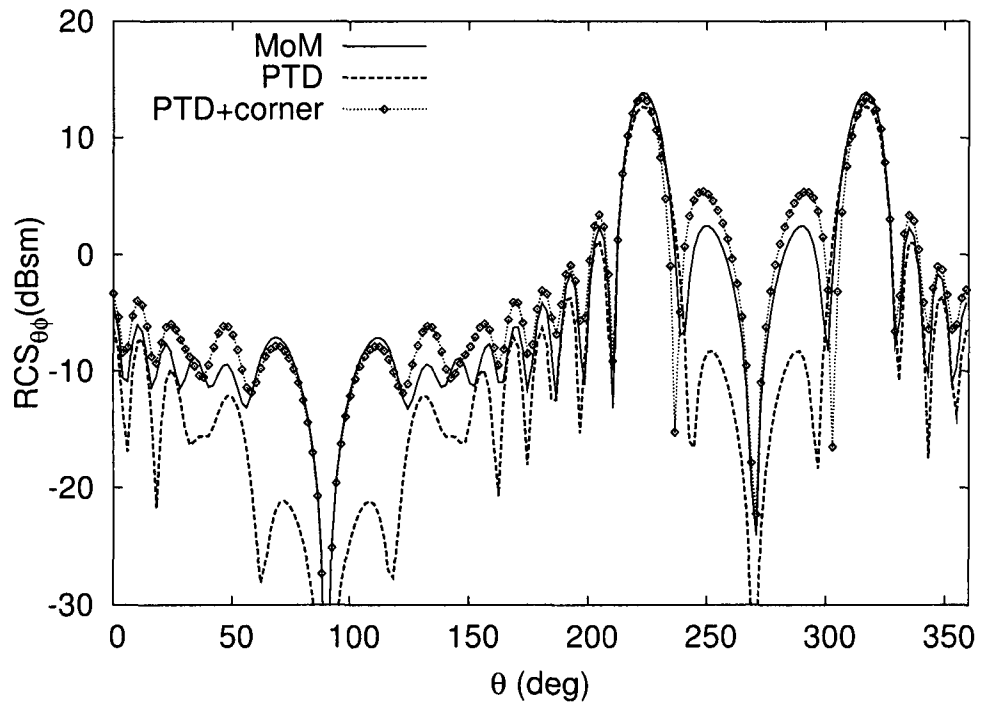
(b)

Figure 3.15: Bistatic RCS of a 5λ square plate. $(\theta_i, \phi_i) = (80°, 45°)$, $\phi_s = 90°$. (a) $RCS_{\phi\phi}$ and (b) $RCS_{\theta\phi}$.
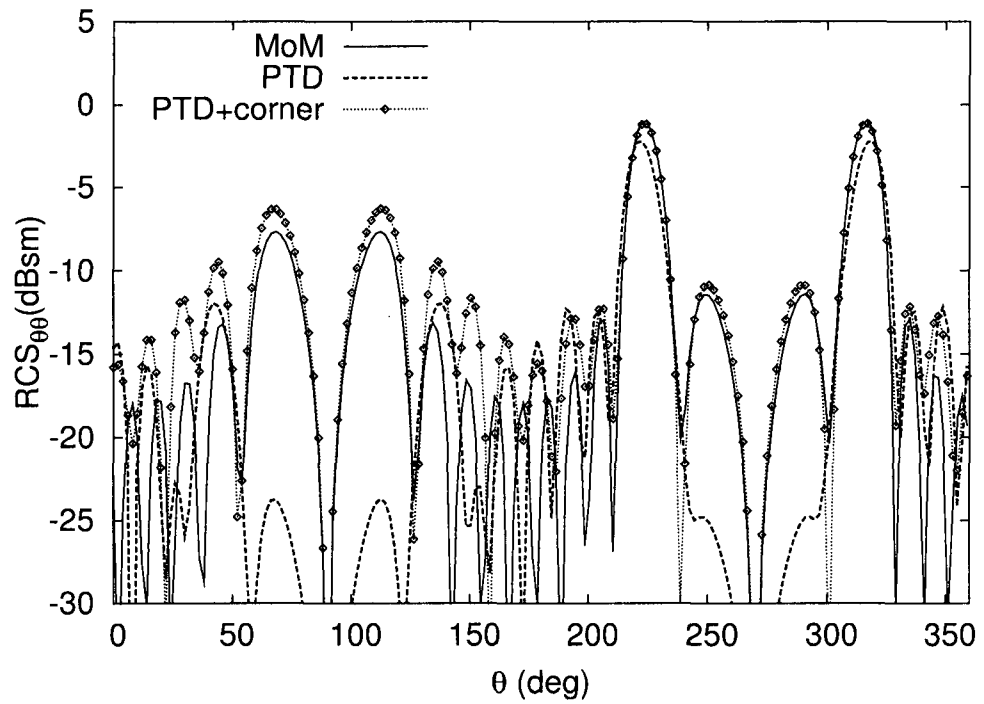
(a)
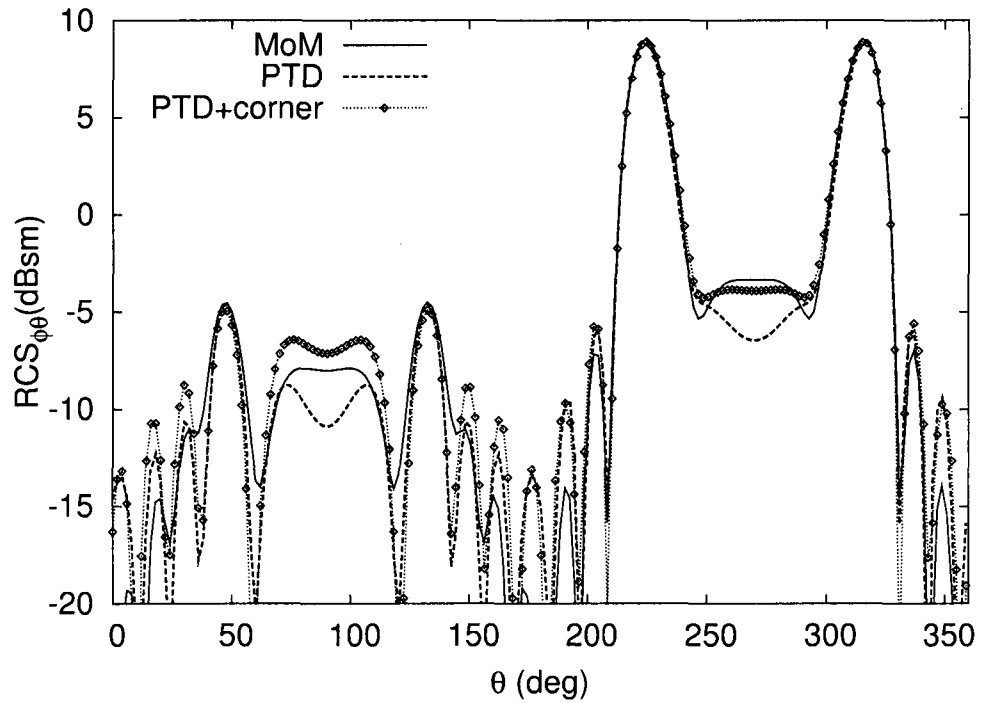
(b)

Figure 3.16: Bistatic RCS of a 5λ square plate. $(\theta_i, \phi_i) = (80°, 45°)$, $\phi_s = 90°$. (a) $RCS_{\theta\theta}$ and (b) $RCS_{\phi\theta}$.

56

Chapter 4

First Order Singular Basis Functions for Corner Diffraction Analysis

4.1 Introduction

This chapter presents the formulation of the first order singular basis functions in detail. We consider electromagnetic scattering from an infinitely-thin perfectly-conducting polygonal scatterer. In the solution of integral equations by the MoM, the triangular patch basis functions developed by Rao, Wilton and Glisson [35] have become the most widely used approach for modeling the surface current density on such scatterers. In this chapter, we develop a set of divergence-conforming basis functions to overcome the inherent limitations of the RWG basis functions near the sharp edges and corners of a scatterer. The new basis functions which are used in the boundary patches that are adjacent to the geometrical edge or a corner of the

polygonal scatterer will be referred to as "first-order singular." By enforcing the edge and corner conditions, the first-order basis functions will be modified to include the correct behavior of the surface current density near the edges and corners of the scatterer. Section 4.2 describes the derivation of the singular basis functions. In Section 4.3, the accuracy of the singularity approximations is investigated through direct comparisons with the exact current density. Section 4.4 summarizes briefly the use of the MPM and the extraction procedure. Finally, the current density obtained using the first-order-singular basis functions is compared with the exact current density for various scattering configurations in Section 4.5. Throughout this chapter, the commonly-used notation for normalized area coordinates [31], [47] is adopted. The normalized area coordinate system, evaluation of the matrix elements and the numerical integration procedures for the singular basis functions in the MoM solution are described in Appendix D. This chapter has been published in [48].

4.2 Singular Basis Functions

Consider the RWG triangle pair depicted in Fig. 4.1. The vertices of each individual triangle are numbered in a counter-clockwise sense starting from the free vertex. First-order basis functions [34] consist of two vector basis functions at each edge ℓ_m given by

$$\bar{f}_{R,1}(\bar{r}) = \begin{cases} -\frac{\ell_m}{2A^+}\xi_{i-1}\bar{\ell}_{i+1}, & r \in T^+ \\ -\frac{\ell_m}{2A^-}\xi_{i+1}\bar{\ell}_{i-1}, & r \in T^- \end{cases} \tag{4.1}$$

$$\bar{f}_{R,2}(\bar{r}) = \begin{cases} \frac{\ell_m}{2A^+}\xi_{i+1}\bar{\ell}_{i-1}, & r \in T^+ \\ \frac{\ell_m}{2A^-}\xi_{i-1}\bar{\ell}_{i+1}, & r \in T^- \end{cases} \tag{4.2}$$

where ξ are the area coordinates defined locally in each triangle [47]. According to the edge condition, the component of the current density parallel to the edge is proportional to $d^{\nu-1}$, where d is the perpendicular distance to the edge and ν is the
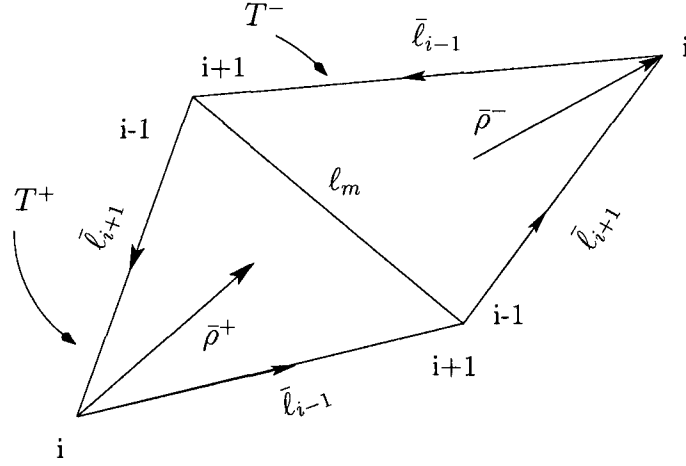
Figure 4.1: RWG triangle pair and the local indexing scheme.

singularity exponent whose value can be obtained by employing the edge condition for different wedge angles [25]. When triangular subsections are used, two types of singularities are encountered. Consider the edge triangles shown in Fig. 4.2, where the dashed line represents a surface boundary edge. The edge singularity must be placed along $\bar{\ell}_1$ in a triangle of type T_1 and at vertex 4 in a triangle of type T_2. Assuming that the edge vector $\bar{\ell}_4$ is parallel to the boundary edge, the perpendicular distance to the edge can be expressed as

$$d = \begin{cases} \frac{2A_1}{|\ell_1|}\xi_1, & r \in T_1 \\ \frac{2A_2}{|\ell_4|}(1 - \xi_4), & r \in T_2 \end{cases} \tag{4.3}$$

where A_1 and A_2 are the areas of T_1 and T_2 respectively. It follows from (4.3) that the basis functions in T_1 and T_2 must be proportional to $\xi_1^{\nu-1}$ and $(1 - \xi_4)^{\nu-1}$ respectively. The singular behavior will be incorporated into the basis functions associated with the element edges $\bar{\ell}_2$, $\bar{\ell}_3$, and $\bar{\ell}_4$. Notice from Fig. 4.2 that the element edges $\bar{\ell}_5$ and $\bar{\ell}_6$ are of the same type as $\bar{\ell}_2$ and $\bar{\ell}_3$ respectively. No basis function is defined for the surface boundary edges ($\bar{\ell}_1$) as in the RWG formulation. A suitable basis function for each edge can be obtained as the product of the corresponding first-order basis function and the necessary singularity. For notational simplicity, we assume that the

59
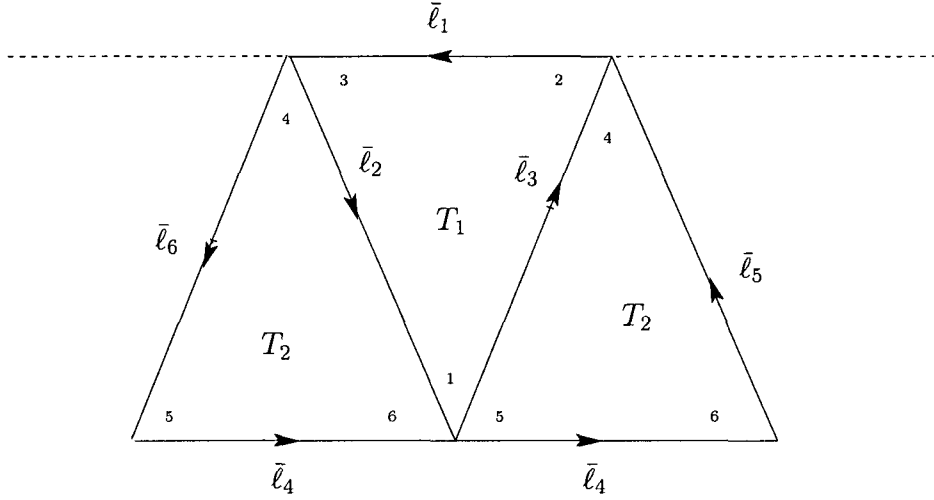
Figure 4.2: Triangular subsections adjacent to the boundary edge (dashed line).

direction of current flow is inwards for triangles of type T_1 and outwards for triangles of type T_2. Using (4.1) and (4.2), the first-order-singular basis functions associated with edge 2 are obtained as the product of the associated first order basis function and the required singularity

$$\bar{f}_{2,1}(\bar{r})=\begin{cases} -\frac{\ell_2}{2A_1}\xi_3\xi_1^{\nu-1}\bar{\ell}_1, & r \in T_1 \\ -\frac{\ell_2}{2A_2}\xi_4(1-\xi_4)^{\nu-1}\bar{\ell}_6, & r \in T_2 \end{cases} \qquad (4.4)$$

$$\bar{f}_{2,2}(\bar{r})=\begin{cases} \frac{\ell_2}{2A_1}\xi_1^{\nu}\bar{\ell}_3, & r \in T_1 \\ \frac{\ell_2}{2A_2}\xi_6(1-\xi_4)^{\nu-1}\bar{\ell}_4, & r \in T_2 \end{cases} \qquad (4.5)$$

where ℓ_2 represents the length of edge 2. In order to show that the normal component of the current is continuous, let us define a surface tangent normal to $\bar{\ell}_2$ as

$$\hat{t}_2 = \hat{n} \times \hat{\ell}_2$$

where $\hat{n}$ is the surface normal. For T_1, the normal components of $\bar{f}_{2,1}$ and $\bar{f}_{2,2}$ along edge 2 are

$$\bar{f}_{2,1}(\bar{r}) \cdot \hat{t}|_{T_1}=\xi_3\xi_1^{\nu-1} \qquad (4.6)$$

$$\bar{f}_{2,2}(\bar{r}) \cdot \hat{t}|_{T_1}=\xi_1^{\nu}. \qquad (4.7)$$

60

Similarly for T_2,

$$\bar{f}_{2,1}(\bar{r}) \cdot \hat{t}|_{T_2} = \xi_4(1 - \xi_4)^{\nu-1} = \xi_4\xi_6^{\nu-1} \tag{4.8}$$

$$\bar{f}_{2,2}(\bar{r}) \cdot \hat{t}|_{T_2} = \xi_6(1 - \xi_4)^{\nu-1} = \xi_6^{\nu}. \tag{4.9}$$

For a point at the common edge $\bar{\ell}_2$, ξ_3 in T_1 is equal to ξ_4 in T_2, and ξ_1 in T_1 is equal to ξ_6 in T_2. Therefore, the normal components of $\bar{f}_{2,1}$ and $\bar{f}_{2,2}$ across edge 2 are continuous. The first-order-singular basis functions associated with edge 3 and edge 4 may similarly be obtained as

$$\bar{f}_{3,1}(\bar{r}) = \begin{cases} -\frac{\ell_3}{2A_1}\xi_1^{\nu}\bar{\ell}_2, & r \in T_1 \\ -\frac{\ell_3}{2A_2}\xi_5(1 - \xi_4)^{\nu-1}\bar{\ell}_4, & r \in T_2 \end{cases} \tag{4.10}$$

$$\bar{f}_{3,2}(\bar{r}) = \begin{cases} \frac{\ell_3}{2A_1}\xi_2\xi_1^{\nu-1}\bar{\ell}_1, & r \in T_1 \\ \frac{\ell_3}{2A_2}\xi_4(1 - \xi_4)^{\nu-1}\bar{\ell}_5, & r \in T_2 \end{cases} \tag{4.11}$$

$$\bar{f}_{4,1}(\bar{r}) = -\frac{\ell_4}{2A_2}\xi_6(1 - \xi_4)^{\nu-1}\bar{\ell}_5 \tag{4.12}$$

$$\bar{f}_{4,2}(\bar{r}) = \frac{\ell_4}{2A_2}\xi_5(1 - \xi_4)^{\nu-1}\bar{\ell}_6. \tag{4.13}$$

It should be noted that $\bar{\ell}_4$ is the common edge for a triangle of type T_2 and an inner triangle. Therefore, $\bar{f}_{4,1}$ and $\bar{f}_{4,2}$ are defined only over T_2. For points located at edge 4, $\xi_4 = 0$. Consequently, (4.12) and (4.13) reduce to the regular first-order basis functions. Therefore, continuity across edge 4 is guaranteed. The surface divergence of an arbitrary vector of the form $\bar{f} = f_i\bar{\ell}_i + f_{i+1}\bar{\ell}_{i+1} + f_{i-1}\bar{\ell}_{i-1}$ is given by

$$\nabla_s \cdot \bar{f} = (\frac{\partial}{\partial\xi_{i-1}} - \frac{\partial}{\partial\xi_{i+1}})f_i + (\frac{\partial}{\partial\xi_i} - \frac{\partial}{\partial\xi_{i-1}})f_{i+1} + (\frac{\partial}{\partial\xi_{i+1}} - \frac{\partial}{\partial\xi_i})f_{i-1}. \tag{4.14}$$

First-order-singular basis functions and their surface divergences obtained using (4.14) are listed in Table 4.3, where it is understood that ℓ and A are the length and area of the element associated with the corresponding basis function. Fig. 4.3 and Fig. 4.4 illustrate the basis functions in the boundary triangles. It is assumed that
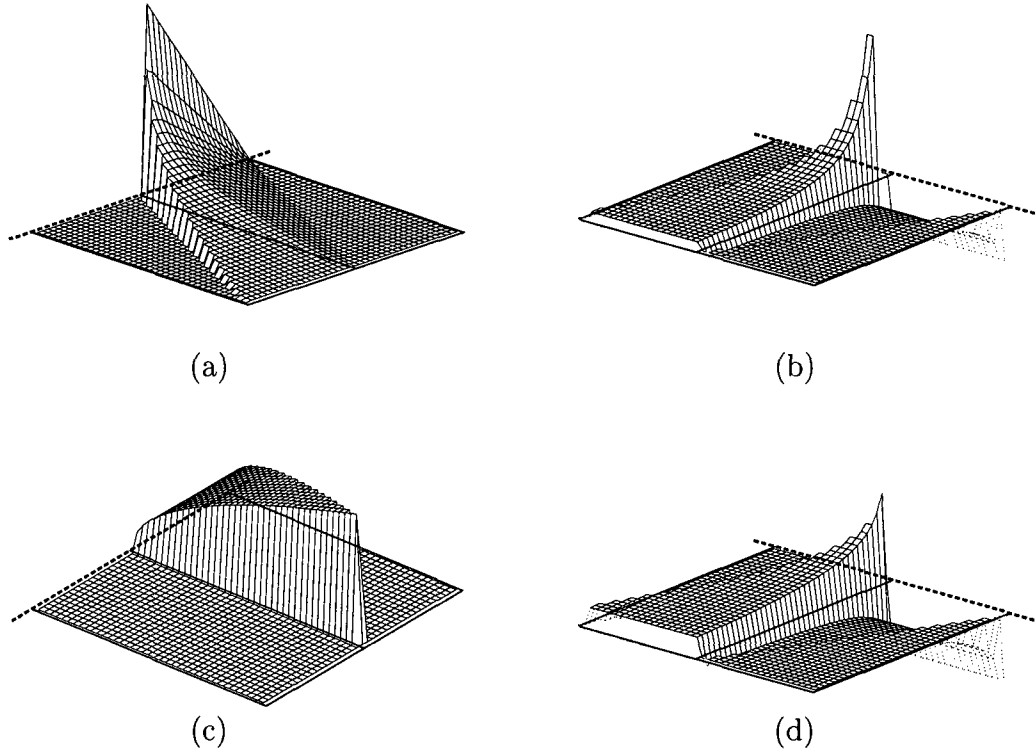
Figure 4.3: First-order-singular basis functions. (a) $\bar{f}_{2,1} \cdot \hat{x}$, (b)$\nabla_s \cdot \bar{f}_{2,1}$, (c) $\bar{f}_{2,2} \cdot \hat{y}$, (d)$\nabla_s \cdot \bar{f}_{2,2}$.

the surface boundary edges (dashed lines in the figures) are parallel to $\hat{x}$. The basis functions parallel to the surface boundary edge are proportional to $d^{\nu-1}$ as expected (Fig. 4.3(a), Fig. 4.4(a)). On the other hand, the basis functions that have a component perpendicular to the edge are proportional to d^{ν} (Fig. 4.3(c), Fig. 4.4(c)). This is the correct behavior for the current flowing perpendicular to the edge. Unlike previous developments, this allows both components to be modeled accurately in the MoM solution. It is evident from Fig. 4.3 and Fig. 4.4 that the charge density (surface divergence of the basis functions) is in the form of pulse doublets [49],
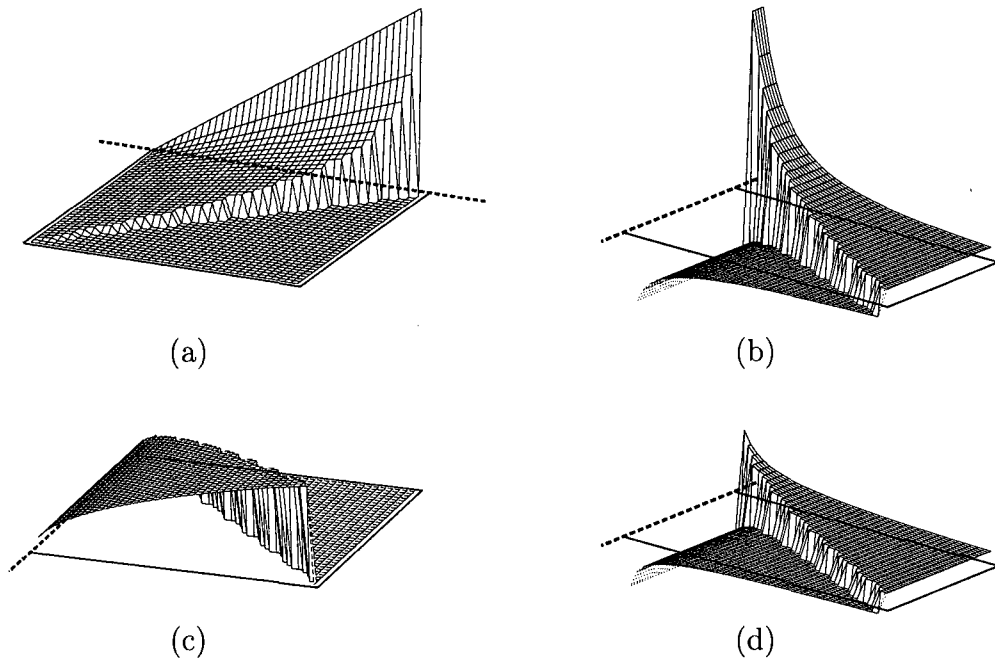
Figure 4.4: First-order-singular basis functions. (a) $\bar{f}_{3,1} \cdot \hat{x}$, (b)$\nabla_s \cdot \bar{f}_{3,1}$, (c) $\bar{f}_{3,2} \cdot \hat{y}$, (d)$\nabla_s \cdot \bar{f}_{3,2}$.

ensuring that no charge accumulation appears on the surface. It should be noted that the correct behavior for the charge density is only approximately satisfied inside T_2 for $\bar{f}_{2,1}$, $\bar{f}_{3,2}$ and $\bar{f}_4$. However, this does not cause any considerable inaccuracy as demonstrated by the numerical results. The correct behavior for the surface charge density is satisfied in T_1 and there is no charge accumulation at the boundary edge $\bar{\ell}_1$. It is possible to obtain the correct behavior for the surface charge density in the edge triangles. First, it is assumed that the charge density in T_1 and T_2 are proportional to $\xi_1^{\nu-1}$ and $(1-\xi_4)^{\nu-1}$ respectively. Then, the expressions for the singular basis functions are obtained by using the equation of continuity [28]. However, the

resulting basis functions do not satisfy the correct behavior of the current density in triangles of type T_2 in this approach. Proper modeling of the surface charge density is of considerable importance at low frequencies. It has been shown in [50] that the elements of the MoM matrix elements at low frequencies are dominated by the scalar potential contributions. As a consequence, the effect of the incorrect behavior of the surface charge density on the accuracy of the MoM solution becomes substantial when the scattering surface is much smaller than a wavelength.

Table 4.3: First order edge basis functions, $M = \ell/2A$

	T_1	T_2
$\bar{f}_{2,1}$	$-M\xi_3\xi_1^{\nu-1}\bar{\ell}_1$	$-M\xi_4(1-\xi_4)^{\nu-1}\bar{\ell}_6$
$\nabla_s \cdot \bar{f}_{2,1}$	$-M\xi_1^{\nu-1}$	$M(1-\nu\xi_4)(1-\xi_4)^{\nu-2}$
$\bar{f}_{2,2}$	$M\xi_1^{\nu}\bar{\ell}_3$	$M\xi_6(1-\xi_4)^{\nu-1}\bar{\ell}_4$
$\nabla_s \cdot \bar{f}_{2,2}$	$-M\nu\xi_1^{\nu-1}$	$M(1-\xi_4)^{\nu-1}$
$\bar{f}_{3,1}$	$-M\xi_1^{\nu}\bar{\ell}_2$	$-M\xi_5(1-\xi_4)^{\nu-1}\bar{\ell}_4$
$\nabla_s \cdot \bar{f}_{3,1}$	$-M\nu\xi_1^{\nu-1}$	$M(1-\xi_4)^{\nu-1}$
$\bar{f}_{3,2}$	$M\xi_2\xi_1^{\nu-1}\bar{\ell}_1$	$M\xi_4(1-\xi_4)^{\nu-1}\bar{\ell}_5$
$\nabla_s \cdot \bar{f}_{3,2}$	$-M\xi_1^{\nu-1}$	$M(1-\nu\xi_4)(1-\xi_4)^{\nu-2}$
$\bar{f}_{4,1}$	-	$-M\xi_6(1-\xi_4)^{\nu-1}\bar{\ell}_5$
$\nabla_s \cdot \bar{f}_{4,1}$	-	$M(\nu\xi_6+\xi_5)(1-\xi_4)^{\nu-2}$
$\bar{f}_{4,2}$	-	$M\xi_5(1-\xi_4)^{\nu-1}\bar{\ell}_6$
$\nabla_s \cdot \bar{f}_{4,2}$	-	$M(\nu\xi_5+\xi_6)(1-\xi_4)^{\nu-2}$

Next, we use a similar procedure to obtain corner basis functions. The behavior of current density at the tip of a plane angular sector has been studied in [25]. We use basis functions proportional to ρ^τ, where ρ is the distance to the corner. Consider the triangle pair at a surface corner depicted in Fig. 4.5. The dashed lines represent surface boundary edges. The corner behavior can be incorporated into the basis functions related to any edge element in the corner triangles. For simplicity, the

behavior of current density near the corner will be incorporated into the basis function associated with the edge element ℓ_c. It is required that $\hat{\ell}_4 \perp \hat{\ell}_6$ and $\hat{\ell}_2 \perp \hat{\ell}_1$. In triangles of type C_1 and C_2, ρ can be expressed in terms of area coordinates as

$$
\rho = \begin{cases} ([\frac{2A_1}{|\ell_1|}\xi_1]^2 + [\frac{2A_1}{|\ell_2|}(1-\xi_2)]^2)^{\frac{1}{2}}, & r \, \epsilon \, C_1 \\ ([\frac{2A_2}{|\ell_4|}\xi_4]^2 + [\frac{2A_2}{|\ell_6|}(1-\xi_6)]^2)^{\frac{1}{2}}, & r \, \epsilon \, C_2 \end{cases} \tag{4.15}
$$

where A_1 and A_2 denote the areas of C_1 and C_2 respectively. The corner basis functions are obtained as the product of the corresponding first order basis functions and the factor ρ^τ and are given by

$$
\bar{f}_{c,1}(\bar{r}) = \begin{cases} -\frac{\ell_c}{2A_1}\xi_1\rho^\tau\bar{\ell}_2, & r \, \epsilon \, C_1 \\ -\frac{\ell_c}{2A_2}\xi_4\rho^\tau\bar{\ell}_6, & r \, \epsilon \, C_2 \end{cases}
$$

$$
\bar{f}_{c,2}(\bar{r}) = \begin{cases} \frac{\ell_c}{2A_1}\xi_2\rho^\tau\bar{\ell}_1, & r \, \epsilon \, C_1 \\ \frac{\ell_c}{2A_2}\xi_6\rho^\tau\bar{\ell}_4, & r \, \epsilon \, C_2. \end{cases} \tag{4.16}
$$

The direction of current flow is assumed to be towards C_1. It is straightforward to show that the normal component of the current density across ℓ_c is continuous. Consider the behavior of the corner basis functions in C_1. Since $\xi_1 = 0$ at the corner, $\bar{f}_{c,1}$ vanishes in a certain manner as the corner is approached as shown in Fig. 4.6. When $\tau < 0$, $\bar{f}_{c,2}$ becomes singular at the corner. Hence, similar to the edge basis functions, the corner basis functions are also capable of modeling both singular and finite currents depending on the value of τ. The corresponding functions for the surface charge density can be obtained by calculating the surface divergence of the corner basis functions. By calculating the surface charge density in the corner triangles, it was observed that $\nabla_s \cdot \bar{f}_{c,2}$ agrees fairly well with the expected behavior $\rho^{\tau-1}$. However, $\nabla_s \cdot \bar{f}_{c,1}$ does not show the correct behavior. The dominant component of the current density in the corner triangles is $\bar{f}_{c,2}$. Notice that $\bar{f}_{c,1}$ is along $\bar{\ell}_2$ and $\bar{\ell}_6$, which are perpendicular to the boundary edges of the quarter plane. Near the corner, the surface divergence of $\bar{f}_{c,1}$ is negligibly small compared to that of $\bar{f}_{c,2}$. Therefore, the incorrect behavior of $\nabla_s \cdot \bar{f}_{c,1}$ does not cause any substantial error.
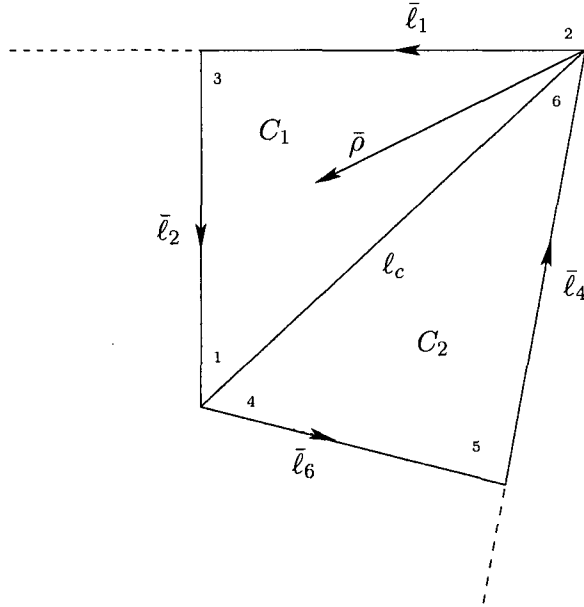
Figure 4.5: Triangular subsections at the corner. Dashed line represents the surface boundary. $\hat{\ell}_4 \perp \hat{\ell}_6$ and $\hat{\ell}_2 \perp \hat{\ell}_1$.

4.3 Edge Singularities

In order to demonstrate the validity of the singularity modeling near the edges, we consider the current density induced on a plane angular sector of 90° located in the x-y plane ($x > 0$, $y > 0$). The current density is calculated along the cut $x = 4\lambda$, $0 \leq y \leq 0.5\lambda$ using the exact eigenfunction formulation. According to the leading-term approximation for the half plane, the singularity of the current density parallel to the edge is described by $(kd)^{-0.5}$, where d is the perpendicular distance to the edge. Fig. 4.7(a) shows the parallel component of the current density J_x for a $\hat{\phi}_i$ polarized field incident from the direction $(\theta_i, \phi_i) = (5°, 270°)$. It is observed that, the leading-term approximation is valid only in the immediate vicinity of the edge. Fig. 4.7(b) shows J_x for $(\theta_i, \phi_i) = (65°, 270°)$. In this case, the current density is well approximated by $(kd)^{-0.5}$. Since the E-field is parallel to the edge in this example, the normal component of the current J_y is zero. The parallel and perpendicular

66
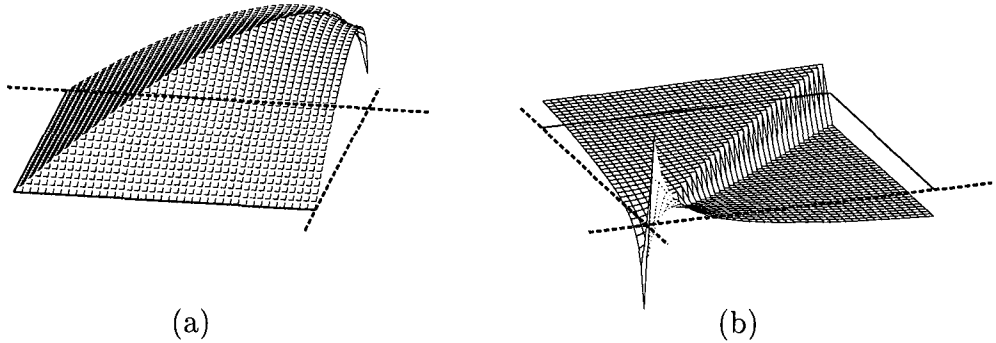
Figure 4.6: First-order-singular basis functions. (a) $|\bar{f}_{c,2}|$. (b)$\nabla_s \cdot \bar{f}_{c,2}$.

components of the current density for a $\hat{\theta}_i$ polarized field incident from the direction $(\theta_i, \phi_i) = (5°, 260°)$ are shown in Fig. 4.7(c) and (d) respectively. The leading-term approximation fails for the parallel component near the edge. For the perpendicular component, the approximation $(kd)^{0.5}$ is valid for $y < 0.1\lambda$. In general, the region over which the leading-term approximation is valid becomes larger as edge-on incidence is approached. Furthermore, the validity of the singularity approximations depends on both the polarization and direction of incidence. Similar behavior was observed for the corner basis functions. The size of the edge and corner triangles are limited by the range over which the leading-term approximation of the singular behavior is dominant.
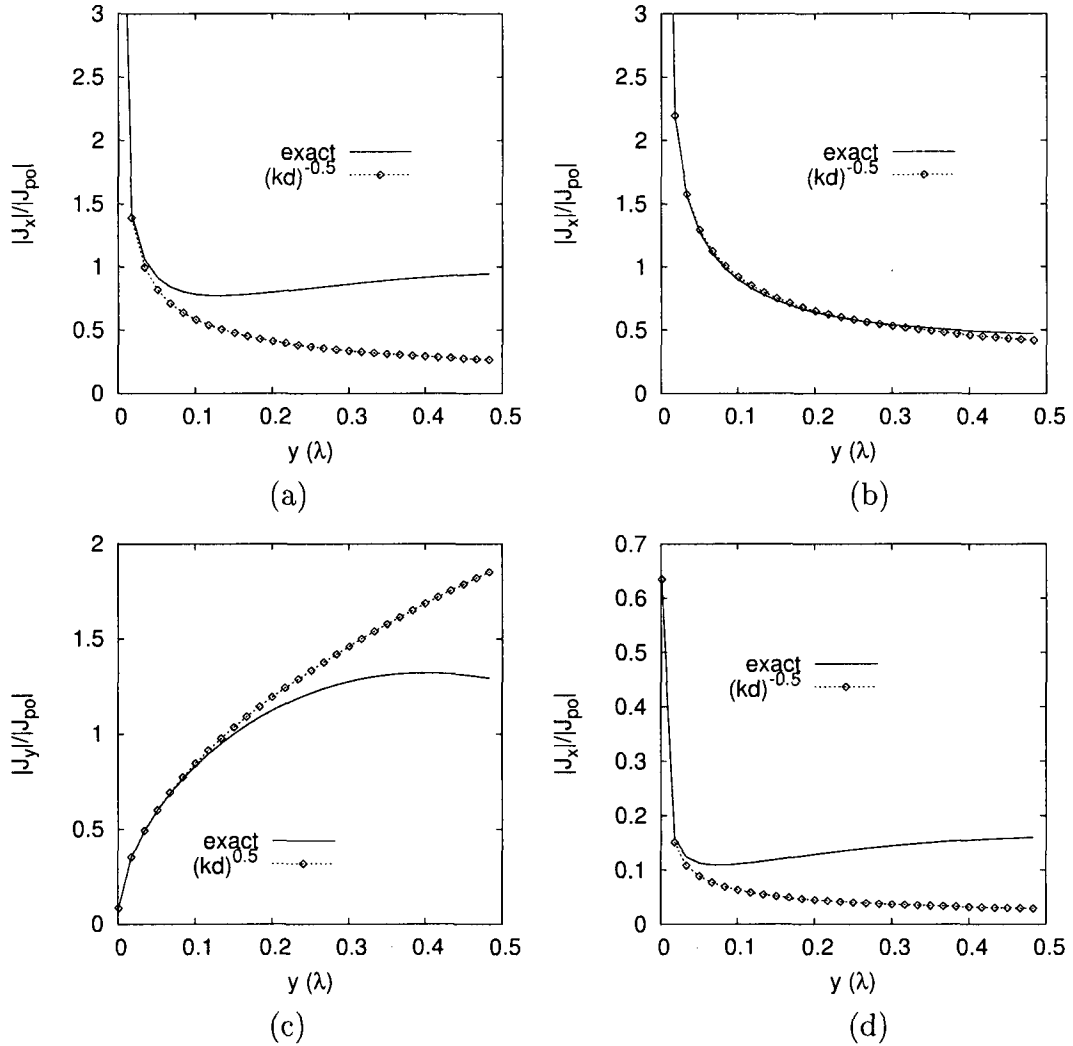
Figure 4.7: Current density along the cut $x = 4\lambda$, $0 \le y \le 0.5\lambda$. (a) $\hat{\phi}_i$ polarization, $(\theta_i, \phi_i) = (5°, 270°)$. (b) $\hat{\phi}_i$ polarization, $(\theta_i, \phi_i) = (65°, 270°)$. (c), (d) $\hat{\theta}_i$ polarization, $(\theta_i, \phi_i) = (5°, 260°)$.
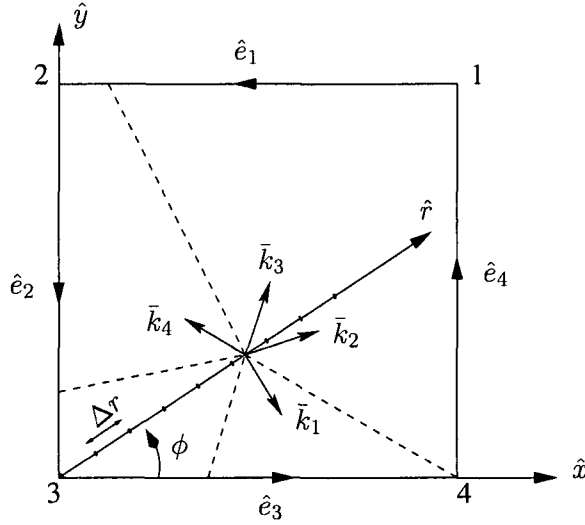
Figure 4.8: Sampling direction $\hat{r}$ and various components of $J_{r,\phi}^{mm}$.

4.4 Extraction of Currents

Consider a perfectly conducting quarter plane located in the first quadrant of the x-y plane illuminated by a plane wave. The total current density at a given point on the surface is composed of diffraction contributions from the two edges, and the corner and the multiple diffractions among the edges. In order to obtain the current density on the quarter plane, the MoM is employed over a finite rectangular region close to the corner defined by $\hat{e}_1$ and $\hat{e}_4$ as depicted in Fig. 4.8. This truncation introduces extraneous diffraction centers that affect the surface current density. The contributions due to these extraneous diffraction centers can be eliminated from the MoM current by using the MPM.

The current density obtained using the MoM is sampled at constant intervals Δr along a radial cut $\hat{r}$ from the tip (corner 3) of the angular sector. The sampling direction and propagation vectors of various contributions are shown in Fig. 4.8. $\bar{k}_4$ represents the corner diffracted current from corner 4 and $\bar{k}_1 - \bar{k}_3$ are the edge diffracted currents due to edges 1, 2 and 3 respectively. Along $\hat{r}$, the $\hat{r}$ and $\hat{\phi}$ components of

the current density can be described by

$$J_{r,\phi}^{MoM}(\phi, m\Delta r) = \sum_{n=1}^{N} C_{r,\phi}^{(n)}(\phi) e^{-j P_{r,\phi}^{(n)}(\phi) \hat{k}_n \cdot \hat{r} m \Delta r},$$

$$m = 1, ..., M \qquad (4.17)$$

where N represents the number of ray contributions, and $C_{r,\phi}^{(n)}$ and $P_{r,\phi}^{(n)}$ are the unknown amplitude and phase factors associated with the nth ray contribution. We wish to identify the rays that originate from edges 1 and 4, and corners 1, 2 and 4. Once these contributions are eliminated, the result is expected to be in close agreement with the current density induced on a semi-infinite quarter plane. Notice from (4.17) that $P_{r,\phi}^{(n)}$ represents the $\hat{r}$ component of the propagation vector of the nth ray. For a given direction of incidence, when the sampling direction $\hat{r}$ is chosen such that $P_{r,\phi}^{(n)}$ is positive only for the rays associated with edges 2 and 3, and corner 3, the extraneous contributions can be identified by their phase factors for a broad range of incidence directions. The unknowns $C_{r,\phi}^{(n)}$, $P_{r,\phi}^{(n)}$ and the number of rays can be obtained by using the MPM.

The MPM is a spectral estimation method that can be used to predict the parameters of a sum of complex exponentials in the form of (4.17). In general, the MPM can be applied effectively to estimate 1-D spectral frequencies as in [37]. Asymptotic Phasefront Extraction method (APE) [51] and extensions of MPM such as Matrix Enhancement-Matrix Pencil method (MEMP) [52] can be used for 2-D spectral frequency estimation. Compared to the 2-D estimation methods, it is observed that the MPM provides sufficient accuracy with much less complexity for the scattering configurations considered in this chapter. Application of the MPM is briefly summarized in the following.

It follows from (4.17) that along a given radial cut, the r and ϕ components of the current at the mth sampling point can be expressed as

$$J_{r,\phi}^{MoM}(\phi, r_m) = \sum_{n=1}^{N} C_{r,\phi}^{(n)}(\phi) z_n^m, \quad m = 1, ..., M \qquad (4.18)$$

70

where $z_n = e^{-jP_{r,\phi}^{(n)}(\phi)\hat{k}_n \cdot \hat{r}\Delta r}$. Using the sequence of MoM current samples along $\hat{r}$, two matrices are defined as

$$
\mathbf{J_1} = \begin{pmatrix} J_1 & J_2 & \cdots & J_P \\ J_2 & J_3 & \cdots & J_{P+1} \\ \vdots & \vdots & \ddots & \vdots \\ J_{M-P} & J_{M-P+1} & \cdots & J_{M-1} \end{pmatrix} \tag{4.19}
$$

$$
\mathbf{J_2} = \begin{pmatrix} J_2 & J_3 & \cdots & J_{P+1} \\ J_3 & J_4 & \cdots & J_{P+2} \\ \vdots & \vdots & \ddots & \vdots \\ J_{M-P+1} & J_{M-P+2} & \cdots & J_M \end{pmatrix}. \tag{4.20}
$$

Each row of $\mathbf{J_1}$ and $\mathbf{J_2}$ is constructed by windowing the sequence of J^{MoM} with the window length P, the pencil parameter. In order to find the phase factor $P_{r,\phi}^{(n)}$, the generalized eigenvalue equation for the matrix pencil $(\mathbf{J_2} - z_n\mathbf{J_1})$ is considered:

$$
\mathbf{J_2}\bar{e}_n = z_n\mathbf{J_1}\bar{e}_n \tag{4.21}
$$

where $\bar{e}_n$ is defined to be an eigenvector of the pencil. $\mathbf{J_1}$ can be decomposed into its singular components as

$$
\mathbf{J_1} = \mathbf{U\Sigma V^H} \tag{4.22}
$$

where the left and right singular unitary matrices $\mathbf{U}$ and $\mathbf{V^H}$ are $(M - P) \times (M - P)$ and $P \times P$ respectively. The superscript $\mathbf{H}$ denotes conjugate transpose. $\mathbf{\Sigma}$ is a $(M - P) \times P$ diagonal matrix with singular values of $\mathbf{J_1}$ on its diagonal elements. The number of modes, N, is easily determined by the number of significant singular values. For the scattering configurations considered in this chapter, the singular values become negligibly small after the first N diagonal elements in $\mathbf{\Sigma}$. Consequently, only the first N columns of $\mathbf{U}$ and $\mathbf{V^H}$ are preserved in (4.22), together with the first N singular values in $\mathbf{\Sigma}$. It follows from (4.21) and (4.22) that,

$$
\mathbf{\Sigma^{-1}U^H J_2 V V^H}\bar{e}_n = z_n\mathbf{V^H}\bar{e}_n. \tag{4.23}
$$

71

Therefore, z_n are simply the eigenvalues of the $N \times N$ matrix $\mathbf{\Sigma}^{-1}\mathbf{U}^{\mathbf{H}}\mathbf{J_2}\mathbf{V}$. Once z_n are determined, the amplitude factors C_n can be obtained by substituting z_n in (4.18) and solving the resulting overdetermined linear system of equations using linear least-squares fitting.

4.5   Numerical Examples

First, we consider the current density induced on the quarter plane depicted in Fig. 4.9(a). The quarter plane is illuminated by a $\hat{\theta}_i$ polarized plane wave incident from the direction $(\theta_i, \phi_i) = (45°, 225°)$. The current density is obtained by employing the MoM over a square region of width 4λ defined by the edges $\hat{e}_1$ and $\hat{e}_4$. The amplitude of $\bar{J}_r$ and $\bar{J}_\phi$ normalized with respect to the Physical Optics (PO) current density $(\bar{J}_{PO})$ for the same incidence direction along the radial cut $\phi = 0.5°$ is shown in Fig. 4.10. The current distribution labeled "RWG" represents the solution obtained using the regular RWG basis functions. "RWG-singular" denotes the current density obtained using the singular RWG basis functions presented in [28].
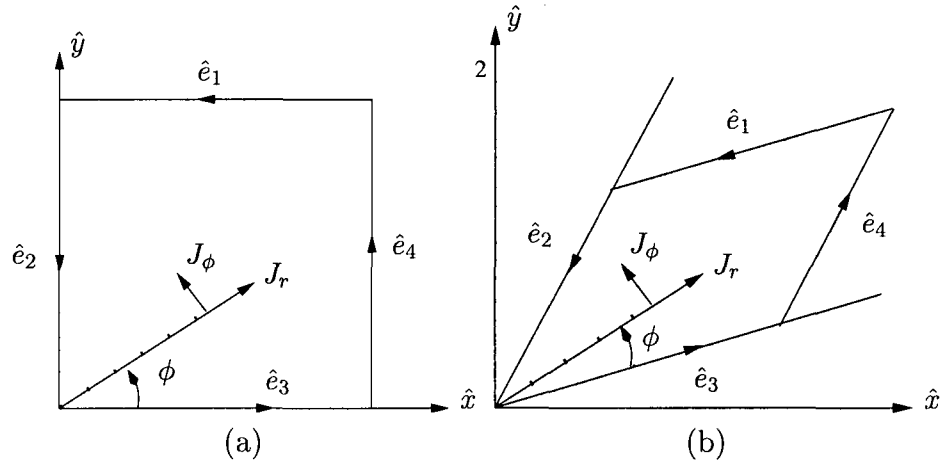
Figure 4.9: The radial cuts along which the current density is plotted in the numerical examples. (a) Quarter plane. (b) 60° angular sector. $\hat{e}_2$ and $\hat{e}_3$ are the two edges of the plane angular sector. $\hat{e}_1$ and $\hat{e}_4$ define the MoM region.

"First order singular" is the current distribution obtained using the edge and corner basis functions developed in this chapter. For the edge basis functions, a knife-edge singularity ($\nu = 0.5$) is used. The behavior of the corner basis functions for a 90° plane angular sector is described by $\tau = 0.298$ [25]. The current density induced on the semi-infinite quarter plane is represented by the curve "exact." The small discontinuities in the current distributions obtained using the MoM are due to the surface discretization. Both r and ϕ current components of the first order solution that employs the corner basis functions as well as singular edge basis functions agree well with the exact solution close to the corner. It is noted that, for the incidence direction considered in this example, the contributions due to truncations (edge 1 and edge 4 in Fig. 4.9(a)) are negligibly small close to the corner of the quarter plane. Hence, the MoM current must be in agreement with the exact quarter plane current for small values of r. The r component of the RWG-singular current agrees fairly well with the first-order-singular current except when the observation point is near the corner. The RWG-singular current tends to become singular at the corner due to singular basis functions used at the corner triangles. Away from the corner, both sets of basis functions produce a more accurate distribution for J_r as compared to the RWG basis functions. However, the RWG-singular basis functions do not provide any improvement over the RWG current distribution for the ϕ component. Along the radial cut $\phi = 0.5°$, J_ϕ represents roughly the component of the current density perpendicular to the edge. Because of the lack of extra independent degrees of freedom in the RWG-singular basis functions, the behavior of the perpendicular component cannot be modeled adequately. In order to improve the accuracy of the RWG basis functions, it is customary to use smaller triangles adjacent to the boundary edges. In this example, the nominal mesh size in the RWG solution is chosen to be $\lambda/10$ for the inner triangles and $\lambda/30$ for the edge triangles. For the RWG-singular and first-order-singular solutions, the surface is uniformly meshed with triangles of nominal
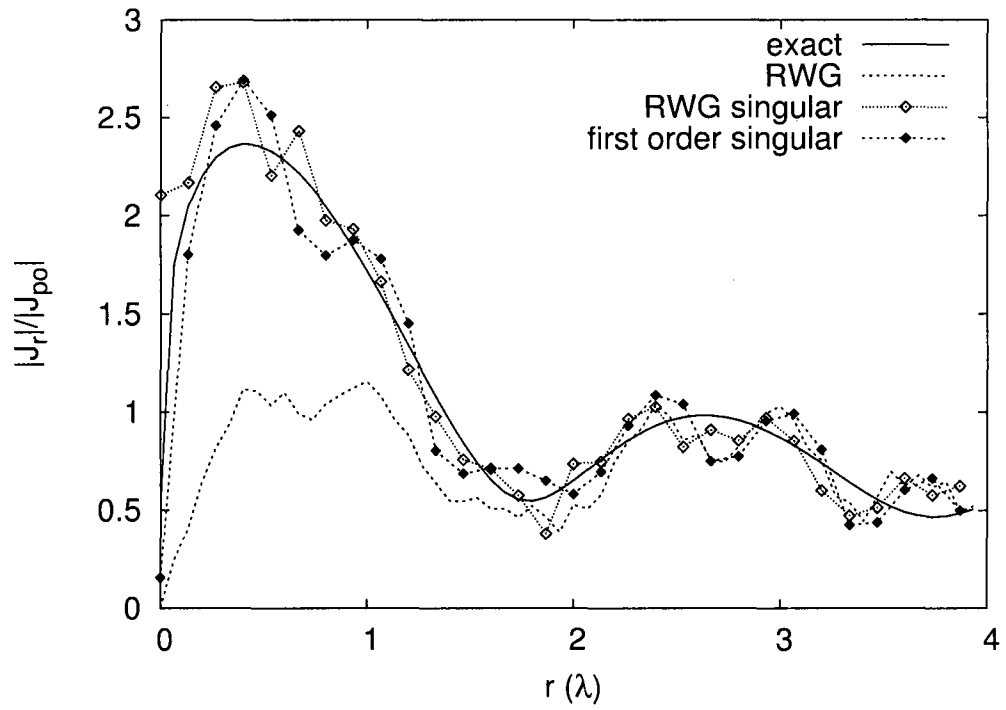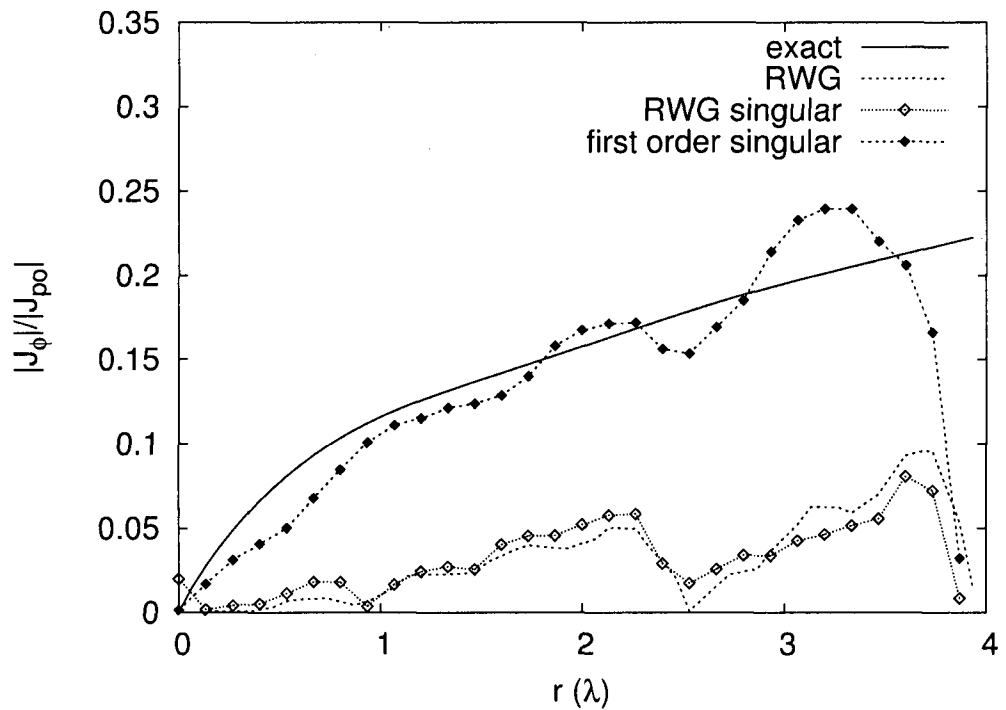
Figure 4.10: (a) J_r and (b) J_ϕ components of the surface current density on a square plate of width 4λ. The current density is calculated along the radial cut $\phi = 0.5°$ for a $\hat{\theta}_i$ polarized plane wave incident from the direction $(\theta_i, \phi_i) = (45°, 225°)$.

size $\lambda/7$.

Far from the corner, the standing wave behavior of the current density obtained using the MoM is associated with the contributions due to truncations. These contributions are eliminated from the MoM current using the MPM. Fig. 4.11 shows the extracted first-order-singular current distribution for various radial cuts. The MPM is applied directly to the MoM current density obtained using the first-order-singular basis functions. Very good agreement was obtained between the first-order-singular and the exact current distributions even along radial cuts in the immediate vicinity of the edge (i.e., $\phi = 0.05°$). The first-order-singular basis functions employ both the corner basis functions and the singular edge basis functions. In general, the inclusion of the corner basis functions causes a drastic change in the total current density, but only within about 0.1λ of the corner. Away from the corner the contribution is minor. It was found that if the corner basis function is excluded, then the first-order-singular current density behavior is very similar (but not identical) to the RWG-singular current in Fig. 4.10(a). Without the corner basis functions, the first-order-singular basis functions always lead to singular currents at the corners. In this case, the MPM cannot extract the currents properly. Thus the corner basis functions must be included in order to be able to extract the currents accurately. In addition, it is noted that the small oscillations seen in J_ϕ of Fig. 4.11(b) are due to the MoM's small current discontinuities processed by the MPM. (J_r has similar discontinuities, but because J_r is stronger near the edges MPM performs a better extraction.)

Fig. 4.12 shows the extracted first-order-singular current density on a 60° plane angular sector illuminated by a $\hat{\theta}_i$ polarized plane wave incident from the direction $(\theta_i, \phi_i) = (45°, 225°)$. In this example, the MoM is applied over a quadrilateral region of side length 3λ at the vertex of the angular sector as depicted in Fig. 4.9(b). $\tau = 0.24$ for a 60° angular sector. Notice from Fig. 4.12 that the range of observation points along radial cuts extends beyond the MoM region. The unknown coefficients in

(4.18) are obtained using the MoM current that is calculated over the quadrilateral region only. We have deliberately chosen the MoM region small enough to show that, once extraneous contributions are eliminated, the amplitude and phase factors of the remaining rays can be used to calculate the current density at observation points outside the MoM region. The first-order-singular current agrees fairly well with the exact current for the whole range of observation points. This verifies that the extracted first-order-singular current density is indeed a good approximation to the actual current density induced on the angular sector. In order to further demonstrate the accuracy of the first-order-singular basis functions, we calculate the relative error in the current density defined by

$$
e(\phi) = \frac{\left[\sum\limits_{m=1}^{M} |\bar{J}^e(\bar{r}_m, \phi) - \bar{J}^{MoM}(\bar{r}_m, \phi)|^2\right]^{\frac{1}{2}}}{\left[\sum\limits_{m=1}^{M} |\bar{J}^e(\bar{r}_m, \phi)|^2\right]^{\frac{1}{2}}} \tag{4.24}
$$

where $\mathbf{J^e}$ and $\mathbf{J^{MoM}}$ represent the current density obtained using the exact solution and the MoM respectively. M denotes the number of current density samples. The scattering configuration considered in the first example is solved using regular RWG and first-order-singular basis functions for various mesh sizes. Fig. 4.13 shows the relative error in J_r along various radial cuts as a function of the number of unknowns in the MoM solution. The error in RWG basis functions increases considerably as the edge is approached. It is noted that increasing the number of unknowns does not improve the RWG solution along the radial cuts that are close to the edge, $\phi = 0.05°$ and $\phi = 0.5°$. For any given number of unknowns, the first-order-singular basis functions are much more accurate compared to the RWG basis functions. The slope of the error curve serves as a measure of the order of convergence of the numerical solution. The error in first-order-singular current density decreases at a faster rate as compared to the error in RWG current density. Note that, especially for small number of unknowns, the rate of decrease in the error for the first-order-singular solution is

76
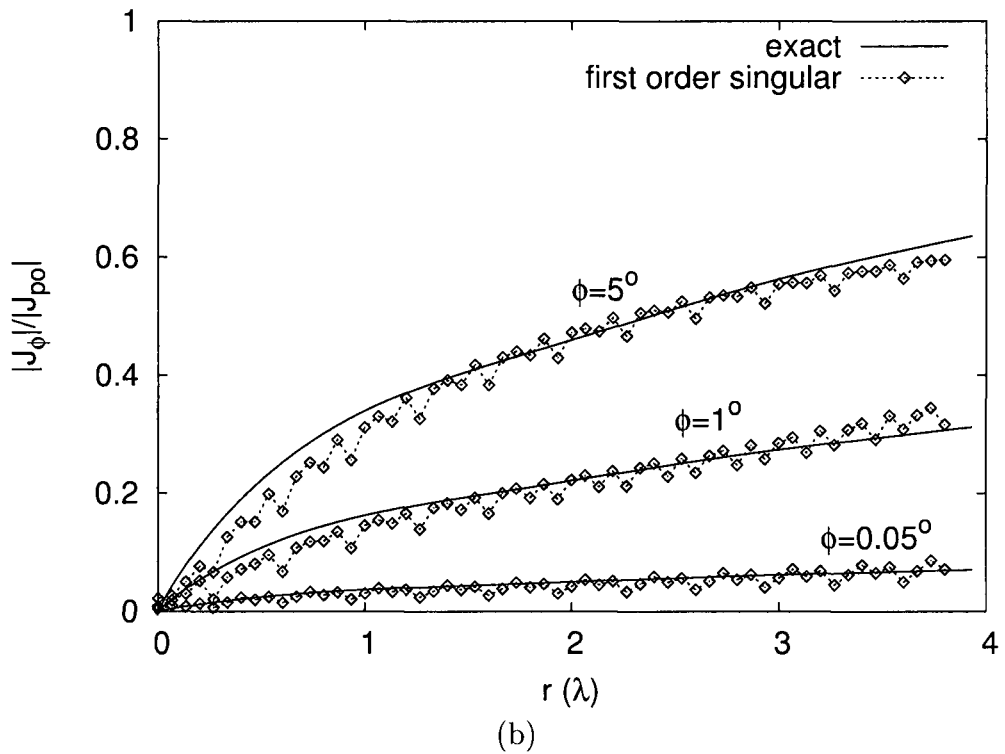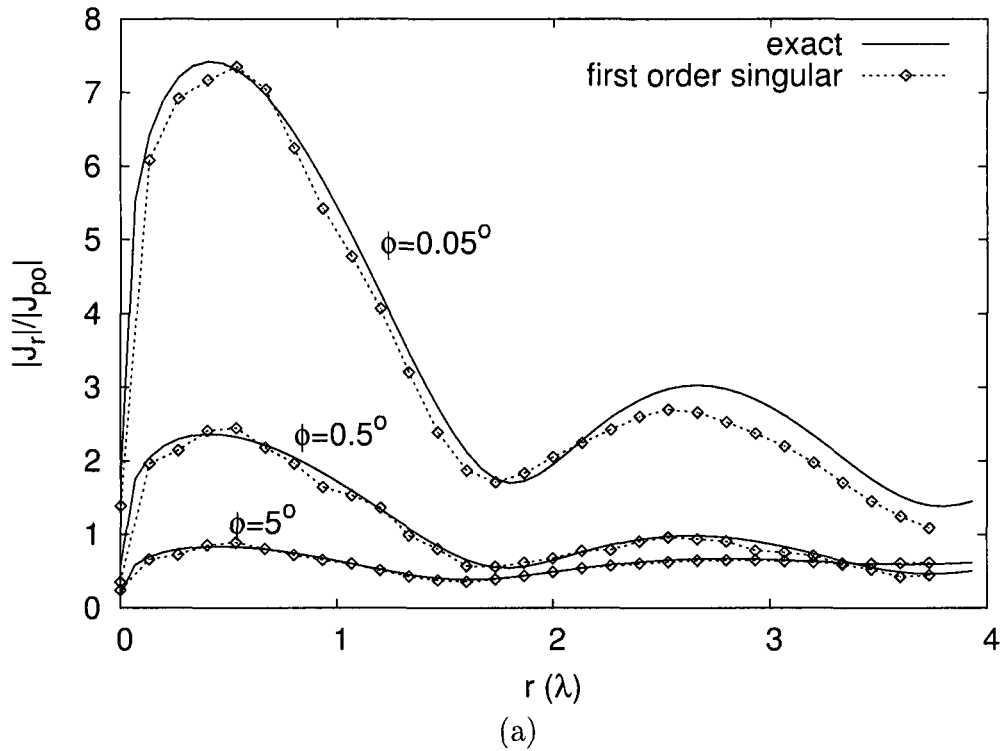
Figure 4.11: (a) J_r and (b) J_ϕ components of the surface current density on a quarter plane for various radial cuts near the edge for a $\hat{\theta}_i$ polarized plane wave incident from the direction $(\theta_i, \phi_i) = (45°, 225°)$.

77

much higher than the RWG solution. Similar improvement was observed in the error in J_ϕ. Since J_ϕ is very small near the edges, the error in total current is also very similar to the results presented in Fig. 4.13.
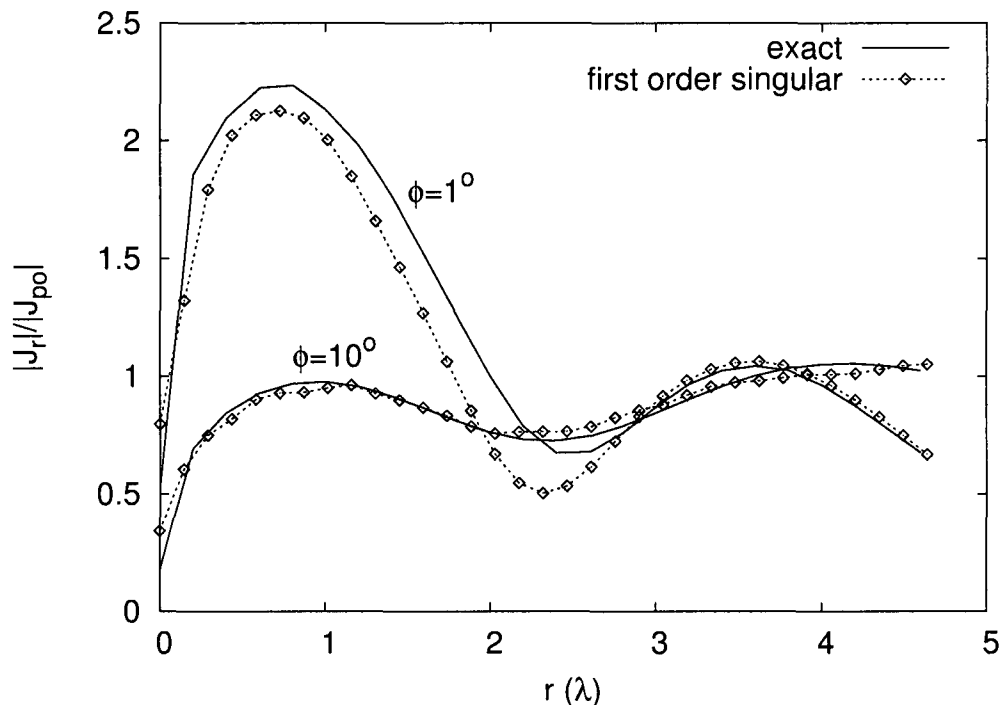
Figure 4.12: Radial component of the surface current density along the radial cuts $\phi = 1°$ and $\phi = 10°$ on a plane angular sector. The tip angle of the plane angular sector is 60°. The incident field field is $\hat{\theta}_i$ polarized and $(\theta_i, \phi_i) = (45°, 225°)$. The MoM is applied over a quadrilateral region of side length 3λ around the corner of the angular sector as depicted in Fig. 4.9(b).

Finally, in order to investigate the effect of the use of singular and corner basis functions on the Radar Cross Section (RCS) pattern, we consider the problem of scattering from a square plate of width 4λ of Fig. 4.8 illuminated by a plane wave incident from the direction $(\theta_i, \phi_i) = (80°, 45°)$. The mesh sizes are chosen to be $\lambda/10$ for RWG and $\lambda/7$ for first-order-singular basis functions. This leads to approximately the same number of unknowns for the two cases. Fig. 4.14 shows the bistatic RCS pattern $(RCS_{\theta\theta})$ of the plate calculated in the y-z plane. The pattern obtained using

78
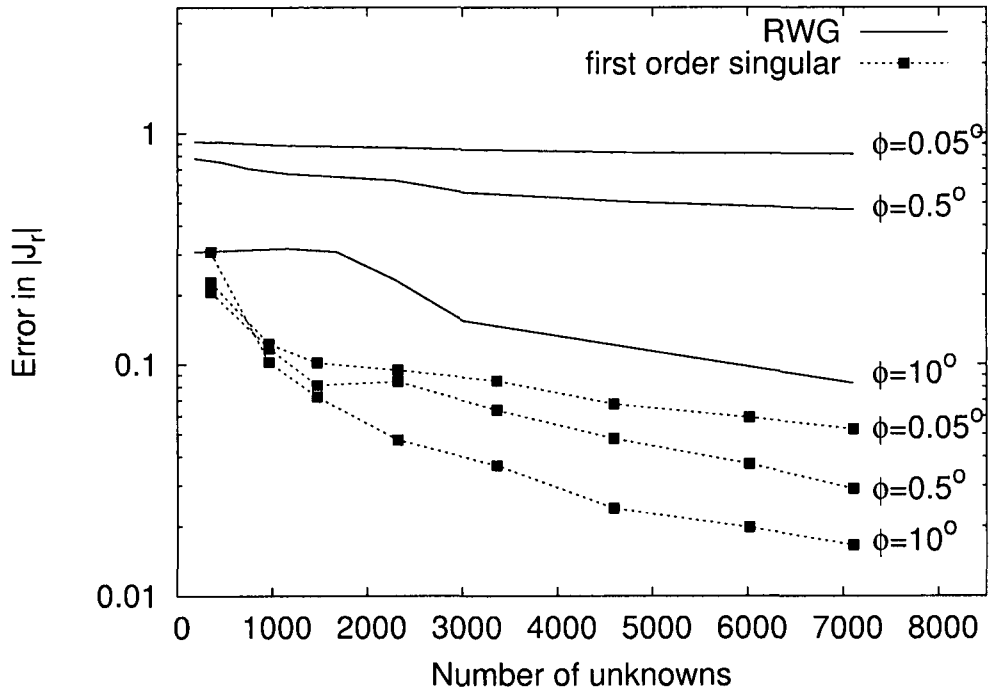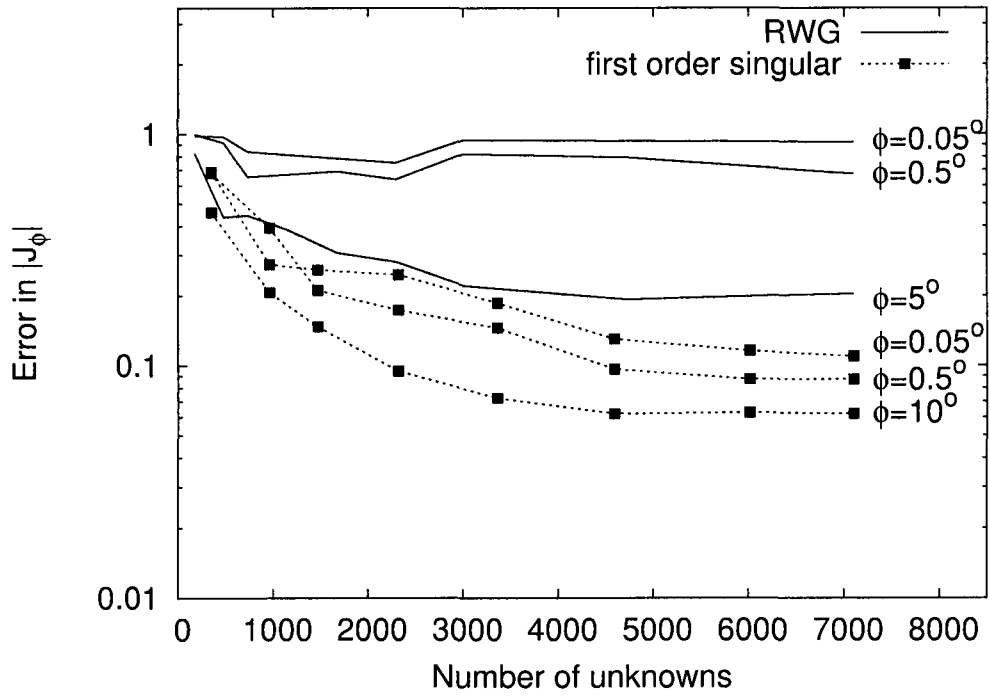
Figure 4.13: Relative error in the (a) $\hat{r}$ and (b)$\hat{\phi}$ components of the surface current density along various radial cuts as a function of the total number of unknowns used in the MoM solution. The incident field is $\hat{\theta}_i$ polarized and $(\theta_i, \phi_i) = (45°, 225°)$.

79
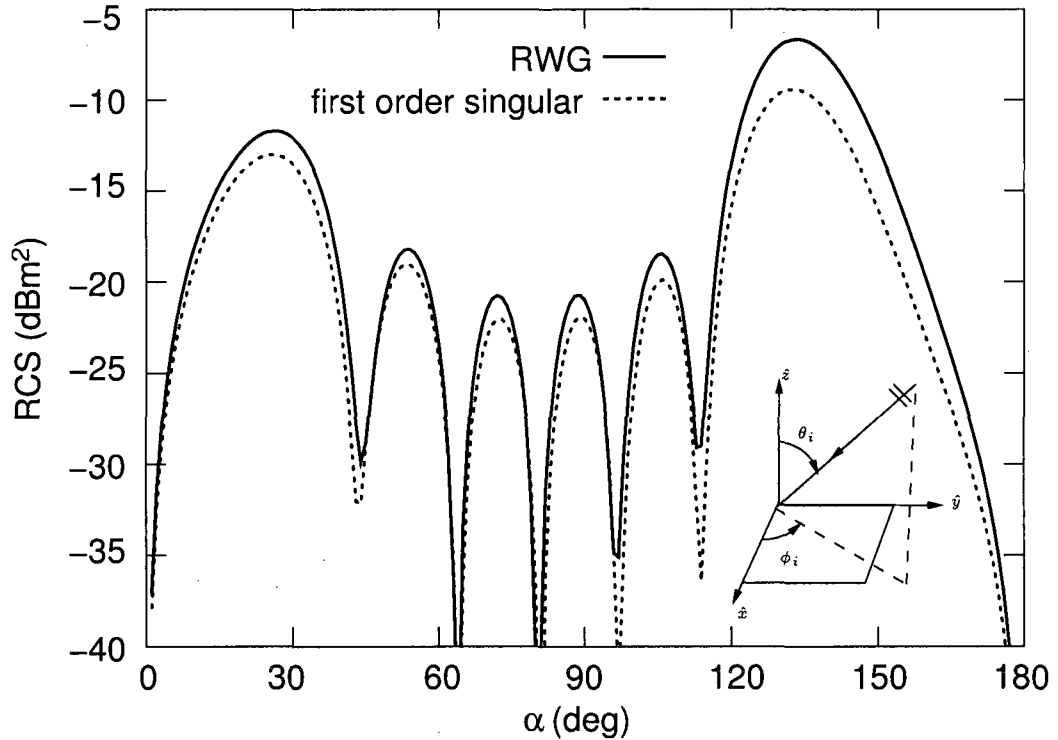
Figure 4.14: Bistatic RCS of a 4λ square plate for $(\theta_i, \phi_i) = (80°, 45°)$. The RCS pattern is calculated on the y-z plane. α is measured from the positive y-axis.

the first-order-singular basis functions differ from the RWG pattern over the entire range of observation directions. The difference is as high as 4 dB around the main lobe. It is demonstrated by the previous numerical examples that first-order-singular basis functions provide a more accurate current density as compared to regular RWG basis functions. Therefore, the RCS pattern obtained using the first-order-singular basis functions must be more accurate. It was observed that using smaller triangles near the edges in the RWG solution does not lead to any substantial change in the RCS pattern. We solved the same problem using regular RWG basis functions with a 0.01λ mesh size within 0.1λ of the edge. It was observed that the RCS values decreased by less than 0.5 dB in the main lobe region. It was not possible to further improve the result by using even smaller triangles near the edges. As suggested by the error analysis
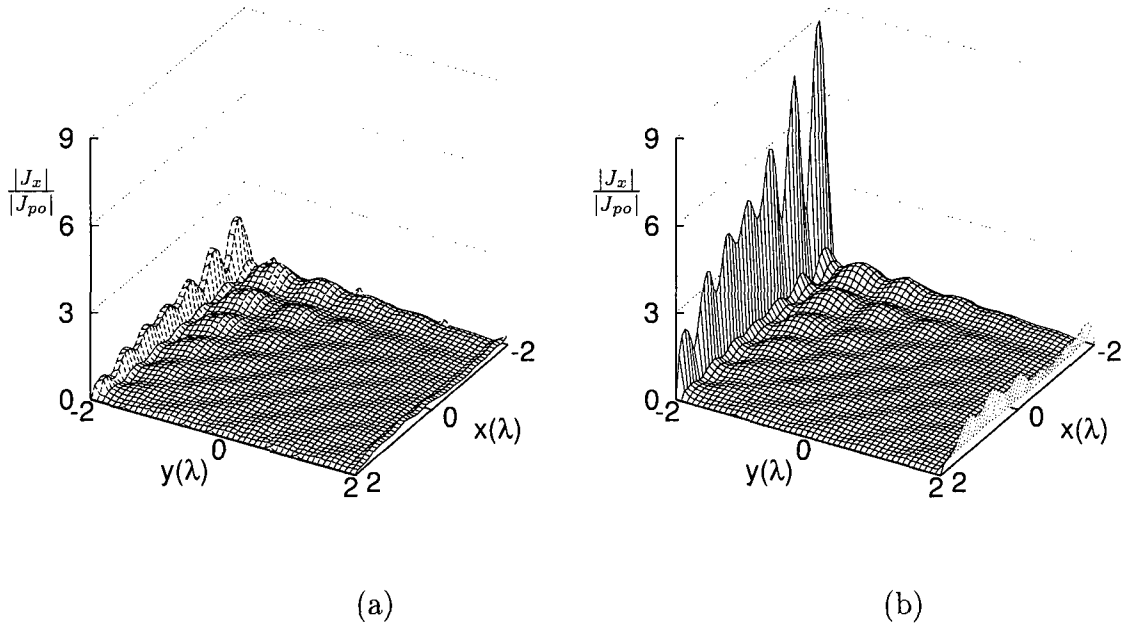
Figure 4.15: $\hat{x}$ component of the surface current density on a 4λ square plate for $(\theta_i, \phi_i) = (80°, 45°)$. (a) RWG, (b) First-order singular basis functions.

in Fig. 4.13, the accuracy of the RWG results cannot be increased simply by using smaller triangles near the edges. It is noted that the observation directions in this example are far off the specular and it is a difficult test case which is sensitive to small errors in the current. We compared the RCS patterns obtained using the first-order-singular basis functions with RWG patterns for several scattering configurations. In general, the RWG and the first-order-singular basis functions produce similar RCS values near the specular directions. However, far from the specular directions, the disagreement between the two methods can be 3 or 4 dB as illustrated in Fig. 4.14. The $\hat{x}$ component of the surface current density on the 4λ square plate normalized with respect to the PO current level is shown in Fig. 4.15. It is observed that, the current density obtained using the first-order singular basis functions is significantly different from the RWG current density near the edges along $\hat{x}$. Fig. 4.16 shows the

RCS pattern ($RCS_{\phi\phi}$) of the triangular plate of Fig. 3.11(a) illuminated by a plane wave incident from the direction $(\theta_i, \phi_i) = (45°, 178°)$. The incident field is polarized in the $\hat{\phi}_i$ direction. It is observed that, the singular-basis function pattern differs from the RWG pattern by as much as 4 dB around the main lobe. It should be noted that the level of the total scattered field is low in this plane of observation. Thus the RCS is very sensitive to changes in the current density. The $\hat{x}$ and $\hat{y}$ components of the difference in the surface current density obtained by subtracting the RWG current density from the first-order-singular current density is shown in Fig. 4.17. It is evident that the difference in the RCS patterns is caused by the difference in the surface current density which is significant near the edges for both components.
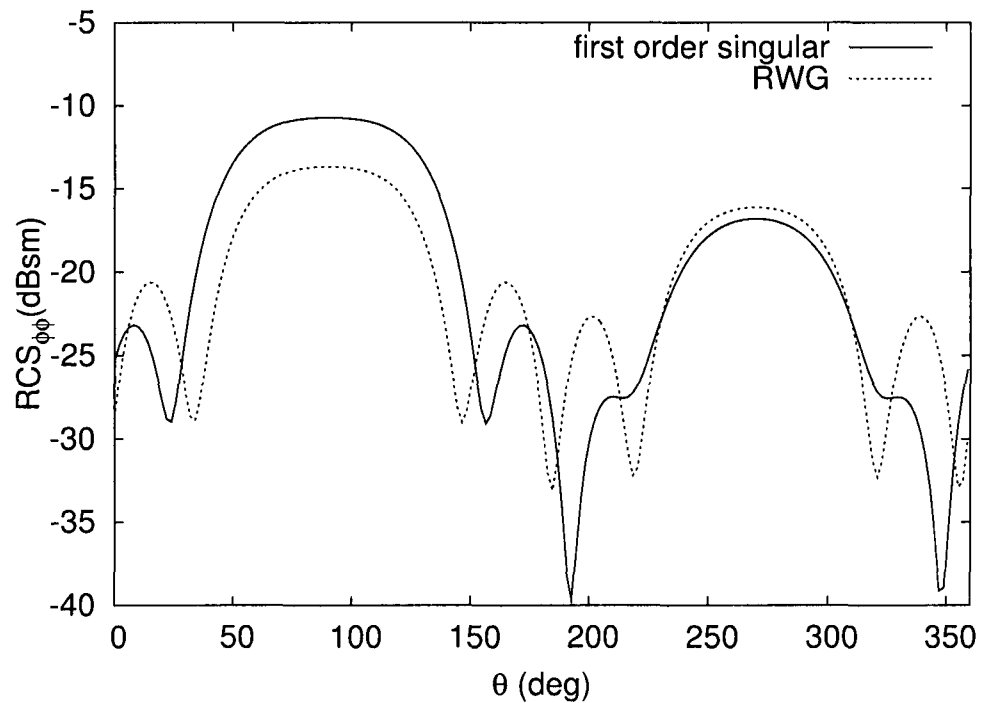
Figure 4.16: Bistatic RCS of a triangular plate for $(\theta_i, \phi_i) = (45°, 178°)$. $h = 3\lambda$, $\alpha_d = 30°$. $RCS_{\phi\phi}$ is calculated on the y-z plane.
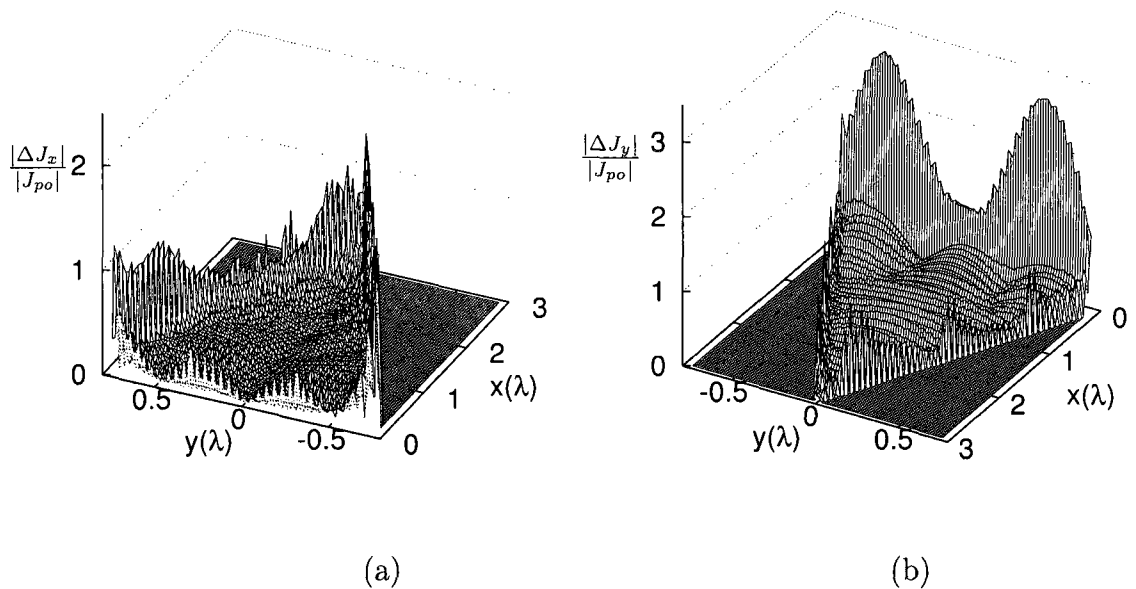
Figure 4.17: (a) $\hat{y}$ and (b) $\hat{x}$ components of the difference in the surface current density on the triangular plate of Fig. 3.11(a) for $(\theta_i, \phi_i) = (45°, 178°)$. The incident field is $\hat{\phi}_i$ polarized. The height of the triangle h is 3λ. $|J_{po}| = 0.00375$ A$/\lambda$.

4.6 Conclusion

In this chapter, a new set of first-order-singular basis functions has been developed based on the first-order RWG functions. It has been demonstrated that the first-order-singular basis functions are capable of modeling both the parallel and the perpendicular component of the current near the edges. The accuracy of the results have been validated by comparisons with the current density obtained using the exact solution on a semi-infinite plane angular sector.

The behavior of the current density in the vicinity of the edge and the corner of a plane angular sector has also been investigated. When singular basis functions are used over all of the boundary patches, the current density at the corner, where two half planes meet, becomes singular too. However, as demonstrated by the numerical

examples, depending on the polarization of the incident field, the corner behavior of the current density is different than its edge behavior. To avoid the unwanted singularity at the corners, corner basis functions to be used only at the patches adjacent to the corners were developed. It was illustrated that the use of first-order-singular basis functions affects the RCS pattern over the low-level regions. It should be noted that the far-field pattern becomes more sensitive to the small errors in the current density as the level of the scattered field decreases. As a consequence the difference between the RCS patterns obtained using the regular RWG basis functions and the first-order singular basis functions increase as the observation point moves away from the specular directions.

Chapter 5

Conclusion

In this thesis, the problem of electromagnetic scattering from a perfectly conducting plane angular sector has been investigated. In the framework of high-frequency techniques, the total current induced on the surface of a scatterer is expressed as the sum of the contributions from localized diffraction centers. For the plane angular sector, the current can be expressed as the sum of the diffracted currents from the edges, and the vertex-diffracted currents. The edge-diffracted currents can be calculated using the well known PTD formulation. The purpose of this thesis was to formulate the vertex-diffracted currents and investigate the effect of vertex diffraction phenomena in RCS calculations. The presence of sharp edges and corners on a scattering body leads to singularities in fields and current density. In a numerical solution, these singularities must be modeled properly for improved accuracy. Towards this goal, we have also developed a new set of singular basis functions. The main contributions of this thesis can be summarized as follows:

- The exact solution of the problem of electromagnetic scattering from a plane angular sector was refined and practical guidelines for the numerical solution of the eigenvalue problem have been presented. It is noted that when the

continued fractions method is used, the eigenvalue pairs become inaccurate as the number of terms in the eigenfunction expansion increases. As a consequence, this method provides accurate results only within around 1.5λ of the vertex. Unlike the continued fractions method, the proposed approach provides accurate results even for observation points far away from the corner.

- Vertex diffraction coefficients for the current density induced on the surface of plane angular sector have been formulated. Unlike the previous developments, the formulation for the vertex-diffracted current density is valid for arbitrary directions of incidence. Thus, it is the first time that the the vertex-diffracted currents have been used together with high-frequency techniques such as the PTD to calculate the RCS pattern of a finite scatterer for arbitrary angles of incidence.

- A new set of basis functions that can accurately model the current density in the vicinity of the edges and corners of a polygonal structure has been developed.

In Chapter 3, numerical diffraction coefficients for vertex-diffracted edge waves were derived. The current density on the surface of the plane angular sector was modeled using the PTD. The vertex-diffracted currents were then defined as the difference between the exact and PTD currents. Based on the known physical behavior of the vertex-diffracted currents, the difference current was modeled as a wave traveling away from the corner. The unknown coefficients for the vertex-diffracted currents were obtained by applying least squares fit approximation to the difference current. In many practical situations, multiple edge diffractions play an important role in calculating the current density on a polygonal flat plate. Thus, in order to be able to identify the vertex-diffracted currents in an accurate manner for arbitrary directions of incidence, it is important to eliminate the higher order edge effects from the total

current. Up to second-order edge-diffracted currents were incorporated in our derivations. Unlike the previous developments, we were able to extract the vertex-diffracted currents even for a narrow plane angular sector. The vertex-diffracted currents have been validated by direct comparisons with the exact solution on the plane angular sector.

The term "corner diffraction" is often used in the literature to describe the effect of the truncation of the edge diffracted currents at the tip of the plane angular sector. This truncation effect serves as a correction to the vertex-diffracted fields arising from the asymptotic evaluation of the PO-based surface integral on the plane angular sector. In the present development, vertex-diffracted currents also include the effect of the vertex-excited edge waves. Since the vertex-diffracted currents are numerically derived, in the RCS calculations it is necessary to solve the problem of diffraction from a semi-infinite plane angular sector for the given direction of incidence and polarization. However, calculation of the exact current is computationally intensive, and this requires additional CPU time especially for monostatic RCS calculations. In order to decrease the computational requirement as much as possible, we chose the maximum range of the radial cut over which the difference current is sampled to be as small as possible in deriving the vertex-diffracted currents. Furthermore, we pre-processed the scattering structure for monostatic RCS calculations to tabulate the corner diffraction coefficients as a function of all the possible incidence directions and observation points on the surface of the scatterer. Once the unknown coefficients were tabulated, they were used directly in the RCS computation to find the vertex-diffracted currents from a pertinent corner on the finite scatterer. We have demonstrated using 3-D scattering problems that the vertex-diffracted currents provide a remarkable improvement in the accuracy of RCS patterns in the low-level regions. The accuracy could further be improved by incorporating the higher order diffraction mechanisms in the solution.

The numerical diffraction coefficients developed in this thesis can be used to model the vertex diffraction from the tip of a plane angular sector of arbitrary vertex angle for arbitrary excitation parameters (incidence direction and polarization). This can be accomplished by tabulating the diffraction coefficients for every possible excitation parameter and vertex angle. Since this procedure requires a long pre-processing time, the practicality of the numerical diffraction coefficients is questionable. The future research efforts should focus on obtaining a functional representation of the numerical diffraction coefficients with respect to the excitation parameters to derive UTD-like analytical expressions for vertex-diffraction coefficients. Another area for future research is the investigation of diffraction coefficients for the tip of a pyramidal structure. The approach used in this thesis can be extended to treat this problem. It should be noted that the total current density excited on the surface of the plane angular sector can be calculated by using the exact eigenfunction expansion which is readily available. Consequently, the current density associated with vertex-diffraction can be identified by subtracting all the other contributions from the total current. Thus, to be able to use the same method, the total current density near the tip of the pyramidal structure should be calculated. A promising approach is to use MoM for this purpose. This approach was previously used for the plane angular sector problem [18]. The resulting expressions for the vertex-diffraction coefficients can only be applied for a very limited angular region of incidence directions. The same approach can be used for the tip of a pyramidal geometry. However, extending the applicability of the diffraction coefficients to arbitrary angles of incidence remains a challenging problem.

In Chapter 4, a new set of first-order-singular basis functions has been developed based on the first-order RWG functions. It has been demonstrated that the first-order-singular basis functions are capable of modeling both the parallel and the perpendicular component of the current near the edges. The accuracy of the results

have been validated by comparisons with the current density obtained using the exact solution on a semi-infinite plane angular sector.

The first-order-singular basis functions have been developed more for achieving an improved accuracy near the sharp edges and corners of a scatterer, rather than for improved convergence. However, since they are based on the first-order RWG basis functions, the new basis functions converge faster than the nonsingular RWG functions. The use of corner and edge singularities also improves the convergence by decreasing the number of unknowns. Since the first-order-singular basis functions can adequately model the current near the edges and corners, it is desirable to mesh the surface such that the triangles adjacent to the edges and corners are as large as possible, leading to fewer triangles to be used in the MoM solution. It was demonstrated that the size of the edge and corner triangles are limited by the accuracy of basis functions. The behavior of the current density near the edges and corners are described by d^ν and ρ^τ. It is noted that these are only first order approximations to the actual behavior of the current density as demonstrated in Chapter 4. Furthermore, in general the values of ν and τ do not depend only on the geometry. Different values of ν and τ may be needed as the polarization and direction of the incident field is changed. Hence the new basis functions are considered to be only first order complete to represent the current density. As a consequence, the triangles adjacent to the edges and corners must be small enough to ensure that the singularity approximation is valid. For instance, $1/\sqrt{d}$ behavior for the parallel component of the current density is valid only for $d < \lambda/10$. Consequently, the size of the edge triangle cannot exceed $\lambda/10$. In order to further improve the convergence and accuracy, higher order behavior of the current density should be included in the basis functions as discussed in [53]. Even though the first-order-singular basis functions developed in this thesis are not highest order complete, it was illustrated with 3-D scattering problems that they provide substantial improvement in the accuracy without incurring too much

complexity in the analysis or additional computational burden.

Bibliography

[1] R. Satterwhite and R. G. Kouyoumjian, "Electromagnetic diffraction by a perfectly conducting plane angular sector," ElectroSci. Lab. Ohio State Univ., Columbus, Tech. Rep. 2183-2, 1970.

[2] T. B. Hansen, "Diffraction by a plane angular sector, a new derivation," *IEEE Trans. Antennas Propagat.*, vol. AP-38, no. 11, pp. 1892–1894, 1990.

[3] R. Satterwhite, "Diffraction by a quarter plane, the exact solution and some numerical results," *IEEE Trans. Antennas Propagat.*, vol. AP-22, pp. 500–503, May 1974.

[4] J. N. Sahalos and G. A. Thiele, "The eigenfunction solution for scattered fields and surface wave currents of a vertex," *IEEE Trans. Antennas Propagat.*, vol. AP-31, no. 1, pp. 206–211, 1983.

[5] S. Blume and U. Uschkerat, "The radar cross section of the semi-infinite elliptic cone: numerical evaluation," *Wave Motion*, vol. 22, pp. 311–324, 1995.

[6] S. Blume and V. Krebs, "Numerical evaluation of dyadic diffraction coefficients and bistatic radar cross sections for a perfectly conducting semi-infinite elliptic cone," *IEEE Trans. Antennas Propagat.*, vol. 46, no. 3, pp. 414–424, 1998.

[7] V. M. Babich, V. P. Smyshlyaev, D. B. Dement'ev, and B. A. Samokish, "Numerical calculation of the diffraction coefficients for an arbitrary shaped perfectly

conducting cone," *IEEE Trans. Antennas Propagat.*, vol. 44, no. 5, pp. 740–747, 1996.

[8] V. P. Smyshlyaev, "Diffraction by conical surfaces at high frequencies," *Wave Motion*, vol. 12, pp. 329–339, 1990.

[9] P. Y. Ufimtsev, *Fundamentals of the Physical Theory of Diffraction.* New Jersey: John Wiley & Sons Inc., 2007.

[10] P. H. Pathak and W. D. Burnside, "A uniform GTD for the diffraction by edges, vertices and convex surfaces," in *Theoretical methods for determining the interaction of electromagnetic waves with structures*, J. K. Skwirzynski, Ed. Sijthoff and Noordhoff, 1981, pp. 497–561.

[11] F. A. Sikta, W. D. Burnside, T. T. Chu, and J. L. Peters, "First-order equivalent current and corner diffraction scattering from flat plate structures," *IEEE Trans. Antennas Propagat.*, vol. AP-31, no. 4, pp. 584–589, 1983.

[12] A. Michaeli, "Comments on "First-order equivalent current and corner diffraction scattering from flat plate structures"," *IEEE Trans. Antennas Propagat.*, vol. AP-32, no. 9, pp. 1011–1012, 1984.

[13] T. J. Brinkley and R. J. Marhefka, "Far-zone bistatic scattering from flat plates," ElectroSci. Lab. Ohio State Univ., Columbus, Tech. Rep. 718295-8, 1990.

[14] A. Michaeli, "Elimination of infinities in equivalent edge currents, part I: Fringe current components," *IEEE Trans. Antennas Propagat.*, vol. AP-34, no. 7, pp. 913–918, 1986.

[15] K. C. Hill, "A utd solution to the em scattering by the vertex of a plane angular sector," Ph.D. dissertation, The Ohio State University, 1990.

[16] K. C. Hill and P. H. Pathak, "A UTD solution for the EM diffraction by a corner in a plane angular sector," in *1991 International IEEE Transactions on Antennas and Propagation and National Radio Science Meeting*, London, Ontario, Canada, June 24-28 1991.

[17] S. Maci, M. Albani, and F. Capolino, "ITD formulation for the currents on a plane angular sector," *IEEE Trans. Antennas Propagat.*, vol. AP-46, no. 9, pp. 1318–1327, Sept. 1998.

[18] T. B. Hansen, "Corner diffraction coefficients for the quarter plane," *IEEE Trans. Antennas Propagat.*, vol. AP-39, no. 7, pp. 976–984, 1991.

[19] G. F. Herrman, "Numerical computation of diffraction coefficients," *IEEE Trans. Antennas Propagat.*, vol. AP-35, no. 1, pp. 53–61, 1987.

[20] G. F. Herrman and S. M. Strain, "Numerical diffraction coefficients in the shadow transition region," *IEEE Trans. Antennas Propagat.*, vol. AP-36, no. 9, pp. 1244–1251, 1988.

[21] M. P. Hurst, "Numerical diffraction coefficients for surface waves," *IEEE Trans. Antennas Propagat.*, vol. AP-41, no. 4, pp. 458–464, 1993.

[22] T. J. Brinkley, "Current near the vertex of a perfectly conducting angular sector," Ph.D. dissertation, The Ohio State University, 1990.

[23] O. Breinbjerg, "Higher order equivalent edge currents for fringe wave radar scattering by perfectly conducting polygonal plates," *IEEE Trans. Antennas Propagat.*, vol. AP-40, no. 12, pp. 1543–1554, 1992.

[24] G. L. James, *Geometrical Theory of Diffraction for Electromagnetic Waves.* England: Peter Peregrinus Ltd., 1976.

[25] J. Van Bladel, *Singular Electromagnetic Fields and Sources*. Piscataway, NJ: IEEE Press, 1991.

[26] D. R. Wilton and S. Govind, "Incorporation of edge conditions in moment method solutions," *IEEE Trans. Antennas Propagat.*, vol. AP-25, no. 6, pp. 845–850, Nov. 1977.

[27] J. H. Richmond, "On the edge mode in the theory of tm scattering by a strip or strip grating," *IEEE Trans. Antennas Propagat.*, vol. AP-28, no. 6, pp. 883–887, Nov. 1980.

[28] W. J. Brown and D. R. Wilton, "Singular basis functions and curvilinear triangles in the solution of the electric field integral equation," *IEEE Trans. Antennas Propagat.*, vol. AP-47, no. 2, pp. 347–353, 1999.

[29] T. Andersson, "Moment method calculations of scattering by a square plate using singular basis functions and multipole expansions," *J. Electro. Waves Appl.*, vol. 7, no. 1, pp. 93–121, 1993.

[30] R. D. Graglia and G. Lombardi, "Singular higher order complete vector bases for finite methods," *IEEE Trans. Antennas Propagat.*, vol. AP-52, no. 7, pp. 1672–1685, 2004.

[31] R. D. Graglia, D. R. Wilton, and A. F. Peterson, "Higher order interpolatory vector bases for computational electromagnetics," *IEEE Trans. Antennas Propagat.*, vol. AP-45, no. 3, pp. 329–342, 1997.

[32] B. M. Notaros, "Higher order frequency-domain computational electromagnetics," *IEEE Trans. Antennas Propagat.*, vol. AP-56, no. 8, pp. 2251–2276, 2008.

[33] J. Meixner, "The behavior of electromagnetic fields at edges," *IEEE Trans. Antennas Propagat.*, vol. AP-20, no. 7, pp. 442–446, July 1972.

[34] L. C. Trintinalia and H. Ling, "First order triangular patch basis functions for electromagnetic scattering," *J. Electro. Waves Appl.*, vol. 15, no. 11, pp. 1521–1537, 2001.

[35] S. M. Rao, D. R. Wilton, and A. W. Glisson, "Electromagnetic scattering by surfaces of arbitrary shape," *IEEE Trans. Antennas Propagat.*, vol. AP-30, no. 3, pp. 409–418, May 1982.

[36] Y. Hua and T. K. Sarkar, "Matrix pencil method for estimating parameters of exponentially damped/undamped sinusoid in noise," *IEEE Trans. Acoustic Speech Signal Processing*, vol. 38, pp. 834–844, May 1990.

[37] Z. Altman, R. Mittra, O. Hashimoto, and E. Michielssen, "Efficient representation of induced currents on large scatterers using the generalized pencil of function method," *IEEE Trans. Antennas Propagat.*, vol. AP-7, no. 1, pp. 51–57, 1996.

[38] L. Kraus and L. M. Levine, "Diffraction be an elliptic cone," *Communications on Pure and Applied Mathematics*, vol. XIV, pp. 49–68, 1961.

[39] C. T. Tai, *Dyadic Green's Functions in Electromagnetic Theory.* Scranton: Intext Educational Publishers, 1971.

[40] E. L. Ince, "The periodic lamé functions," *Proc. Roy. Soc. Edinburgh*, pp. 47–63, Sect. A 60 1940.

[41] J. K. M. Jansen, "Simple periodic and nonperiodic lamé functions and their application in the theory of conical waveguides," Ph.D. dissertation, Eindhoven Univ. Technol., Eindhoven, The Netherlands, 1976.

[42] W. H. Press, S. A. Teukolsky, W. T. Vetterling, and B. P. Flannery, *Numerical Recipes: The Art of Scientific Computing.* New York: Cambrige University Press, 2007.

[43] A. K. Ozturk, R. Paknys, and C. W. Trueman, "Vertex diffracted edge waves on a perfectly conducting plane angular sector," *IEEE Trans. Antennas Propagat.*, Submitted.

[44] F. B. Hildebrand, *Introduction to Numerical Analysis.* New York: McGraw-Hill, 1956.

[45] L. P. Ivrissimtzis and R. J. Marhefka, "A uniform ray approximation of the scattering by polyhedral structures including higher order terms," *IEEE Trans. Antennas Propagat.*, vol. AP-40, no. 11, pp. 1302–1312, Nov. 1992.

[46] ——, "Edge wave vertex and edge diffraction," *Radio Sci.*, vol. 24, no. 6, pp. 771–784, Nov.-Dec. 1989.

[47] O. C. Zienkiewicz, *The Finite Element Method in Engineering Science.* New York: McGraw-Hill, 1971.

[48] A. K. Ozturk, R. Paknys, and C. W. Trueman, "First order singular basis functions for corner diffraction analysis using the method of moments," *IEEE Trans. Antennas Propagat.*, vol. AP-57, no. 10, 2009.

[49] A. W. Glisson and D. R. Wilton, "Simple and efficient numerical methods for problems of electromagnetic radiation and scattering from surfaces," *IEEE Trans. Antennas Propagat.*, vol. AP-28, no. 5, pp. 593–603, 1980.

[50] J. R. Mautz and R. F. Harrington, "An E-field solution for a conducting surface small or comparable to the wavelength," *IEEE Trans. Antennas Propagat.*, vol. AP-32, no. 4, pp. 330–339, 1984.

[51] D. Kwon, R. J. Burkholder, and P. H. Pathak, "Efficient method of moments formulation for large pec scattering problems using asymptotic phasefront extraction (APE)," *IEEE Trans. Antennas Propagat.*, vol. AP-49, no. 4, pp. 583–591, 2001.

[52] Y. Hua, "Estimating two-dimensional frequencies by mathix enhancement and matrix pencil," *IEEE Trans. on Signal Processing*, vol. 40, pp. 2267–2280, Sept. 1992.

[53] M. M. Bibby, A. F. Peterson, and C. M. Coldwell, "High order representations for singular currents at corners," *IEEE Trans. Antennas Propagat.*, vol. 56, no. 8, pp. 2277–2287, 2008.

[54] D. R. Wilton, S. M. Rao, A. W. Glisson, D. H. Schaubert, O. M. Al-Bundak, and C. M. Butler, "Potential integrals for uniform and linear source distributions on polygonal and polyhedral domains," *IEEE Trans. Antennas Propagat.*, vol. AP-32, no. 3, pp. 276–281, Mar. 1984.

Appendix A

Sphero-conal Coordinate System

The vector wave equation has been solved in the uniformized sphero-conal coordinate system developed in [38]. The sphero-conal coordinates represented by (r, ϑ, φ) are related to the cartesian coordinates by

$$x_c = r \cos \vartheta \sqrt{1 - k'^2 \cos^2 \varphi} \tag{A-1}$$

$$y_c = r \sin \vartheta \sin \varphi \tag{A-2}$$

$$z_c = r \cos \varphi \sqrt{1 - k^2 \cos^2 \vartheta} \tag{A-3}$$

where r represents the distance from the origin and ϑ is measured from the x_c axis on the $x_c - y_c$ plane. Similarly, φ is measured from the z_c axis on the $z_c - y_c$ plane. k is the ellipticity parameter given by

$$k^2 = \cos^2 \frac{\alpha_d}{2}$$

and k' is defined as

$$k'^2 = 1 - k^2$$

where $0 \leq k \leq 1$, $0 \leq k' \leq 1$, $0 \leq \vartheta \leq \pi$ and $0 \leq \varphi \leq 2\pi$. The geometry of the coordinate surfaces are shown in Fig. A-1(a). The intersection of the surfaces
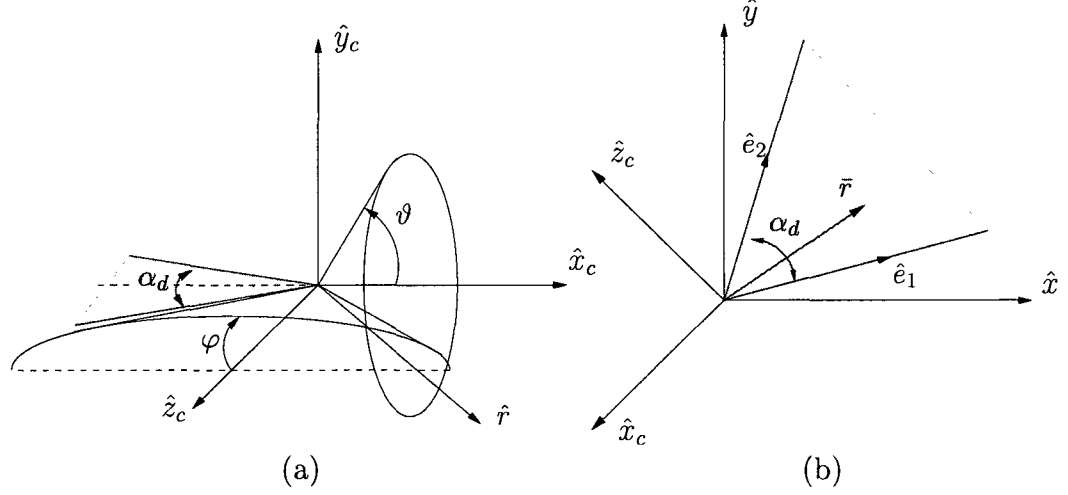
Figure A-1: (a)Sphero-conal coordinate system and the local cartesian coordinates defined at the tip of the angular sector (b) Plane angular sector in the global coordinate system (x, y, z).

$r = r_0$, and $\varphi = \varphi_0$ defines a unique point in space. The metric coefficients for the sphero-conal coordinate system are

$$s_r = 1 \tag{A-4}$$

$$s_\vartheta = r \left[\frac{k^2 \sin^2 \vartheta + k'^2 \sin^2 \varphi}{1 - k^2 \cos^2 \vartheta} \right]^{\frac{1}{2}} \tag{A-5}$$

$$s_\varphi = r \left[\frac{k^2 \sin^2 \vartheta + k'^2 \sin^2 \varphi}{1 - k'^2 \cos^2 \varphi} \right]^{\frac{1}{2}}. \tag{A-6}$$

The gradient and the laplacian operators can easily be obtained as

$$\nabla = \hat{r} \frac{\partial}{\partial r} + \hat{\vartheta} \frac{\sqrt{1 - k^2 \cos^2 \vartheta}}{r \sqrt{k^2 \sin^2 \vartheta + k'^2 \sin^2 \varphi}} \frac{\partial}{\partial \vartheta} + \hat{\varphi} \frac{\sqrt{1 - k'^2 \cos^2 \varphi}}{r \sqrt{k^2 \sin^2 \vartheta + k'^2 \sin^2 \varphi}} \frac{\partial}{\partial \varphi} \tag{A-7}$$

$$\nabla^2 = \frac{1}{r^2} \frac{\partial}{\partial r} r^2 \frac{\partial}{\partial r} + \frac{1}{r^2 (k^2 \sin^2 \vartheta + k'^2 \sin^2 \varphi)} \left[\sqrt{1 - k^2 \cos^2 \vartheta} \frac{\partial}{\partial \vartheta} \left(\sqrt{1 - k^2 \cos^2 \vartheta} \frac{\partial}{\partial \vartheta} \right) \right.$$
$$\left. + \sqrt{1 - k'^2 \cos^2 \varphi} \frac{\partial}{\partial \varphi} \left(\sqrt{1 - k'^2 \cos^2 \varphi} \frac{\partial}{\partial \varphi} \right) \right]. \tag{A-8}$$

In order to be able to evaluate the current density on the plane angular sector for a given direction of incidence using the eigenfunction expansion, it is necessary to transform the position vector of the observation point and the direction of incidence into the sphero-conal coordinate system. In this thesis, the plane angular sector is specified in a global coordinate system as shown in Fig. A-1(b). The unit vector for the direction of incidence is first transformed into the local cartesian coordinate system. Let the direction of incidence be

$$\hat{\beta}_i = \hat{x}_c x_c + \hat{y}_c y_c + \hat{z}_c z_c. \tag{A-9}$$

Then in the sphero-conal coordinate system, the direction of incidence specified by (ϑ_0, φ_0) can be obtained using

$$\vartheta_0 = \sin^{-1}\left\{\left[-\frac{k'^2 - y_c^2 k^2 - z_c^2 \mp \sqrt{[k'^2 - y_c^2 k^2 - z_c^2]^2 + 4k^2 y_c^2 k'^2}}{2k^2}\right]^{1/2}\right\} \tag{A-10}$$

$$\varphi_0 = \sin^{-1}\left(\frac{y_c}{\sin \vartheta_0}\right). \tag{A-11}$$

An observation point on the surface of the plane angular sector represented by $\mathbf{r} = \hat{x}_c x_c + \hat{y}_c y_c$ can easily be transformed into the sphero-conal coordinate system using (A-1). On the surface of the angular sector

$$\vartheta = \pi \tag{A-12}$$

$$\varphi = \cos^{-1}\left[\frac{z_c}{|\mathbf{r}|k'}\right]. \tag{A-13}$$

Appendix B

Dyadic Green's Function for the

Plane Angular Sector

A scalar Green's function in the uniformized sphero-conal coordinate system for the problem of the plane angular sector was first derived in [38]. The sphero-conal coordinate system is suitable for solving the scalar Helmholtz equation for conical boundaries. It is noted that in this coordinate system, a plane angular sector is simply a degenerate case of an elliptic cone surface. The scalar Helmholtz equation is separable and the boundary of the scattering structure coincides with a coordinate surface. As a consequence, the solution of the scalar problem can be constructed in a simple manner as demonstrated in Chapter 2. This appendix summarizes the derivation of the dyadic Green's function for an arbitrary current distribution $\bar{J}$ radiating in the vicinity of the plane angular sector. The expression for the current density on a plane angular sector illuminated by a plane wave is then obtained by using the large-argument form of the functions involving the source position $\mathbf{r}'$.

B.1 Vector Wave Equation

In order to derive an expression for the current density on a plane angular sector illuminated by a plane wave, the observation point is assumed to be closer to the tip of the angular sector than the source point ($\bar{r} \leq \bar{r}'$). The E-field satisfies the equation

$$\nabla \times \nabla \times \bar{E} - \kappa^2 \bar{E} = -j\omega\mu\bar{J} \tag{B-1}$$

and the boundary condition

$$\hat{n} \times \bar{E} = 0 \tag{B-2}$$

where $\hat{n}$ is the surface normal. The E-field also satisfies the radiation condition as $r \to \infty$. The solution to (B-1) is given by
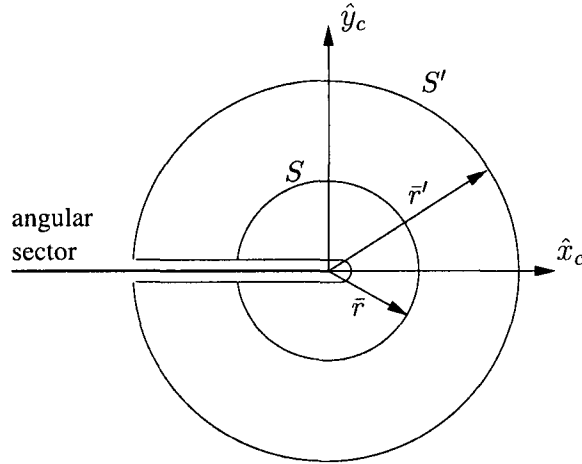
Figure B-1: Plane angular sector and the volumes S and S'.

$$\bar{E}(\bar{r}) = j\omega\mu \int_V \bar{\bar{\Gamma}}(\bar{r}, \bar{r}') \cdot \bar{J}(\bar{r}')dV$$
$$+ \int_S \left[\bar{E}(\bar{r}') \times \hat{n} \cdot \nabla' \times \bar{\bar{\Gamma}}(\bar{r}, \bar{r}') \right] dS \tag{B-3}$$

where V is the volume enclosing $\bar{J}$ and S is the plane angular sector. The vectors $\bar{r}'$ and $\bar{r}$ denote the source and observation point vectors. In order to obtain the field

due to a vector point source $\hat{a}$, a vector Green's function $\bar{G}(\bar{r}, \bar{r}')$ can be defined such that $\bar{G}(\bar{r}, \bar{r}') = \bar{\bar{\Gamma}}(\bar{r}, \bar{r}') \cdot \hat{a}$. Then, the vector Green's function should satisfy

$$\nabla \times \nabla \times \bar{G}(\bar{r}, \bar{r}') - \kappa^2 \bar{G}(\bar{r}, \bar{r}') = -\hat{a}\delta(|\bar{r} - \bar{r}'|) \tag{B-4}$$

$$\hat{n} \times \bar{G}(\bar{r}, \bar{r}') = 0. \tag{B-5}$$

Since $\bar{G}$ is a divergenceless vector, it can be represented using the vector wave functions (see Section 2.2) as

$$\bar{G}(\bar{r}, \bar{r}') = \sum_n a_n(\bar{r}')\bar{M}_{n2}^{(1)}(\bar{r}) + b_n(\bar{r}')\bar{N}_{n1}^{(1)}(\bar{r}) \tag{B-6}$$

in which n denotes the type and index of the vector wave functions. The subscripts 1 and 2 implies that the vector wave function is the solution of Dirichlet and Neumann boundary conditions respectively. From (2.46) and (2.47) the vector wave functions can be expressed as

$$\bar{M}_q^{(1)}(\bar{r}) = j_{\nu q}(\kappa r)\bar{m}_q(\vartheta, \varphi) \tag{B-7}$$

$$\bar{M}_q^{(2)}(\bar{r}) = h_{\nu q}^{(2)}(\kappa r)\bar{m}_q(\vartheta, \varphi) \tag{B-8}$$

$$\bar{N}_q^{(1)}(\bar{r}) = \frac{j_{\nu q}(\kappa r)}{\kappa r}\bar{\ell}_q + \frac{[rj_{\nu q}(\kappa r)]'}{\kappa r}[\hat{r} \times \bar{m}_q(\vartheta, \varphi)] \tag{B-9}$$

$$\bar{N}_q^{(2)}(\bar{r}) = \frac{h_{\nu q}^{(2)}(\kappa r)}{\kappa r}\bar{\ell}_q + \frac{[rh_{\nu q}^{(2)}(\kappa r)]'}{\kappa r}[\hat{r} \times \bar{m}_q(\vartheta, \varphi)] \tag{B-10}$$

where $\bar{m}_q$ and $\bar{\ell}_q$ are given by (2.48) and (2.49). Green's second identity for the vectors $\bar{G}(\bar{r}, \bar{r}')$ and $\bar{M}_{p2}^{(2)}(\bar{r})$ can be expressed as

$$\int_V \left[\bar{M}_{p2}^{(2)}(\bar{r}) \cdot \nabla \times \nabla \times \bar{G}(\bar{r}, \bar{r}') - \bar{G}(\bar{r}, \bar{r}') \cdot \nabla \times \nabla \times \bar{M}_{p2}^{(2)}(\bar{r}) \right]$$
$$= \int_S \left[\bar{G}(\bar{r}, \bar{r}') \times \nabla \times \bar{M}_{p2}^{(2)}(\bar{r}) - \bar{M}_{p2}^{(2)}(\bar{r}) \times \nabla \times \bar{G}(\bar{r}, \bar{r}') \right] \cdot \hat{n}dS \tag{B-11}$$

where V is the volume enclosed by S in Fig. B-1 and the surface normal $\hat{n} = \hat{r}$. Using (B-4) and the fact that $\bar{M}_{p2}^{(2)}(\bar{r})$ satisfies the homogeneous Helmholtz equation, the volume integral can easily be evaluated as

$$I_1 = \int_V \left[\bar{M}_{p2}^{(2)}(\bar{r}) \cdot \nabla \times \nabla \times \bar{G}(\bar{r}, \bar{r}') - \bar{G}(\bar{r}, \bar{r}') \cdot \nabla \times \nabla \times \bar{M}_{p2}^{(2)}(\bar{r}) \right]$$
$$= \int_V \left[\bar{M}_{p2}^{(2)}(\bar{r}) \cdot [\kappa^2 \bar{G}(\bar{r}, \bar{r}') - \hat{a}\delta(|\bar{r} - \bar{r}'|)] - \bar{G}(\bar{r}, \bar{r}') \cdot [\kappa^2 \bar{M}_{p2}^{(2)}(\bar{r})] \right] dV. \tag{B-12}$$

103

Then

$$I_1 = -\bar{M}_{p2}^{(2)}(\bar{r}') \cdot \hat{a}. \tag{B-13}$$

Using the vector identities

$$\left[\bar{G}(\bar{r}, \bar{r}') \times \nabla \times \bar{M}_{p2}^{(2)}(\bar{r})\right] \cdot \hat{n} = \hat{n} \times \bar{G}(\bar{r}, \bar{r}') \cdot \nabla \times \bar{M}_{p2}^{(2)}(\bar{r})$$

$$\left[\bar{M}_{p2}^{(2)}(\bar{r}) \times \nabla \times \bar{G}(\bar{r}, \bar{r}')\right] \cdot \hat{n} = \hat{n} \times \bar{M}_{p2}^{(2)}(\bar{r}) \cdot \nabla \times \bar{G}(\bar{r}, \bar{r}')$$

the surface integral in (B-11) can be expressed as

$$I_2 = \int_S \left[\hat{r} \times \bar{G}(\bar{r}, \bar{r}') \cdot \nabla \times \bar{M}_{p2}^{(2)}(\bar{r}) - \hat{r} \times \bar{M}_{p2}^{(2)}(\bar{r}) \cdot \nabla \times \bar{G}(\bar{r}, \bar{r}')\right] dS. \tag{B-14}$$

It is noted that the surface reduces to sphere of radius r because of the boundary conditions on the surface of the quarter plane. Using (B-6) in (B-14)

$$I_2 = \kappa \int_S \sum_n a_n(\bar{r}')[\hat{r} \times \bar{M}_{n2}^{(1)}(\bar{r}) \cdot \bar{N}_{p2}^{(2)}(\bar{r}) - \hat{r} \times \bar{M}_{p2}^{(2)}(\bar{r}) \cdot \bar{N}_{n2}^{(1)}(\bar{r})]$$

$$+ b_n(\bar{r}')[\hat{r} \times \bar{N}_{n1}^{(1)}(\bar{r}) \cdot \bar{N}_{p2}^{(2)}(\bar{r}) - \hat{r} \times \bar{M}_{p2}^{(2)}(\bar{r}) \cdot \bar{M}_{n1}^{(1)}(\bar{r})]dS.$$

Using the symmetry properties of the vector wave functions, it can be shown that the second term of the integrand is zero. Therefore the surface integral reduces to

$$I_2 = \kappa \sum_n a_n(\bar{r}') \int_S [\hat{r} \times \bar{M}_{n2}^{(1)}(\bar{r}) \cdot \bar{N}_{p2}^{(2)}(\bar{r}) - \hat{r} \times \bar{M}_{p2}^{(2)}(\bar{r}) \cdot \bar{N}_{n2}^{(1)}(\bar{r})]dS \tag{B-15}$$

$$= \kappa \sum_n a_n(\bar{r}') S_n.$$

Using (B-7)-(B-10) in (B-15), the surface integral can be expressed as

$$S_n = \frac{1}{\kappa r} \left\{ j_{n2}(\kappa r)[r h_{p2}^{(2)}(\kappa r)]' - h_{p2}^{(2)}(\kappa r)[r j_{n2}(\kappa r)]' \right\}$$

$$r^2 \int_S \frac{T_{p2}'(\vartheta) P_{p2}(\varphi) T_{n2}'(\vartheta) P_{n2}(\varphi)}{s_\vartheta^2} + \frac{T_{p2}(\vartheta) P_{p2}'(\varphi) T_{n2}(\vartheta) P_{n2}'(\varphi)}{s_\varphi^2} dS. \tag{B-16}$$

Using the orthogonality relationship of the Lamé functions, it can be shown that the integral in (B-16) is nonzero only when $n = p$. Using $dS = s_\vartheta s_\varphi d\vartheta d\varphi$ and

$$j_{n2}(\kappa r)[r h_{p2}^{(2)}(\kappa r)]' - h_{p2}^{(2)}(\kappa r)[r j_{n2}(\kappa r)]' = \frac{j}{\kappa r} \tag{B-17}$$

104

in (B-16), the expression for S_n can be written as

$$
S_n = \begin{cases} \frac{j}{\kappa^2} \int_0^{2\pi} \int_0^{\pi} \left\{ \frac{[T'_{p2}(\vartheta)P_{p2}(\varphi)]^2}{s_\vartheta} s_\varphi + \frac{[T_{p2}(\vartheta)P'_{p2}(\varphi)]^2}{s_\varphi} s_\vartheta \right\} d\vartheta d\varphi, & n = p \\ 0, & n \neq p. \end{cases} \tag{B-18}
$$

Using (B-18) in (B-15), the surface integral is found to be

$$
I_2 = a_p(\bar{r}')\frac{j}{\kappa}\Lambda_{p2} \tag{B-19}
$$

where

$$
\Lambda_{p2} = \int_0^{2\pi} \int_0^{\pi} \left\{ \frac{[T'_{p2}(\vartheta)P_{p2}(\varphi)]^2}{s_\vartheta} s_\varphi + \frac{[T_{p2}(\vartheta)P'_{p2}(\varphi)]^2}{s_\varphi} s_\vartheta \right\} d\vartheta d\varphi. \tag{B-20}
$$

It should be noted that all other terms in the series (B-15) are zero. Finally, $a_p(\bar{r}')$ can be obtained by using (B-19) and (B-13) in (B-11)

$$
a_p(\bar{r}') = \frac{j\kappa \bar{M}_{p2}^{(2)}(\bar{r}') \cdot \hat{a}}{\Lambda_{p2}}. \tag{B-21}
$$

The same procedure can be repeated with $\bar{N}_{p1}^{(2)}(\bar{r})$ instead of $\bar{M}_{p2}^{(2)}(\bar{r})$ in (B-11) to obtain an expression for $b_p(\bar{r}')$. Using (B-21), it can be deduced that

$$
b_p(\bar{r}') = \frac{j\kappa \bar{N}_{p1}^{(2)}(\bar{r}') \cdot \hat{a}}{\Lambda_{p1}}. \tag{B-22}
$$

Therefore, the electric field due to a vector point source $\hat{a}$ can be expressed as

$$
\bar{E}(\bar{r}, \bar{r}') = j\kappa \sum_n \frac{\bar{M}_{n2}^{(2)}(\bar{r}') \cdot \hat{a}\bar{M}_{n2}^{(1)}(\bar{r})}{\Lambda_{n2}} + \frac{\bar{N}_{n1}^{(2)}(\bar{r}') \cdot \hat{a}\bar{N}_{n1}^{(1)}(\bar{r})}{\Lambda_{n1}}. \tag{B-23}
$$

The surface current density on the plane angular sector is given by

$$
\bar{J}(\bar{r}) = \hat{n} \times [\bar{H}(r, \vartheta = \pi, 0 \leq \varphi \leq \pi) - \bar{H}(r, \vartheta = \pi, \pi \leq \varphi \leq \pi)] \tag{B-24}
$$

in which the surface normal $\hat{n}$ is $\hat{y}_c$ (see Fig. A-1). The magnetic field can easily be obtained from (B-23) using Maxwell's equations. The final expression for the surface current density follows directly from (B-24). The current density on a plane angular

105

sector for $\bar{r} \leq \bar{r}'$ is given by

$$\bar{J}(\bar{r}) = \frac{-2\kappa}{\eta} \sum_{n=1}^{\infty} \frac{\bar{M}_{on2}^{(2)}(\bar{r}') \cdot \hat{a}}{\Lambda_{on2}} T_{on2}(\pi)$$

$$[-\nu(\nu+1)\frac{j_\nu(\kappa r)}{\kappa r}P_{on2}(\varphi)\hat{\varphi} + \frac{\frac{d}{dr}(rj_\nu(\kappa r))}{\kappa r \sin \varphi}\sqrt{1+\sin^2 \varphi}P'_{on2}(\varphi)\hat{r}]$$

$$+\frac{\bar{N}_{en1}^{(2)}(\bar{r}') \cdot \hat{a}}{\Lambda_{en1}}\frac{j_\nu(\kappa r)}{\sin \varphi}T'_{en1}(\pi)P_{en1}(\varphi)\hat{r}. \qquad \text{(B-25)}$$

106

Appendix C

Eigenvalue Pairs

Table C-1: Eigenvalue pairs for the odd Neumann problem for $\alpha_d = 90°$ ($k^2 = 0.5$). The eigenfunction types 1 and 2 denote $P_{o2}^{(1)}$ and $P_{o2}^{(2)}$ respectively.

ν	μ	type	ν	μ	type
0.814644	-0.189508	2	8.790567	-0.763712	2
1.597126	0.795775	2	8.975449	-7.724364	1
1.955320	-1.552891	1	8.998651	-16.417713	2
2.520875	2.621753	2	8.999963	-26.751471	1
2.801147	-0.349178	1	9.000000	-38.660286	2
2.990671	-3.886619	2	9.500000	43.181561	2
3.504194	5.424531	2	9.500017	30.563993	1
3.617049	1.261785	1	9.500659	19.518759	2
3.938053	-2.308192	2	9.513223	10.130462	1
3.998142	-7.193804	1	9.637954	2.490856	2
4.500818	9.219427	2	9.915986	-4.344004	1
4.532030	3.680930	1	9.993033	-12.744469	2
4.795764	-0.494747	2	9.999681	-22.866467	1
4.984158	-5.230457	1	9.999992	-34.626576	2
4.999641	-11.489923	2	10.000000	-47.952866	1
5.500156	14.012041	2	10.500000	52.974178	2
5.507777	7.067286	1	10.500004	38.939415	1
5.627034	1.691327	2	10.500154	26.466913	2
5.928010	-3.015884	1	10.503624	15.633493	1
5.996260	-9.123751	2	10.549193	6.544482	2
5.999932	-16.782949	1	10.789017	-0.891187	1
6.500029	19.804279	2	10.972285	-8.907550	2
6.501779	11.442933	1	10.998142	-18.757319	1
6.539436	4.675285	2	10.999928	-30.316997	2
6.792663	-0.632047	1	10.999999	-43.502392	1
6.979297	-6.502716	2	11.000000	-58.245510	2
6.999163	-14.002448	1	11.500000	63.766846	2
6.999988	-23.075371	2	11.500001	48.315521	1
7.500006	26.596592	2	11.500034	34.418350	2
7.500390	16.815985	1	11.500941	22.141430	1
7.510735	8.628466	2	11.515360	11.586781	2
7.633398	2.098806	1	11.641448	2.871227	1
7.921133	-3.691647	2	11.911922	-4.978156	2
7.994556	-10.966582	1	11.991669	-14.471322	1
7.999820	-19.877058	2	11.999529	-25.771765	2
7.999998	-30.367784	1	11.999985	-38.770058	1
8.500001	34.389023	2	12.000000	-53.378765	2
8.500083	23.189476	1	12.000000	-69.538193	1
8.502728	13.573640	2	12.499999	75.559540	2
8.544899	5.625997	1	12.500001	58.692123	1

Table C-2: Eigenvalue pairs for the even Dirichlet problem for $\alpha_d = 90°$ ($k^2 = 0.5$). The eigenfunction types 1 and 2 denote $P_{e1}^{(1)}$ and $P_{e1}^{(2)}$ respectively.

ν	μ	type	ν	μ	type
0.296568	0.089456	1	8.280985	0.548963	1
1.131244	-0.452788	2	8.459557	5.874331	2
1.426506	0.917649	1	8.497295	13.591759	1
2.039574	-1.702414	1	8.499918	23.190062	2
2.287566	0.216126	2	8.499999	34.389034	1
2.480879	2.667650	1	9.000001	-38.660290	2
3.009061	-3.937848	2	9.000038	-26.752028	1
3.146398	-0.825597	1	9.001343	-16.433693	2
3.408677	1.533192	2	9.023193	-7.935415	1
3.495887	5.437692	1	9.161119	-1.817754	2
4.001844	-7.207837	1	9.389215	3.196786	1
4.053802	-2.576199	2	9.487252	10.220277	2
4.284202	0.332447	1	9.499342	19.523735	1
4.470928	3.789495	2	9.499983	30.564125	2
4.499184	9.222710	1	9.500000	43.181564	1
5.000358	-11.493355	2	10.000000	-47.952866	1
5.015172	-5.334270	1	10.000008	-34.626701	2
5.153522	-1.170844	2	10.000319	-22.870892	1
5.399493	2.110182	1	10.006843	-12.820037	2
5.492437	7.101768	2	10.072187	-4.940698	1
5.499844	14.012799	1	10.280023	0.652209	2
6.000067	-16.783731	1	10.455774	6.865732	1
6.003695	-9.156192	2	10.496414	15.661986	2
6.062113	-3.395878	1	10.499847	26.468201	1
6.282283	0.442732	2	10.499997	38.939445	2
6.464373	4.852334	1	10.500000	52.974178	1
6.498231	11.452479	2	11.000000	-58.245510	2
6.499971	19.804445	1	11.000002	-43.502415	1
7.000013	-23.075542	2	11.000073	-30.318153	2
7.000834	-14.011423	1	11.001847	-18.781401	1
7.019670	-6.659832	2	11.026077	-9.173084	2
7.157966	-1.499885	1	11.163525	-2.127235	1
7.393535	2.662376	2	11.385866	3.717567	2
7.489614	8.689046	1	11.485233	11.708070	1
7.499610	16.818417	2	11.499062	22.149735	2
7.499995	26.596626	1	11.499966	34.418671	1
8.000003	-30.367821	1	11.500000	63.766846	1
8.000180	-19.879356	2	11.500000	48.315529	2
8.005362	-11.019791	1	12.000000	-69.538193	1
8.067855	-4.180817	2	12.000001	-53.378773	2

Table C-3: Eigenvalue pairs for the odd Neumann problem for $\alpha_d = 60°$ ($k^2 = 0.75$). The eigenfunction types 1 and 2 denote $P_{o2}^{(1)}$ and $P_{o2}^{(2)}$ respectively.

ν	μ	type	ν	μ	type
0.919034	-0.543760	2	8.995657	-11.602567	2
1.756871	0.031390	2	8.999839	-20.931631	1
1.992185	-2.754786	1	8.999996	-32.078022	2
2.612871	0.908156	2	9.000000	-59.710823	2
2.960147	-2.035264	1	9.000000	-45.011600	1
2.999307	-6.405681	2	9.500094	20.258299	2
3.542792	2.211462	2	9.504033	11.578403	1
3.880761	-1.099050	1	9.567658	4.265999	2
3.995190	-5.497543	2	9.858991	-2.085347	1
3.999942	-11.541562	1	9.987453	-9.539968	2
4.515744	3.988794	2	9.999370	-18.778353	1
4.752600	0.037849	1	9.999982	-29.855602	2
4.980944	-4.385648	2	10.000000	-42.744041	1
4.999484	-10.408962	1	10.000000	-57.412796	2
4.999995	-18.175459	2	10.000000	-73.844734	1
5.505745	6.251943	2	10.500033	25.007597	2
5.630938	1.455295	1	10.501590	15.325063	1
5.943727	-3.081733	2	10.530648	7.036269	2
5.997462	-9.083114	1	10.751041	0.041977	1
5.999949	-16.809904	2	10.968066	-7.332872	2
6.000000	-26.309238	1	10.997927	-16.467516	1
6.502079	9.007297	2	10.999917	-27.455143	2
6.558450	3.277699	1	10.999998	-40.283058	1
6.866817	-1.606806	2	11.000000	-54.911018	2
6.990906	-7.575749	1	11.000000	-89.478661	2
6.999699	-15.250090	2	11.000000	-71.314148	1
6.999996	-24.710073	1	11.500012	30.256927	2
7.000000	-35.943062	2	11.500617	19.569630	1
7.500746	12.258878	2	11.513430	10.284994	2
7.524581	5.562234	1	11.645576	2.427197	1
7.751512	0.040468	2	11.927299	-4.995410	2
7.973498	-5.897185	1	11.994036	-14.012280	1
7.998722	-13.509845	2	11.999693	-24.889601	2
7.999968	-22.913399	1	11.999990	-37.638573	1
8.000000	-47.076931	1	12.000000	-52.213093	2
8.000000	-34.110657	2	12.000000	-68.578636	1
8.500266	16.008869	2	12.000000	-86.715622	2
8.510057	8.326125	1	12.000001	-106.612595	1
8.639884	1.954886	2	12.500004	36.006332	2
8.934011	-4.060856	1	12.500237	24.313856	1

110

Table C-4: Eigenvalue pairs for the even Dirichlet problem for $\alpha_d = 60°$ ($k^2 = 0.75$). The eigenfunction types 1 and 2 denote $P_{e1}^{(1)}$ and $P_{e1}^{(2)}$ respectively.

ν	μ	type	ν	μ	type
0.240099	0.036081	1	8.024343	-6.141800	1
1.061285	-0.738683	2	8.169662	-1.209826	2
1.347983	0.403861	1	8.396811	2.714182	1
2.007530	-2.798964	1	8.490358	8.403337	2
2.151359	-0.449050	2	8.499735	16.011175	1
2.421223	1.147938	1	9.000000	-45.011600	1
3.000688	-6.411735	2	9.000000	-59.710823	2
3.034592	-2.229582	1	9.000004	-32.078091	2
3.247566	0.045080	2	9.000161	-20.934269	1
3.464343	2.349656	1	9.004269	-11.657570	2
4.000058	-11.542243	1	9.055419	-4.598423	1
4.004704	-5.536935	2	9.249158	0.048021	2
4.088333	-1.579006	1	9.443933	4.726283	1
4.335545	0.814981	2	9.496038	11.614032	2
4.485457	4.058327	1	9.499907	20.259209	1
5.000004	-18.175529	2	10.000000	-73.844734	1
5.000514	-10.414780	1	10.000000	-42.744049	1
5.017776	-4.528127	2	10.000000	-57.412796	2
5.163861	-0.842000	1	10.000019	-29.855965	2
5.405077	1.959075	2	10.000628	-18.788313	1
5.494434	6.283815	1	10.012030	-9.689419	2
6.000000	-26.309244	1	10.105868	-3.079492	1
6.000051	-16.810635	2	10.326370	1.549540	2
6.002507	-9.110360	1	10.472269	7.290071	1
6.047678	-3.449885	2	10.498422	15.340842	2
6.248725	0.047054	1	10.499968	25.007952	1
6.451498	3.575316	2	11.000000	-71.314148	1
6.497945	9.021065	1	11.000000	-54.911018	2
7.000000	-35.943066	2	11.000000	-89.478661	2
7.000005	-24.710154	1	11.000003	-40.283108	1
7.000301	-15.254250	2	11.000083	-27.456709	2
7.008792	-7.667480	1	11.002055	-16.499069	1
7.099307	-2.348549	2	11.029075	-7.681654	2
7.329880	1.191562	1	11.173258	-1.562274	1
7.477594	5.720212	2	11.391429	3.435752	2
7.499257	12.264594	1	11.487210	10.414625	1
8.000000	-34.110664	2	11.499386	19.576406	2
8.000000	-47.076931	1	11.499989	30.257063	1
8.000033	-22.913950	1	12.000000	-86.715622	2
8.001269	-13.526807	2	12.000000	-68.578636	1

Table C-5: Eigenvalue pairs for the odd Neumann problem for $\alpha_d = 30°$ ($k^2 = 0.933$). The eigenfunction types 1 and 2 denote $P_{o2}^{(1)}$ and $P_{o2}^{(2)}$ respectively.

ν	μ	type	ν	μ	type
0.981610	-0.868771	2	8.999996	-21.212454	2
1.940284	-0.679924	2	9.000000	-58.858894	1
1.999548	-3.665138	1	9.000000	-44.373657	2
2.872336	-0.406043	2	9.000000	-31.823843	1
2.997730	-3.464635	1	9.000000	-75.278137	2
2.999990	-8.298757	2	9.517976	4.332814	2
3.784127	-0.050167	2	9.771800	-0.119742	1
3.993141	-3.195542	1	9.983356	-5.186747	2
3.999932	-8.037456	2	9.999414	-11.918397	1
4.000000	-14.796936	1	9.999989	-20.572573	2
4.695659	0.394735	2	10.000000	-58.204044	1
4.983777	-2.856926	1	10.000000	-74.621323	2
4.999727	-7.713409	2	10.000000	-31.176374	1
4.999998	-14.469728	1	10.000000	-43.721691	2
5.000000	-23.161114	2	10.000000	-92.972458	1
5.625532	0.942946	2	10.511025	5.495198	2
5.966944	-2.448261	1	10.702304	0.648947	1
5.999181	-7.327841	2	10.970843	-4.503163	2
5.999991	-14.079602	1	10.998753	-11.235719	1
6.000000	-33.391323	1	10.999969	-19.874264	2
6.000000	-22.767899	2	11.000000	-92.249786	1
6.577904	1.606061	2	11.000000	-57.485832	1
6.939290	-1.969790	1	11.000000	-43.007320	2
6.997957	-6.881805	2	11.000000	-73.900513	2
6.999967	-13.627883	1	11.000000	-30.468006	1
7.000000	-22.311348	2	11.000000	-112.532806	2
7.000000	-45.487568	2	11.506760	6.786998	2
7.000000	-32.932167	1	11.642207	1.512959	1
7.547833	2.390163	2	11.951367	-3.760244	2
7.897454	-1.422523	1	11.997523	-10.499025	1
7.995514	-6.376063	2	11.999926	-19.119074	2
7.999903	-13.116052	1	11.999998	-29.699842	1
7.999999	-21.792479	2	12.000000	-56.704880	1
8.000000	-32.409405	1	12.000000	-133.959183	1
8.000000	-44.962505	2	12.000000	-91.463043	1
8.000000	-59.449837	1	12.000000	-42.231361	2
8.529316	3.298377	2	12.000000	-73.116173	2
8.840231	-0.806943	1	12.000000	-111.744286	2
8.991041	-5.811014	2	12.504141	8.209424	2
8.999748	-12.545689	1	12.596326	2.484263	1

Table C-6: Eigenvalue pairs for the even Dirichlet problem for $\alpha_d = 30°$ ($k^2 = 0.933$). The eigenfunction types 1 and 2 denote $P_{e1}^{(1)}$ and $P_{e1}^{(2)}$ respectively.

ν	μ	type	ν	μ	type
0.181066	0.007108	1	8.000096	-13.117442	1
1.016310	-0.932195	2	8.004371	-6.422143	2
1.249953	0.094527	1	8.073550	-1.969524	1
2.000449	-3.668471	1	8.299887	0.552943	2
2.044967	-0.862191	2	8.474874	3.464078	1
2.304271	0.261211	1	9.000000	-75.278137	2
3.000010	-8.298864	2	9.000000	-58.858894	1
3.002227	-3.480959	1	9.000000	-44.373657	2
3.081812	-0.753247	2	9.000000	-31.823843	1
3.349976	0.514484	1	9.000004	-21.212524	2
4.000000	-14.796939	1	9.000251	-12.549252	1
4.000068	-8.038206	2	9.008565	-5.900562	2
4.006575	-3.243316	1	9.104577	-1.597641	1
4.123606	-0.601701	2	9.339114	1.025367	2
4.388268	0.864914	1	9.483767	4.450813	1
5.000000	-23.161114	2	10.000000	-58.204044	1
5.000002	-14.469756	1	10.000000	-74.621323	2
5.000272	-7.716369	2	10.000000	-31.176374	1
5.014890	-2.964881	1	10.000000	-43.721691	2
5.167981	-0.402676	2	10.000000	-92.972458	1
5.419431	1.324653	1	10.000011	-20.572779	2
6.000000	-33.391323	1	10.000582	-11.926580	1
6.000000	-22.767899	2	10.015418	-5.347112	2
6.000009	-14.079731	1	10.139931	-1.201843	1
6.000812	-7.336580	2	10.374220	1.596432	2
6.028431	-2.655167	1	10.489680	5.577384	1
6.213106	-0.149753	2	11.000000	-112.532806	2
6.443767	1.905417	1	11.000000	-92.249786	1
7.000000	-32.932167	1	11.000000	-57.485832	1
7.000000	-22.311354	2	11.000000	-43.007324	2
7.000000	-45.487568	2	11.000000	-73.900513	2
7.000032	-13.628351	1	11.000000	-30.468016	1
7.002013	-6.903242	2	11.000031	-19.874805	2
7.047961	-2.321964	1	11.001236	-11.252924	1
7.257504	0.165344	2	11.025831	-4.771136	2
7.461920	2.616558	1	11.178240	-0.774246	1
8.000000	-32.409405	1	11.404479	2.280342	2
8.000000	-44.962505	2	11.493522	6.843231	1
8.000000	-59.449837	1	12.000000	-111.744286	2
8.000001	-21.792500	2	12.000000	-56.704880	1

113

Appendix D

Numerical Procedures

D.1   Normalized Area Coordinate System

Consider a point defined by $\bar{r}$ in the global coordinate system as shown in Fig. D-1. The normalized area coordinates for this point are defined as

$$\xi_k = \frac{A_k}{A} \qquad\qquad\text{(D-1)}$$

where A denotes the area of the triangle and A_i is the area of the sub triangle formed by the point $\bar{r}$ and edge i as shown in Fig. D-1. The value of the RWG basis function at a given point inside the triangle is proportional to the position vector of the point with respect to the pertinent vertex. These vectors can be expressed in areal coordinates as

$$\bar{\rho}_i = \xi_{i+1}\bar{\ell}_{i-1} - \xi_{i-1}\bar{\ell}_{i+1} \qquad\qquad\text{(D-2)}$$

$$\bar{\rho}_{i+1} = \xi_{i-1}\bar{\ell}_i - \xi_i\bar{\ell}_{i-1} \qquad\qquad\text{(D-3)}$$

$$\bar{\rho}_{i-1} = \xi_i\bar{\ell}_{i+1} - \xi_{i+1}\bar{\ell}_i. \qquad\qquad\text{(D-4)}$$

The local coordinates can be transformed into global coordinates by using the relation $\bar{r} = \bar{r}_k + \bar{\rho}_k$ where $k = \{i, \ i+1, \ i-1\}$. Substituting (D-2)-(D-4) in this equation, it

can be shown that

$$\bar{r} = \xi_i \bar{r}_i + \xi_{i+1} \bar{r}_{i+1} + \xi_{i-1} \bar{r}_{i-1}. \tag{D-5}$$
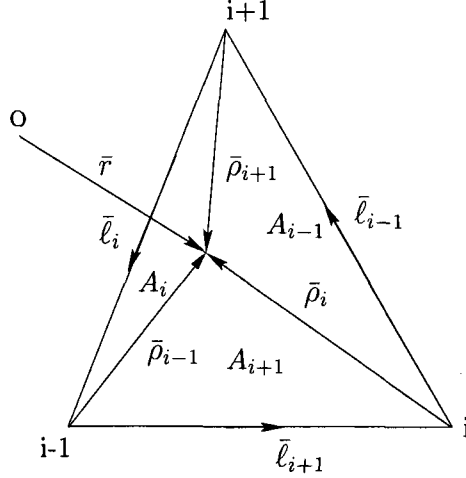
Figure D-1: Area coordinate system.

D.2   Matrix Equation

After the testing procedure, the EFIE can be expressed as

$$\int_S \bar{E}^i(\bar{r}) \cdot \bar{f}_m(\bar{r}) dS = j\omega \int_S \bar{A}(\bar{r}) \cdot \bar{f}_m(\bar{r}) dS + \int_S \nabla \phi(\bar{r}) \cdot \bar{f}_m(\bar{r}) dS \tag{D-6}$$

where $\bar{f}_m$ denotes the testing function and the magnetic vector and electric scalar potentials are given by

$$\bar{A}(\bar{r}) = \mu \int_{S'} \bar{J}(\bar{r}')g(\bar{r}, \bar{r}') dS' \tag{D-7}$$

$$\phi(\bar{r}) = \frac{j}{\omega \epsilon} \int_{S'} \nabla' \cdot \bar{J}(\bar{r}')g(\bar{r}, \bar{r}') dS' \tag{D-8}$$

where

$$g(\bar{r}, \bar{r}') = \frac{e^{-jkR}}{4\pi R}, \quad R = |\bar{r} - \bar{r}'|$$

115

denotes the free-space Green's function. Using the vector identity

$$\nabla \phi \cdot \bar{f}_m = \nabla \cdot (\phi \bar{f}_m) - \phi \nabla \cdot \bar{f}_m$$

the second integral in (D-6) can be expressed as

$$\int_S \nabla \phi \cdot \bar{f}_m dS = \int_S \nabla \cdot (\phi \bar{f}_m) dS - \int_S \phi \nabla \cdot \bar{f}_m dS. \qquad (\text{D-9})$$

Then, using the Gauss' theorem, the first term in (D-9) can be written as

$$\int_S \nabla \cdot (\phi \bar{f}_m) dS = \oint_C (\phi \bar{f}_m \cdot \hat{n}) d\ell \qquad (\text{D-10})$$

where S represents an open surface and C is the edge curve enclosing S. $\hat{n}$ denotes the edge normal. Since the basis functions $\bar{f}_m$ are tangential to the boundary, $\bar{f}_m \cdot \hat{n} = 0$. Therefore, (D-6) reduces to

$$\int_S \bar{E}^i(\bar{r}) \cdot \bar{f}_m(\bar{r}) dS = j\omega \int_S \bar{A}(\bar{r}) \cdot \bar{f}_m(\bar{r}) dS - \int_S \phi(\bar{r}) \nabla \cdot \bar{f}_m(\bar{r}) dS \qquad (\text{D-11})$$

Next, the current density is approximated in terms of basis functions as

$$\bar{J}(\bar{r}) = \sum_{n=1}^{N} I_n \bar{f}_n(\bar{r}). \qquad (\text{D-12})$$

Substituting (D-12), it follows from (D-7) and (D-8) that

$$\bar{A}(\bar{r}) = \mu \sum_{n=1}^{N} I_n \left\{ \int_{T_n^+} \bar{f}_n(\bar{r}') g(\bar{r}, \bar{r}') dS' + \int_{T_n^-} \bar{f}_n(\bar{r}') g(\bar{r}, \bar{r}') dS' \right\} \qquad (\text{D-13})$$

$$\phi(\bar{r}) = \frac{j}{\omega \epsilon} \sum_{n=1}^{N} I_n \left\{ \int_{T_n^+} [\nabla' \cdot \bar{f}_n(\bar{r}')] g(\bar{r}, \bar{r}') dS' + \int_{T_n^-} [\nabla' \cdot \bar{f}_n(\bar{r}')] g(\bar{r}, \bar{r}') dS' \right\} . (\text{D-14})$$

Using (D-13) and (D-14) in (D-11), the EFIE yields an $N \times N$ matrix equation that be expressed as

$$\bar{V} = \bar{\bar{Z}} \bar{I} \qquad (\text{D-15})$$

where

$$\bar{I} = \left[I_1, I_2, I_3, ..., I_N \right]^T . \qquad (\text{D-16})$$
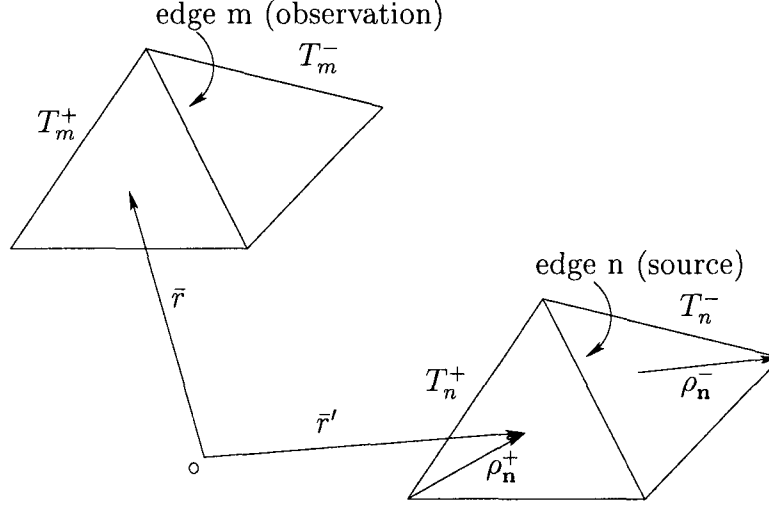
Figure D-2: Evaluation of Z_{mn}.

The elements of the vector $\bar{V}$ and the matrix $\bar{\bar{Z}}$ are given by

$$V_m = \int_{T_m^+} \bar{E}^i(\bar{r}) \cdot \bar{f}_m(\bar{r})dS + \int_{T_m^-} \bar{E}^i(\bar{r}) \cdot \bar{f}_m(\bar{r})dS, \quad m = 1, ..., N \qquad (\text{D-17})$$

$$Z_{mn} = j\omega(K_{mn}^+ + K_{mn}^-) - (P_{mn}^+ + P_{mn}^-), \quad m = 1, ..., N; n = 1, ..., N \qquad (\text{D-18})$$

where

$$K_{mn}^{\mp} = \int_{T_m^{\mp}} [\mu \int_{S'} \bar{f}_n(\bar{r}')g(\bar{r}, \bar{r}')dS'] \cdot \bar{f}_m dS \qquad (\text{D-19})$$

$$P_{mn}^{\mp} = \int_{T_m^{\mp}} [\frac{j}{\omega\epsilon} \int_{S'} \nabla' \cdot \bar{f}_n(\bar{r}')g(\bar{r}, \bar{r}')dS']\nabla \cdot \bar{f}_m dS. \qquad (\text{D-20})$$

The edge elements m and n are interpreted as the observation and source edges as depicted in Fig. D-2. In order to evaluate the integral over a triangular region $T_m^{\pm}$ or $T_n^{\pm}$, the integral is first expressed in terms of the areal coordinates. Consider the integral

$$I_t = \int_{T_m^{\mp}} f(x, y)dxdy. \qquad (\text{D-21})$$

Let the vertices of the triangular region $T_m^{\mp}$ be denoted by $\bar{r}_i = (x_i, y_i, z_i)$, $i = 1, 2, 3$. Then, an arbitrary point $\bar{r} = (x, y, z)$ in $T_m^{\mp}$ can be expressed as

$$\bar{r} = \xi_1 \bar{r}_1 + \xi_2 \bar{r}_2 + (1 - \xi_1 - \xi_2)\bar{r}_3. \qquad (\text{D-22})$$

117

Thus, the integral (D-21) can be expressed as

$$I_t = \int_0^1 \int_0^{1-\xi_2} f(x(\xi_1,\xi_2),y(\xi_1,\xi_2))|\mathcal{J}|d\xi_1 d\xi_2 \qquad (D\text{-}23)$$

in which

$$\mathcal{J} = \frac{\partial(x,y)}{\partial(\xi_1,\xi_2)} = \begin{vmatrix} \frac{\partial x}{\partial \xi_1} & \frac{\partial x}{\partial \xi_2} \\ \frac{\partial y}{\partial \xi_1} & \frac{\partial y}{\partial \xi_2} \end{vmatrix} = 2S_m^{\mp}$$

where $S_m^{\mp}$ is the surface area of the triangle $T_m^{\mp}$. Using this result, (D-23) can numerically be evaluated using an N-point Gaussian quadrature given by

$$I_t = 2S_m^{\mp} \sum_{i=1}^{N} W_i f(\xi_1^{(i)}, \xi_2^{(i)}). \qquad (D\text{-}24)$$

The superscript i denotes the index of the integration nodes and W_i is the corresponding weight. In a MoM solution, the surface integrals are expressed in the same form as (D-24). Depending on the behavior of the integrand $f(x,y)$, various methods can be used to determine the weights W_i and abscissas $(\xi_1^{(i)}, \xi_2^{(i)})$ for a given N. N should be chosen based on the size of the triangular patch and the behavior of the integrand. For instance, in [35], regular RWG basis functions are used as the testing function and 1-point Gaussian quadrature was used in evaluating the testing integrals (i.e. integrals over $T_m^{\mp}$ in (D-19) and (D-20)). In this case, $W_1 = 0.5$ and $\xi_1^{(1)} = \xi_2^{(1)} = 1/3$. Notice that this corresponds to the center of the triangular patch. Substituting in (D-24), one finds that the integral is approximated simply by the value of the integrand at the center of the triangular patch multiplied by the area. When regular RWG basis functions are used as the testing functions, we use 3-point Gaussian quadrature to evaluate the testing integrals. Thus, (D-19) and (D-20) are expressed as

$$K_{mn}^{\mp} = 2S_m^{\mp}\mu \sum_{i=1}^{3} W_i \left\{ \int_{S'} \bar{f}_n(\bar{r}')g(\bar{r}_i,\bar{r}')dS' \right\} \cdot \bar{f}_m(\bar{r}_i) \qquad (D\text{-}25)$$

$$P_{mn}^{\mp} = 2S_m^{\mp}\frac{j}{\omega\epsilon} \sum_{i=1}^{3} W_i \left\{ \int_{S'} \nabla' \cdot \bar{f}_n(\bar{r}')g(\bar{r}_i,\bar{r}')dS' \right\} \nabla \cdot \bar{f}_m(\bar{r}_i). \qquad (D\text{-}26)$$

The weights W_i and abscissas in areal coordinates for 3-point Gaussian quadrature are listed in Table D-1. The potential integrals over the source patches ($T_n^{\mp}$ in Fig. D-2) can be evaluated in the same manner if the integrand is analytic over the domain of integration. This is the case when regular RWG basis functions are used. However, when singular basis functions are used for the boundary triangles, the weights and nodes should be chosen according to the behavior of the integrand. Numerical integration over the singular basis functions is presented in Section D.3.

Table D-1: 3-point Gaussian quadrature nodes.

i	W_i	$\xi_1^{(i)}$	$\xi_2^{(i)}$
1	1/6	2/3	1/6
2	1/6	1/6	2/3
3	1/6	1/6	1/6

D.3 Numerical Integration of the Singular Basis Functions

The potential integrals involving singular basis functions are evaluated using the Gauss-Radau Method. Consider the surface integral of a function $f(x,y)$ over a square region defined by $-1 \leq x \leq 1$ and $-1 \leq y \leq 1$. This integral can numerically be evaluated using the Gauss-Jacobi and Gauss-Legendre abscissas and weights for the x and y directions respectively. The integral can be expressed as

$$I = \int_{-1}^{1} \int_{-1}^{1} (1-x)^{\gamma}(1+x)^{\beta} f(x,y) dx dy = \sum_{m=1}^{M} \sum_{n=1}^{N} W_L^{(m)} W_J^{(n)}(\gamma, \beta) f(x_n, y_m) \quad \text{(D-27)}$$

where y_m and $W_L^{(m)}$ denote the mth Gauss-Legendre abscissa and weight. Similarly, x_n and $W_J^{(n)}$ are the Gauss-Jacobi abscissa and weight respectively. In the MoM

procedure, the potential integrals should be evaluated over triangular patches in the areal coordinate system. Thus, the square region in (D-27) is transformed into a triangular region by the change of variables

$$x = 2u - 1$$
$$y = \frac{4v}{1-x} - 1$$
$$dxdy = \frac{8}{1-v}dudv \tag{D-28}$$

resulting in

$$I = 2^{\gamma+\beta+2} \int_0^1 \int_0^{1-v} (1-u)^{\gamma-1} u^\beta f(u,v) dudv. \tag{D-29}$$

Using (D-29) and (D-27) the integral over the triangular region in the $u - v$ domain can be expressed as

$$\int_0^1 \int_0^{1-v} (1-u)^{\gamma-1} u^\beta f(u,v) dudv = \frac{1}{2^{\gamma+\beta+2}} \sum_{m=1}^{M} \sum_{n=1}^{N} W_L^{(m)} W_J^{(n)}(\gamma,\beta) f(u_n, v_m). \tag{D-30}$$

This equation can be used to evaluate the potential integrals in the MoM solution. For a given number of integration nodes (M and N), the nodes and weights are first calculated in the square domain in the range [-1,1] for the $\hat{x}$ and $\hat{y}$ directions. It should be noted that in the above, x was chosen to be the direction along which the integrand is singular. Thus, the Gauss-Jacobi nodes must be used along x (x_n, $W_J^{(n)}$). Along y, Gauss-Legendre abscissa and weights are calculated (y_m, $W_L^{(m)}$). These values can be calculated using widely available subroutines [42]. Each node is then mapped onto the $u - v$ domain using D-28 to obtain the corresponding abscissas $u_n - v_m$. Then, $f(u_n, v_m)$ can easily be calculated at each integration node. In particular, three different types of singularities are encountered in evaluating the potential integrals:

- $\xi_i^{\nu-1}$: For the basis functions of type $\bar{f}_{2,1}$ and $\bar{f}_{3,2}$, the potential integral takes the form

$$I_1 = \int_0^1 \int_0^{1-\xi_{i\mp1}} \xi_i^{\nu-1} f(\xi_i, \xi_{i\mp1}) d\xi_i d\xi_{i\mp1}. \tag{D-31}$$

120

Comparing (D-31) and (D-30),

$$I_1 = \frac{1}{2^{\nu+2}} \sum_{m=1}^{M} \sum_{n=1}^{N} W_L^{(m)} W_J^{(n)} (\gamma = 1, \beta = \nu - 1) f(\xi_{i,n}, \xi_{i\mp 1,m}). \qquad \text{(D-32)}$$

- $(1 - \xi_i)^{\nu-1}$: For the basis functions used in the boundary triangles of type T_2 and the surface divergences of the basis functions $\bar{f}_{2,2}$ and $\bar{f}_{3,1}$ the integral takes the form

$$I_2 = \int_0^1 \int_0^{1-\xi_{i\mp 1}} (1 - \xi_i)^{\nu-1} f(\xi_i, \xi_{i\mp 1}) d\xi_i d\xi_{i+1}. \qquad \text{(D-33)}$$

Comparing (D-33) and (D-30),

$$I_2 = \frac{1}{2^{\nu+2}} \sum_{m=1}^{M} \sum_{n=1}^{N} W_L^{(m)} W_J^{(n)} (\gamma = \nu, \beta = 0) f(\xi_{i,n}, \xi_{i\mp 1,m}). \qquad \text{(D-34)}$$

- $(1 - \xi_i)^{\nu-2}$: This term arises in integrating the divergences of the basis functions $\bar{f}_{2,1}$, $\bar{f}_{3,2}$, $\bar{f}_{4,1}$ and $\bar{f}_{4,2}$. The surface integral can be expressed as

$$I_3 = \int_0^1 \int_0^{1-\xi_{i\mp 1}} (1 - \xi_i)^{\nu-2} f(\xi_{i,n}, \xi_{i\mp 1,m}) d\xi_i d\xi_{i+1}. \qquad \text{(D-35)}$$

Comparing (D-33) and (D-30),

$$I_3 = \frac{1}{2^{\nu+1}} \sum_{m=1}^{M} \sum_{n=1}^{N} W_L^{(m)} W_J^{(n)} (\gamma = \nu - 1, \beta = 0) f(\xi_{i,n}, \xi_{i\mp 1,m}). \qquad \text{(D-36)}$$

It should be noted that in (D-32)-(D-36) the singularity is placed along ξ_i. Thus, ξ_i and $\xi_{\mp 1}$ should replace u and v respectively in (D-30). The function $f(\xi_{i,n}, \xi_{i\mp 1,m})$ represents an arbitrary function for each expression. The parameters to be used in (D-30) for the three types of basis functions are listed in Table D-2.

Table D-2: Numerical integration parameters for the singular basis functions.

	γ	β
$\xi_i^{\nu-1}$	1	$\nu - 1$
$(1 - \xi_i)^{\nu-1}$	ν	0
$(1 - \xi_i)^{\nu-2}$	$\nu - 1$	0

D.4 Evaluation of the Self Term

When the source and observation triangles coincide, the integrands in (D-7) and (D-8) become singular. In general, when $\bar{r}$ and $\bar{r}'$ are very close to each other, R vanishes and the Green's function is singular. This occurs in evaluating the self term Z_{mm}. The potential integral in (D-25) can be expressed in the form

$$\bar{I}(\bar{r}) = \int_{T'} \bar{f}(\bar{r}') \frac{e^{jk|\bar{r}-\bar{r}'|}}{|\bar{r}-\bar{r}'|} dS \qquad (D-37)$$

where T' is the triangular patch over which the integration is being performed and $\bar{f}(\bar{r}')$ denotes the basis function associated with a given edge of the triangular patch. When the observation point $\bar{r}$ and the source point $\bar{r}'$ are in the same triangular patch, the integrand becomes singular. This singularity due to Green's function must be extracted. To accomplish this, the integral (D-37) is expressed as $\bar{I}(\bar{r}) = \bar{I}_n(\bar{r}) + \bar{I}_a(\bar{r})$, where

$$\bar{I}_n(\bar{r}) = \int_{T'} \frac{\bar{f}(\bar{r}')e^{jk|\bar{r}-\bar{r}'|} - \bar{f}_T(\bar{r}')}{|\bar{r}-\bar{r}'|} dS, \qquad (D-38)$$

$$\bar{I}_a(\bar{r}) = \int_{T'} \frac{\bar{f}_T(\bar{r}')}{|\bar{r}-\bar{r}'|} dS. \qquad (D-39)$$

The function $\bar{f}_T$ is the Taylor series expansion of $\bar{f}$ around the observation point $\bar{r}_o$. In the areal coordinates, $\bar{I}_n$ can be expressed as

$$\bar{I}_n(\bar{r}(\xi_i,\xi_{i+1})) = 2S \int_0^1 \int_0^{1-\xi_{i+1}} \frac{f(\xi_i',\xi_{i+1}')e^{jk|\bar{r}(\xi_i,\xi_{i+1})-\bar{r}'(\xi_i',\xi_{i+1}')|} - \bar{f}_T(\xi_i',\xi_{i+1}')}{|\bar{r}(\xi_i,\xi_{i+1})-\bar{r}(\xi_i',\xi_{i+1}')|} d\xi_i d\xi_{i+1}$$

$$(D-40)$$

where S denotes the are of the triangular patch. The resulting integrand is well-behaved for all types of basis functions and the integral can be calculated numerically by employing a Gaussian quadrature rule. It should be noted that, for the singular basis functions, the integrand in (D-40) can easily be written in one of the three forms described in Section D.3. Using (D-24), $\bar{I}_n$ is given by

$$\bar{I}_n(\bar{r}(\xi_i,\xi_{i+1})) = 2S \sum_{m=1}^{M} W_m \frac{f(\xi_i^{(m)},\xi_{i+1}^{(m)})e^{jk|\bar{r}(\xi_i,\xi_{i+1})-\bar{r}'(\xi_i^{(m)},\xi_{i+1}^{(m)})|} - \bar{f}_T(\xi_i^{(m)},\xi_{i+1}^{(m)})}{|\bar{r}(\xi_i,\xi_{i+1})-\bar{r}'(\xi_i^{(m)},\xi_{i+1}^{(m)})|} d\xi_i d\xi_{i+1}$$

$$(D-41)$$

where W_m denotes the weight at the mth integration node $(\xi_i^{(m)}, \xi_{i+1}^{(m)})$. Taylor series expansion of $\bar{f}(\xi_i, \xi_{i+1})$ around the observation point $\bar{r}_o(\xi_i^o, \xi_{i+1}^o)$ is given by

$$\bar{f}_T(\xi_i, \xi_{i+1}) = \bar{f}(\xi_i^o, \xi_{i+1}^o) + \bar{D}_i(\xi_i - \xi_i^o) + \bar{D}_{i+1}(\xi_{i+1} - \xi_{i+1}^o) + \bar{D}_{i-1}(\xi_{i-1} - \xi_{i-1}^o) \quad \text{(D-42)}$$

where

$$\bar{D}_i = \frac{\partial f(\xi_i, \xi_{i+1})}{\partial \xi_i}\Big|_{(\xi_i^o, \xi_{i+1}^o)} \quad \text{(D-43)}$$

$$\bar{D}_{i+1} = \frac{\partial f(\xi_i, \xi_{i+1})}{\partial \xi_{i+1}}\Big|_{(\xi_i^o, \xi_{i+1}^o)} \quad \text{(D-44)}$$

$$\bar{D}_{i-1} = \frac{\partial f(\xi_i, \xi_{i+1})}{\partial \xi_{i-1}}\Big|_{(\xi_i^o, \xi_{i+1}^o)}. \quad \text{(D-45)}$$

Substituting (D-43)-(D-45) in (D-39), and transforming the resulting integral into areal coordinates, $\bar{I}_a(\bar{r})$ can be expressed as

$$\bar{I}_a = 2S\left[f(\xi_i^o, \xi_{i+1}^o) - \bar{D}_i\xi_i^o - \bar{D}_{i+1}\xi_{i+1}^o - \bar{D}_{i-1}\xi_{i-1}^o\right]\int_{T'}\frac{1}{R}dS'$$
$$+ 2S\left\{\bar{D}_i\int_{T'}\frac{\xi_i}{R}dS' + \bar{D}_{i+1}\int_{T'}\frac{\xi_{i+1}}{R}dS' + \bar{D}_{i-1}\int_{T'}\frac{\xi_{i-1}}{R}dS'\right\} \quad \text{(D-46)}$$

where $R = |\bar{r}(\xi_i, \xi_{i+1}) - \bar{r}'(\xi_i', \xi_{i+1}')|$. Consider the triangle T' depicted in Fig. D-3. The integrals in (D-46) can be calculated using the integrals

$$g_s = \int_T \frac{1}{R}dS \quad \text{(D-47)}$$

$$\bar{g}_k = \int_T \frac{\bar{\rho}_k}{R}dS \quad \text{(D-48)}$$

which can be evaluated analytically [54]. The subscript k denotes the vertex index (i, i+1 or i-1) and $\bar{\rho}_k$ is the position vector with respect to the kth vertex as shown in Fig. D-3. The position vectors with respect to vertex i-1 can be expressed in terms of the edge vectors as

$$\bar{\rho}_{i-1} = \xi_i\bar{\ell}_{i+1} - \xi_{i+1}\bar{\ell}_i. \quad \text{(D-49)}$$
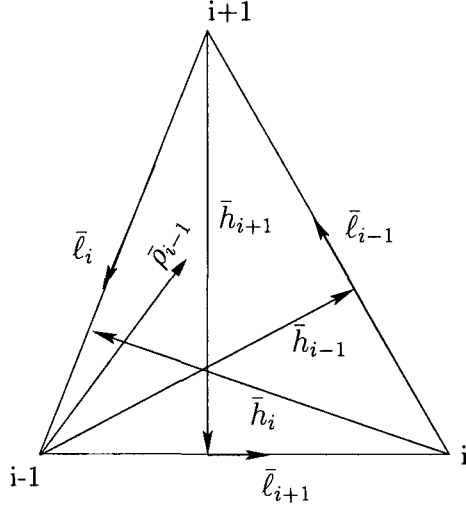
123

Figure D-3: Local vectors defined over a patch.

Noting that $\bar{\ell}_i \cdot \hat{h}_i = \bar{\ell}_{i+1} \cdot \hat{h}_{i+1} = 0$, the integrals defined as

$$I_a^{(i)} = -\bar{g}_{i-1} \cdot \frac{\hat{h}_i}{h_i} = -2S \int_T \frac{\xi_i}{R} dS \bar{\ell}_{i+1} \cdot \frac{\hat{h}_i}{h_i} = 2S \int_T \frac{\xi_i}{R} dS$$

$$I_a^{(i+1)} = -\bar{g}_{i-1} \cdot \frac{\hat{h}_{i+1}}{h_{i+1}} = -2S \int_T \frac{\xi_{i+1}}{R} dS \bar{\ell}_i \cdot \frac{\hat{h}_{i+1}}{h_{i+1}} = 2S \int_T \frac{\xi_{i+1}}{R} dS$$

(D-50)

are used in (D-46) resulting in

$$\bar{I}_a = [f(\xi_i^o, \xi_{i+1}^o) - \bar{D}_i \xi_i^o - \bar{D}_{i+1} \xi_{i+1}^o - \bar{D}_{i-1} \xi_{i-1}^o] g_s$$

$$+ \bar{D}_i I_a^{(i)} + \bar{D}_{i+1} I_a^{(i+1)} + \bar{D}_{i-1} I_a^{(i-1)}$$

(D-51)

where $I_a^{(i-1)}$ is given by

$$I_a^{(i-1)} = g_s - I_a^{(i+1)} - I_a^{(i)}.$$

(D-52)

Eq. (D-52) follows from (D-47) and the fact that $\xi_i + \xi_{i+1} + \xi_{i-1} = 1$.